UNIVERSITY OF SOUTHAMPTON

ABSTRACT

FACULTY OF ENGINEERING AND THE ENVIRONMENT
SCHOOL OF ENGINEERING SCIENCES

Doctor of Philosophy

A NANOSTRUCTURED COMPOSITE MATERIAL FOR HYDROGEN STORAGE: DESIGN & ANALYSIS

by Abdulwahid A. Al-Hajjaj

Hydrogen has long been considered an ideal energy carrier for a sustainable energy economy, for both direct combustion and as a fuel for polymer-electrolyte fuel cells. One of the main challenges associated with the use of hydrogen is to find efficient methods of storage. Any method must be safe, reversible, cost-effective and practical. In this thesis, a general introduction to hydrogen energy and the hydrogen economy is provided, together with descriptions of incumbent and emerging storage methods. A mathematical framework for simulating sorption isotherms in microporous materials is developed. This framework provides explicit expressions for the excess, condensed, compressed and absolute hydrogen masses. Furthermore, key parameters such as the surface area and adsorption volume can be estimated (for the first time) using a single-step nonlinear regression analysis, with the use of any isotherm model. Values are derived for three classes of porous materials, showing consistency with experimental data. A novel composite consisting of titanate nanotubes decorated with nanostructured metal cyanide frameworks, e.g., cadmium ferricyanide ($Cd_3[Fe(CN)_6]_2$), are synthesised. The equilibrium and kinetic hydrogen sorption properties of the titanate-nanotube/$Cd_3[Fe(CN)_6]_2$ composite are studied at low, intermediate and high pressure (up to 150 bar), revealing uptake values of ca. 14 weight %, which compare favourably with known materials for hydrogen storage. The role of mass transport in the sorption process is investigated, including the effects of boundary-layer diffusion and intraparticle diffusion. The results suggest that the composite possesses good hydrogen mass transfer characteristics. The effects of the reaction environment during synthesis are explored and the samples are thoroughly characterised. Significant differences in the loading of $Cd_3[Fe(CN)_6]_2$ on the titanate nanotubes are seen. Hydrogen and nitrogen sorption analyses reveal the role of the pore size distribution on the effective surface area for adsorption and, therefore, the hydrogen uptake.

Table of Contents

List of Figures

List of Tables

DECLARATION OF AUTHORSHIP

I, **Abdulwahid A. Al-Hajjaj** declare that the thesis entitled **A NANOSTRUCTURED COMPOSITE MATERIAL FOR HYDROGEN STORAGE: DESIGN & ANALYSIS** and the work presented in the thesis are both my own, and have been generated by me as the result of my own original research. I confirm that:

- this work was done wholly or mainly while in candidature for a research degree at this University;
- where any part of this thesis has previously been submitted for a degree of any other qualification at this University or any other institution, this has been clearly stated;
- where I have consulted the published work of others, this is always clearly attributed;
- where I have quoted from the work of others, the source is always given. With the exception of such quotations, this thesis is entirely my own work;
- I have acknowledged all main sources of help;
- where the thesis is based on work done by myself jointly with others, I have made clear exactly what was done by others and what I have contributed myself;
- parts of this work have been published as (my contribution is described in detail):

(1) **Al-Hajjaj A.A.**, Zamora B., Bavykin D.V., Shah A.A., Walsh F.C., Reguera E., On the application of standard isotherms to hydrogen adsorption in microporous materials, *International Journal of Hydrogen Energy* 37, 2012: 318-326.

Role: Developed most of the mathematical framework; performed the regression analysis; performed most of the analysis of the results; wrote first draft.

(2) **Al-Hajjaj A.A.**, Zamora B., Shah A.A., Reguera E., Bavykin D.V., Walsh F.C., Sorption of hydrogen onto titanate nanotubes decorated with a nanostructured $Cd_3[Fe(CN)_6]_2$ Prussian Blue analogue, *International Journal of Hydrogen Energy* 36, 2011: 14464-14476.

Role: Synthesised the composite (including the original idea); designed the research programme; performed FTIR, and all H_2 adsorption experiments; analysed results; wrote first draft

(3) **Al-Hajjaj A.A.**, Zamora B., Shah A.A., Bavykin D.V., Reguera E., Kinetic and thermodynamic studies of hydrogen adsorption on titanate nanotubes decorated with a Prussian blue analogue, under review for publication in *International Journal of Hydrogen Energy*.

Role: Designed the research programme; synthesised the composites; performed all kinetic H_2 adsorption experiments; performed the mathematical analysis; analysed results; wrote first draft.

(4) **Al-Hajjaj A.A.**, Zamora B., Reguera E., Bavykin D.V., Shah A.A., Hydrogen adsorption on titanate nanotubes decorated with a Prussian blue analogue: The role of pH during synthesis on H_2 adsorption, in preparation.

Role: Designed the research programme; participated in TEM, high resolution TEM, AFM, EDX, XPS; performed FTIR, XRD and TGA; performed H_2 and N_2 adsorption experiments; analysed results; writing first draft.

(5) **Al-Hajjaj A.A.**, Shah A.A., Bavykin D.V., "Modelling and comparison of isothermal discharge in hydrogen storage systems", in *The XIX International Materials research Congress*, Cancun, Mexico, Aug 2010 (oral presentation).

(6) **Al-Hajjaj A.A.**, Shah A.A., Bavykin D.V., "Mathematical modelling of isothermal discharge in hydrogen storage systems", in *The 16th Postgraduate Conference*, Southampton University, UK, Oct 1st 2010 (poster).

(7) **Al-Hajjaj A.A.**, Zamora B., Bavykin D.V., Shah A.A., Walsh F.C., Reguera E., "Synthesis and characterization of a PBA/TiNT composite for hydrogen storage", Presented in *Symposium of Summer School Calorimetry,* Lyon, France, June 19–25, 2011 (poster).

(8) **Al-Hajjaj A.A.**, Zamora B., Shah A.A., Bavykin D.V., Reguera E., "Synthesis, characterisation and application of novel titanate

nanotube/Prussian blue composites", in *Conference of Engineering Sciences, Iraqi Cultural Attaché,* University College London, UK, November 2nd , 2011 (oral).

Signature: .....

Date: .....

Acknowledgments

First and foremost, I am extremely grateful to my supervisors Dr Dmitry Bavykin and Dr Akeel Shah whose doors were always open. I am grateful to Dr Bavykin for giving me the opportunity to work in the area of hydrogen storage and for his continual guidance. You replied to all my enquiries with great haste. I am grateful to Dr Shah for his open-minded approach to problems, and for his willingness to take time to direct and guide my research. I will always remember your efforts with great fondness. I would also like express my gratitude to Professor Frank Walsh for many useful observations and suggestions.

My sincere appreciation and gratitude are expressed to Professor Edilso Reguera Ruiz of Centro de Investigacion en Ciencia Aplicada y Tecnologia Avanzada del IPN (CICATA), Mexico for his continual advice, suggestions and assistance.

I gratefully acknowledge the financial support from the Ministry of Higher Education and Scientific Research, Iraq and the cultural attaché staff in London for their continuous support.

During my research visit to CICATA, I was supported by many people. I am happy that I have the opportunity to express my gratitude to the following persons and institutions in México: Abel Tinoco Davila, Monica Maria Centeno Alvarez, Dr. Eduardo Perez Cappe, Omar Reyes Martinez, Juan Antonio Jimenez Gallegos, Alfonso Martinez Perez, Jose Refugio Lopez Serrato (Cuco), Alicia Lopez Torres, Nelida Lopez, Claudia Guadalupe Leon Lara, Cindy Arianna Samano Alonso, Alma Lilia Garcia, Naudimar Chavez Hernandez and Osiry Hernandez Silva from CICATA, IPN; Dr Juan Vicente Méndez Méndez, Dr Luis Lartundo Rojas from Centro de Nanociencias y Micro y Nanotecnología, IPN; Dr Patricia Santiago from Instituto Mexicano del Petroleo; and Dr. Jorge Balmaseda and Prof. David Diaz from UNAM University.

I would also to express my sincere thanks to Ms Rachel White for preparing some TEM images at University of Southampton**.** I am extremely thankful to my friend Maytham Al-Abbas and his family for their continuous help. I am grateful for the support provided to me and my family during the last three years.

I would like to express my deepest gratitude and a special word of thanks to my family in Iraq for their patience, love and support in the past three years. You were my main source of encouragement and inspiration and will always occupy a special place in my heart and in my mind.

Last, but definitely not least, I would like to express my special thanks to my partner Blanca Estela Zamora Reynoso for the unlimited support, for her company during the long working days and nights in Southampton and in CICATA, and for her full understanding during the hard times. Without you I could not have reached this far Thank you for anything and everything.

Nomenclature

Roman

Symbol	Definition	Unit
A	Aare	m^2
b	Toth adjustable parameter	Pa
c	UNILAN adjustable parameter	Pa
D	Diffusion coefficient	$m^2\ s^{-1}$
E	Energy	kJ mol^{-1}
K	Affinity constant	Pa^{-1}
k	Equilibrium rate constant	s^{-1} or kg $kg^{-1}\ s^{-1}$
l	Height	m
$\dot{m}$	Mass Flow rate	kg s^{-1}
m_e	Excess gravimetric capacity	kg kg^{-1}
$\tilde{m}_e$	Excess volumetric capacity	m^3 kg^{-1}
m_{H_2}	Molecular mass of hydrogen	kg mol^{-1}
m_t	Absolute capacity	kg
M	Mass	kg
M_e	Excess mass	kg
n	Heterogeneity parameter	Dimensionless
N_A	Avogadro's number	mol^{-1}
P	Pressure	bar
P_s	Pseudo saturation vapour pressure	bar
q_m	Maximum adsorbed capacity	kg kg^{-1}
q_{H_2}	Mass of hydrogen adsorbed	kg kg^{-1}
r	radius	m
R	gas constant	J mol^{-1} K^{-1}
R^2	Coefficients of determination	Dimensionless
S	Surface area	m^2 kg^{-1}
s	UNILAN adjustable parameter	Dimensionless
t	Time	s
T	Temperature	K

ν	IR vibration	Dimensionless
V_a	Interfacial layer volume	$m^3\ kg^{-1}$
V_b	Total volume of the sample	$m^3\ kg^{-1}$
V_g	Total gas volume	$m^3\ kg^{-1}$
V_m	Volume occupied by a monolayer	$m^3\ kg^{-1}$
V_{pore}	Specific pore specific volume	$m^3\ kg^{-1}$
V_s	Solid skeleton specific volume	$m^3\ kg^{-1}$

Greek

Symbol	**Definition**	**unit**
ΔH	Isosteric enthalpy	$kJ\ mol^{-1}$
ρ	density	$kg\ m^{-3}$
λ	Number of adsorbate layers	Dimensionless
ε	Porosity	Dimensionless
θ	Coverage ratio	$(kg\ H_2)\ (kg^{-1}$ solid)
σ	Average reach of an adsorbate molecule	m
ψ	Adsorption potential	$kJ\ mol^{-1}$
τ	Time constant	s

Subscripts	**Meaning**
a	Activation
ads	Adsorbed
b	Bed
c	Critical or condensed condition
DA	Dubinin-Astakhov
e	Excess
g	Gas
k	Knudsen
L	Langmuir
LF	Langmuir-Freundlich
m	molecular
max	Maximum

min	Minimum
p	Particle
r	Radial
s	Solid or saturation
T	Toth
U	UNILAN
z	Longitudinal
0	Initial values

Abbreviations

AAS	Atomic Absorption Spectrophotometer
APD	average pore diameter
AFM	Atomic Force Microscopy
a.u.	Arbitrary units
BDDT	Brunauer-Deming- Deming- Teller
BET	Brunauer-Emmett-Teller
BJH	Barrett-Joyner-Halenda
Cd_3Fe^{III}	Cadmium prussian blue analogue
CoIIICu	Copper hexacyanocobaltate (III)
COF	Covalent Organic Framework
CPV	Cumulative Pore Volume
$Cu_3(BTC)_2$	Copper 1,3,5-benzene tricarboxylate
D-A	Dubinin-Astakhov
DOE	US Department of Energy
3D	Three dimensional
EA	Elemental analysis
EDX	Energy-dispersed X-ray
FTIR	Fourier Transform Infrared spectroscopy
HR	High Resolution
IUPAC	International Union of Pure and Applied Chemistry
L-F	Langmuir-Freundlich
MCF	Metal Cyanide-Framework
MH_x	Metal Hydride

MOF	Metal Organic Framework
MWNT	Multi-Walled Nanotube
NP	Nitroprusside
OEA	Organic Elemental Analysis
PB	Prussian Blue
PCT	Pressure Composition Temperature
SEM	Scanning Electron Microscopy
SSA	Specific Surface Area
SWNT	Single-Walled Carbon Nanotube
TEM	Transmission Electron Microscopy
TGA	Thermo Gravimetric Analysis
TiNT	Titanate Nanotube
wt.	Weight
XRD	X Ray Diffraction
XPS	X-Ray Photoelectron Spectroscopy
Z	Compressibility factor
ZIF	Zeolitic Imidazolate Framework

Chapter 1: Introduction

1.1 Hydrogen: the future of energy?

The demand for energy has increased rapidly with the growth in the world population and with improvements in living standards. Indeed, the world population has increased by a factor of 6 in the last century, while the energy consumption has risen by a factor of 80 [1]. Recently, the worldwide average continuous power consumption is 2kW per person; in the USA the power consumption is on average 10kW per person and in Europe about 5 kW per person, [2]. The transportation sector is the largest consumer of petroleum products [3]. With a continually growing global population, the number of vehicles and the energy demand for residential and commercial, transportation, industrial requirements, are further projected to grow [4,5].

Despite the variety of energy resources, the demand for power is still largely met by fossil hydrocarbons, i.e., coal, oil and natural gas. Recent studies have confirmed the domination of these resources, estimated to be up to 85% of the world's energy needs [6]. The projected shortage for fossil fuels, along with the detrimental impact that heavy use of these fuels is believed to have on the environment, has motivated the development of a host of sustainable, clean energy technologies.

Renewable and sustainable sources of power such as solar, wind and hydrogen are still very much under development. Hydrogen has long been considered a future energy carrier, particularly for sustainable and clean power. The combustion of hydrogen with air does not give rise to harmful (either toxic or greenhouse) emissions. It is also the preferred fuel for polymer electrolyte fuel cells, for which the final product of electrochemical reaction is simply water. Hydrogen is particularly attractive since it has a high energy density per unit weight compared to any other known fuel, excluding nuclear fuels. It has a gravimetric calorific value of around 120 kJ kg^{-1} (see Table 1.1), which is equivalent to 33.3 kWh kg^{-1} [7]. The energy content of one kg of hydrogen is

equivalent to approximately one gallon (i.e. about 2.7 kg) of gasoline, potentially making it a more portable energy carrier. The biggest constraint, however, is the volume requirement; one gram of hydrogen gas occupies around 11 litres of volume at atmospheric pressure.

Table 1.1: Properties of hydrogen compared with some common fuels [8].

Property	Hydrogen	Petroleum (gasoline)	Methane	Methanol
Boiling point (K)	20.3	350-400	111.7	337
Liquid density @bp (kg m^{-3})	70.8	700	425	423
Gas density @STP (kg m^{-3})	0.08	4.7	0.66	–
Vaporization heat (kJ kg^{-1})	444	300	577	1168
Combustion heat (MJ kg^{-1})	120	44.5	50.0	20.1
Combustion heat (MJ m^{-3})	8960	31170	21250	16020
Ignition temperature (K)	858	495	807	658

Although hydrogen energy systems are not new, the rising demand for energy and the introduction of targets for CO_2 reduction (at global and national levels) have generated a strong impetus behind a hydrogen-based energy economy, not least for automotive propulsion [9-12]. Recent studies have identified a number of key technical challenges to be overcome before a hydrogen-based energy economy can become a reality [13,14]. Notable amongst these challenges are the development of efficient methods for the production, storage, transportation and safe handling of the fuel. Due to its explosiveness (the explosion limit of 18.3–59%) [15], safety is an overriding concern, particularly if the hydrogen is to be carried on board a vehicle [16,17].

A hydrogen fuel cell car needs to store at least 4 kg hydrogen in order to have the same range as a gasoline-powered car. In order to store this quantity of hydrogen in a gaseous state at room temperature and atmospheric pressure, an extremely large volume container would be required (44 m^3). Such a large volume would clearly not be practical for automobile applications. The gas can be compressed but the accompanying high pressure (up to 450 bar) poses risks [18]; the required pressure would be much higher

than that of a typical gasoline-powered vehicle. Thus, storage as a gas is not practical for automobile applications [19].

The U.S. Department of Energy (DOE) targets for hydrogen powered vehicles include a driving range of more than 300 miles, together with strict volume and cost constraints. The DOE has also established targets of 6 wt. % by 2010 and 9 wt. % by 2015 of H_2 for automobiles applications, for any storage system [20-22]. The various targets set by the DOE are shown in Table 1.2.

Table 1.2: The DOE set of some technical requirements for hydrogen storage systems used in transportation applications [20-22].

Storage parameter	2010	2015
Gravimetric capacity (wt. % H_2)	6%	9%
Volumetric capacity (kg H_2 m^{-3})	45	81
Storage system cost ($/kg H_2)	133	67
Operating ambient temperature (K)	243-323	233-333
Minimum and maximum delivery temperature of H_2 from tank (K)	243-358	233-358
Maximum delivery pressure of H_2 from tank (atm)	100	100
Maximum delivery pressure of H_2 from tank to fuel cell (atm)	4	3
Maximum delivery pressure of H from tank to internal combustion engine (atm)	35	35
Minimum full-flow rate (g s^{-1} kW^{-1})	0.02	0.02
Start time to full flow at 298 K (s)	4	0.05
Start time to full flow at minimum ambient temperature (s)	8	2

1.2 Scope of the thesis

A brief introduction to hydrogen energy was provided above. A review of the fundamentals of conventional hydrogen storage methods and materials will be provided

in Chapter 2. Chapter 3 describes the materials, experimental methods and characterization techniques used throughout this thesis.

A mathematical framework for simulating hydrogen adsorption isotherms in porous materials and estimating key parameters associated with the adsorption process is developed and discussed in detail in Chapter 4. Explicit expressions for the surface excess, adsorbed/condensed, compressed and absolute masses, for any model isotherm relation, are derived. Equilibrium isotherms for three classes of microporous materials (Prussian blue analogues, nitropussides and metal-organic frameworks) are determined experimentally. The model is used in combination with five standard isotherm models to simulate the experimental data *via* nonlinear regression and to estimate the surface areas, the affinity and heterogeneity factors, and the pressure-dependent adsorption volumes. The results (including simulated adsorbed and absolute masses) are discussed and the estimated parameter values are compared to those available in the literature, demonstrating consistency.

In Chapter 5 a study of hydrogen sorption in titanate nanotubes decorated with nanostructured cadmium ferrocyanide ($Cd_3[Fe(CN)_6]_2$) is presented. The nanostructured composite is synthesized by the deposition of cadmium ferricyanide, $Cd_3[Fe(CN)_6]_2$, on the surfaces of titanate nanotubes (TiNTs) by ion exchange with $CdSO_4$ followed by reaction with $K_3[Fe(CN)_6]$ in an aqueous suspension. Cadmium ions migrate to the nanotube surfaces to form –Fe-CN-Cd- chains and K^+ ions are incorporated on the TiNT surfaces to maintain charge balance. Information on the nature of the formed surface complex was obtained from IR spectra and XRD data. Electron microscopy studies show that $Cd_3[Fe(CN)_6]_2$ is distributed on the surfaces of the TiNTs in the form of a precipitate. The composite exhibits a significantly higher level of hydrogen uptake than both the base $Cd_3[Fe(CN)_6]_2$ and TiNTs. at a temperature of 77 K and a pressure of 100 bar, the hydrogen uptake for the composite is approximately 12.5 wt. %, whereas only 4.5 wt. % and 4 wt. % are achieved for the TiNTs and $Cd_3[Fe(CN)_6]_2$, respectively.

In Chapter 6, the kinetic and thermodynamic hydrogen adsorption characteristics of the $Cd_3[Fe(CN)_6]_2$/TiNT composite are investigated at high pressures and different temperatures. The contributions of the various mechanisms of mass transport are compared. It is shown that boundary-layer diffusion (as defined in Chapter 6) does not play a limiting role in the mass transport of hydrogen inside the composite material. The

diffusion coefficient and time constant at different temperatures and pressures are calculated using an intra-particle diffusion model. The results suggest that molecular diffusion is dominant in the overall mass transport. The Gibb's free energy is estimated by fitting isotherm equilibrium data to the Dubinin–Astakhov model and is used to calculate the enthalpy and the entropy of adsorption. The calculated value of enthalpy is characteristic of a physisorption process and is considerably higher than the activation energy for intraparticle diffusion, suggesting that the rate-limiting step of the overall process of hydrogen adsorption onto the composite material is surface adsorption.

In Chapter 7, the effects of variations in the pH during synthesis of the $Cd_3[Fe(CN)_6]_2$/TiNT composite are investigated. Samples of the composite are thoroughly characterised to reveal their surface characteristics and gas adsorption properties. Significant variations in the H_2 uptake are seen, and the reasons for the differences are explained using the results from high resolution transmission electron microscopy, atomic force microscopy, energy-dispersive X-ray spectroscopy, elemental analysis, Fourier-transform infrared spectroscopy, X-ray diffraction analysis and X-ray photospectroscopy and thermogravimetric analysis. The effect of the pH on the loading of $Cd_3[Fe(CN)_6]_2$ on the TiNTs and on the morphology of the composite are discussed, particularly in relation to the active surface area for adsorption.

In Chapter 8, a summary and conclusions are provided, together with an outline of future work.

References

[1] Jochem E., Energy Environ. 2 (1991) 31–44.

[2] Zuttel A., Naturwissenschften 91 (2004) 157–172.

[3] Gross K., The reversible hydride solution for hydrogen storage, G-CEP Hydrogen workshop, April 14-15, 2003 California. USA.

[4] Ogden J.M. (2001) The Int. Energy Agency, Golden, IEA/H2/TR02/002.

[5] Dunn S., *Worldwatch Paper* 157 (2001), Worldwatch Institute, Washington, DC.

[6] Zuttel A., Borgschult A., and Schlapbach L., Hydrogen as future energy carrier, Wiley-VCH, Germany (2008).

[7] Klell M., Kindermann H., Jogl C., *Proceedings Int. Hydrogen Congress and Exhibition IHEC* (2007), Istanbul, Turkey, 13–15 July 2007.

[8] van den Berg A.W.C., Arean C.O., Chem. Commun. 6 (2008) 668–681.

[9] Scheuerer K., *World Nuclear Association Annual Symposium* (2004) 8–10 September – London.

[10] Evenson W.E., *R&D of Energy Technologies Report* (2005), Annex IV-Section 1, 209–215.

[11] Aceves S.M., Berry G.D., Ramach G.D., Int. J. Hydrogen Energy 23 (1998) 583–591.

[12] Guo Z.X., Shang C., Aguey-Zinsou K.F., J. European Ceramic Society 28 (2008) 1467–1473.

[13] Schlapbach L., Zuttel A., Nature 414 (2001) 353.

[14] Edwards P.P., Kuznetsov V.L., David W.I.F., Brandon N.P., Energy Policy 36 (2008) 4356–4362.

[15] Bartram R. J., Froehlich P., LCGC NORTH AMERICA 28 (2010) 1–8

[16] Crabtree G.W., Dresselhaus M.S., Buchanan M.V., Physics Today 57 (2004) 39–44.

[17] Harris R., Book D., Anderson P.A., Edwards P.P., The Fuel Cell Review, June/July, (2004) 17–23.

[18] Kang J.K., Lee J.Y., Muller R.P., Goddard W.A., J. Chem. Phys. 121 (2004) 0623–10633.

[19] Das L.M., Int. J. Hydrogen Energy 21 (1996) 789–800.

[20] Iniguez J., Yildirim T., Appl. Phys. Lett. 86 (2005) 103109, 1–4.

[21] Sun Q., Wang Q., Jena P., Reddy V., Marquez M., Chem. Mater. 19 (2007) 3074–3078.

[22] Wu X., Gao Y., Zeng X.C., J. Phys. Chem C 112 (2008) 8458–8463.

Chapter 2: Literature review

2.1 Introduction

The limited availability of fossil fuels, together with concerns over their impact on the environment, has motivated the search for alternative fuels, as well as the development of a host of sustainable, clean energy technologies. Due to its high-energy density, abundance and environmentally-friendly by-products of combustion, hydrogen has long been considered as one of the most promising alternatives [1]. The hydrogen energy economy is generally based on production, distribution and delivery through the storage means, which make the utilization of hydrogen possible.

The diversity of production methods is one of the main attractions of hydrogen as an energy source. Hydrogen can be produced from [2,3]:

1) reforming of natural gas; gasification of coal;
2) the splitting of water by water-electrolysis, photo-electrolysis, photo-biological production and high temperature thermo-chemical cycles;
3) biomass and even municipal waste.

Each of these routes is currently at a different stage of development, and each offers unique benefits and challenges. Selection of the method is influenced by policy issues, the local availability of feedstock, the maturity of the technology, the market applications, demand, and costs [4]. Hydrogen is industrially produced through several technology options that are readily available in the market. Pure hydrogen was first produced commercially using the process of electrolysis of water in the late 1920s. A fossil-based feedstock then gradually replaced this process in the 1960s [4]. The central role of hydrogen as an energy carrier associated with the multiple hydrogen production methods and various end-user applications are demonstrated, based on the chart published by Edward *et al.* [3], in Figure 2.1.

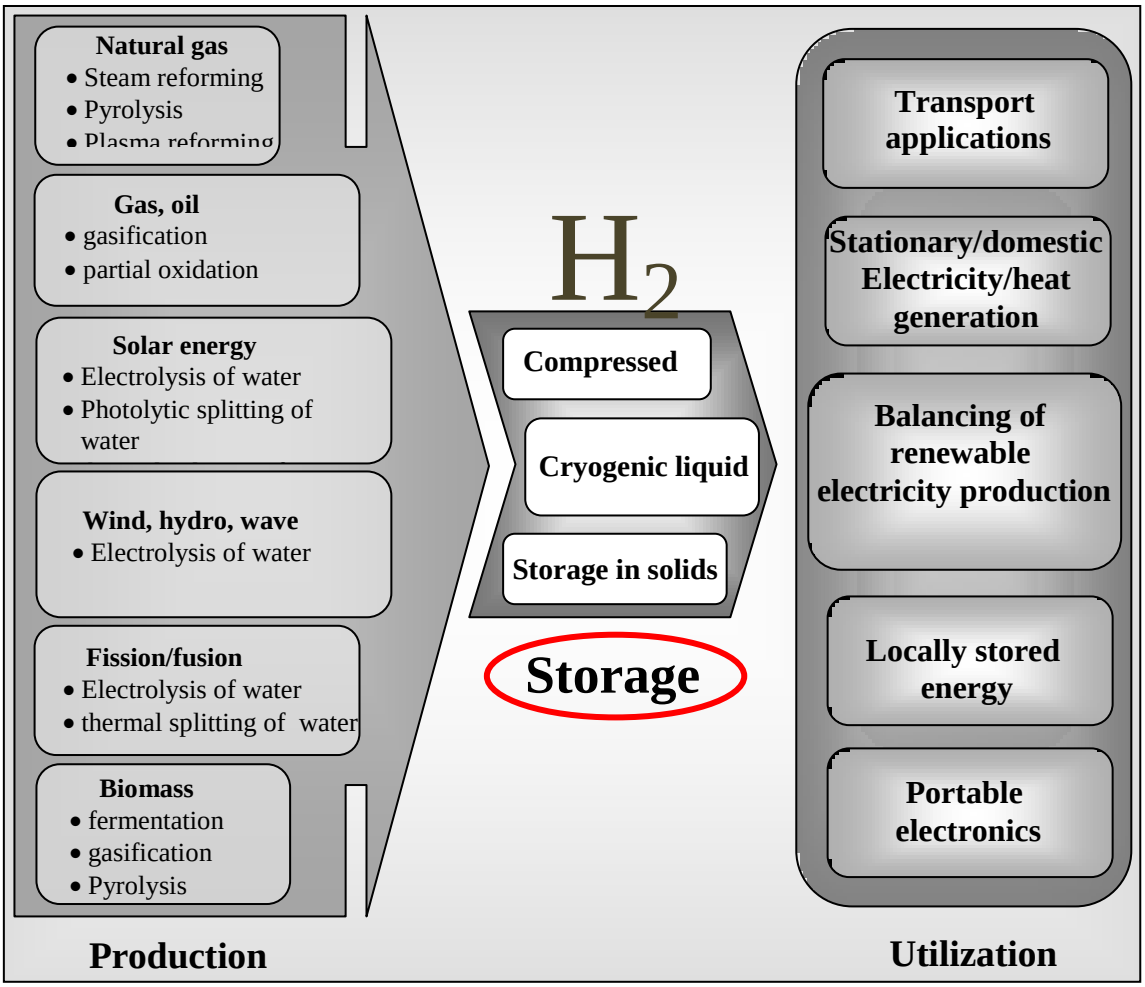

Figure 2.1: Hydrogen economy cycle.

Currently, the most practical hydrogen production method is based on the process of steam reforming of natural gas and partial oxidation of coal or heavy hydrocarbons [3]. Since it can be applied on a large scale and is cost effective, this process has distinct advantages. The associated production of carbon dioxide, however, is a major drawback in the production of hydrogen during the reforming process and poses a major challenge for the environmentally benign utilization of hydrogen [5]. In order to increase the reliability and flexibility of hydrogen production technologies, significant improvements in the plant efficiencies and capital cost reductions are required. Extensive investigations have been carried out on hydrogen production techniques [6,7]. Such methods are beyond the scope of this thesis and will not, therefore, be addressed in detail.

Apart from the method of hydrogen production, the development of practical and safe methods of **hydrogen storage** is vital to the advancement of hydrogen-based energy technologies, particularly the proton exchange membrane fuel cell. Hydrogen storage is anticipated to be a major concern in relation to meeting the DOE targets in terms of both volumetric and gravimetric energy/power densities for vehicular applications (the main application area for hydrogen fuel cells) [8]. The aim of this chapter is to present an overview of the technical challenges involved in storing hydrogen.

2.2 Hydrogen storage methods

Hydrogen can be stored in various ways depending on the application, which can be mobile or stationary. The major requirement for many practical applications is a high volumetric and/or gravimetric density. In order to increase the hydrogen density in a storage system, work must either be applied to compress the hydrogen, the temperature has to be decreased below the critical temperature or the repulsion has to be reduced by the intersection of hydrogen with another material. The second important criterion of a hydrogen storage system is the reversibility of the hydrogen uptake, i.e., subsequent release.

Currently, only a small number of hydrogen storage technologies are considered commercially feasible; namely, storage as a compressed gas up to 700 bar [9], storage as liquid hydrogen at cryogenic temperatures [10], physical adsorption on the surface of porous materials at low temperatures [11,12] or storage as chemically bound hydrogen in the form of various metal hydrides [13-17]. Alternative methods of hydrogen encapsulation are constantly emerging, based on new types of adsorbents, such as nanostructured materials [18-20] and Metal Organic Frameworks (MOFs) [21,22], or new strategies for hydrogen capture, including ambient temperature reversible hydrogenation [23,24] and the formation of clathrate hydrate structures [25]. Many other new materials and methods could potentially increase the stored hydrogen density significantly [17-22], although the majority are expensive and/or complicated. To date, none of the available technologies based on above methods have proven to be efficient in terms of the size, weight, cost and operating conditions required for practical application such as vehicle transportation. A review of the predominant storage methods is given below.

2.2.1 Compressed hydrogen storage

Hydrogen has been stored and transported in the gaseous phase in high-pressure vessels for more than a century. As long ago as 1898, 43 liters of hydrogen gas was shipped for the first time in a steel cylinder at a pressure of 140 bar [26]. The modernized storage systems consist of high-pressure gas cylinders with a maximum pressure range between 200-800 bar and a volumetric hydrogen density of around 36 kg m^{-3} [1].

Hydrogen is compressed in the same manner as natural gas. Compressors need a high quality seal to store hydrogen in cylindrical tanks at 200-250 bar due to its low density. These tanks are usually made of aluminium or carbon composites and have volumes of approximately 50 litters. They can be used in small industrial projects as well as transportation. To store compressed hydrogen in larger quantities, pressures of 500–600 bar are applied. Major drawbacks in this method are usually associated with the low density of hydrogen and with safety concerns. Heavy cylinders are now being used due to the safety concerns, which leads to a reduction in the gravimetric density in addition to the high energetic cost required to compress the gas to extremely high pressures. Pressurized hydrogen cylinders (30-70 MPa) are already available on the markets [27]. However, the compressed hydrogen storage technology continues to develop, with work primarily focused on the performance, development and optimization of the materials of the storage tank walls [28].

The effects of variations in the vessel temperature and pressure during the fast filling process have been investigated and reported recently by several authors [29-32]. In contrast, few attempts have been made to understand the behavior of hydrogen during and after accidental releases from a high pressure storage tank, which may arise from accidental damage. Cancelli *et al.* [33] developed and installed simulated codes to reduce risks due to the accidental damage to: the storage tanks, the connecting pipeline or the direct pressure relief/safety device. However, traditional compressed hydrogen gas tanks are much larger and heavier than those required for light-duty vehicles. Research studies are underway on the potential reduction of weight and volume of the compressed gas storage systems through the use of light-weight, safe, composite materials [34]

2.2.2 Cryogenic hydrogen storage

Hydrogen has been stored in liquid form for practical applications since the 1960s [35]. The liquid hydrogen is usually stored in a cryogenic tank at a temperature of 21.2 K and at ambient pressure with a volumetric density of 70.8 kg m^{-3}. In comparison, to obtain the same volumetric density, the pressure in a closed vessel at room temperature should increase to around 104 bar [11]. The development of an energy efficient liquefaction process and high performance thermal insulation of the cryogenic storage vessel are the most crucial challenges. The process is also lengthy and energy intensive since the liquefaction process of hydrogen cannot be initiated unless the temperature of hydrogen reaches 20 K.

The process of liquefaction requires a large amount of energy. The liquefaction process of hydrogen requires around 40% of the upper heating value [1] making liquid hydrogen storage a non-energy efficient process. In addition, the possible application of liquid hydrogen is limited due to the boil-off phenomenon, where the hydrogen is consumed in a relatively short period of time. These losses cause a problem for hydrogen fuel users because the fuel would be lost by evaporation even in the case when the cars are not in use [36]. Liquid hydrogen systems are conventionally open. Hence, continuous evaporation due to the low critical temperature (32 K) leads to so-called latency losses. Consequently, the majority of the theoretical and experimental work reported is entirely focused on this phenomenon. To reduce the unavoidable heat transfer leading to hydrogen loss via boil-off, a robust insulation technique is required for the storage system [37]. The performance of non-loss cryogenic vessels was studied by Li *et al.* [38]. In this study, a detail discussion pertaining to the effects of liquid volume fraction, storage pressure, environmental temperature and thermal insulation of the vessel performance was presented.

Despite the limitations mentioned above which make the process is an impractical means of hydrogen storage due to its high energy and maintenance costs, liquefied hydrogen is used in aerospace applications [38,39], due to its high energy mass ratio, which is about three times that of gasoline. For automotive applications, however, it is difficult to store sufficient amounts of hydrogen fuel due to the large and bulky insulated tank needed for its storage.

The technology of liquid hydrogen storage is well established and does not require further basic research for mass production. Nevertheless, there are number of issues related to the safety and perceptions; the practical suitability and public acceptance of liquid gas tank systems for hydrogen-driven cars are still unresolved issues.

Traditional compression and liquefaction storage methods are not widespread for practical usage due to several limitations. A cryo-compressed hybrid type of the high-pressure tank that can store the high pressure hydrogen gas under cryogenic conditions between 77 and 153 K is also potentially viable. More compact and lighter weight storage may be achievable through the use of cryo-compressed tanks [34]. For wide-ranging practical applications, however, further research is required.

A brief comparison between compressed gas and cryogenic techniques is given below:

1) Liquefied hydrogen as compared to gaseous hydrogen is denser and therefore contains more energy in a given volume. On the other hand, more energy is required for the liquefaction process.
2) Liquid hydrogen tanks have higher volumes and weights, due to the additional insulation required to prevent hydrogen loss, and may, therefore, be more costly.
3) The loss in energy during pressurization of the hydrogen gas is usually about 12-16% for compression to 800 bar compared with 40% during liquefaction.

2.2.3 Hydrogen storage in solid materials

Storage of hydrogen in a solid material under moderate temperature and pressure can combine safety with relatively high storage capacity per unit volume [1, 40-45]. It is believed to be the safest method of storage [46]. In solid-state storage, hydrogen can be stored on the surfaces of solids by adsorption. In an adsorption process, hydrogen associates with the surface of a porous material through weak dispersive interactions (physisorption), or in the form of chemical compounds via stronger chemical reactions (chemisorption).

In physisorption, hydrogen attaches to the surface of a material as hydrogen molecules (H_2) (Figure 2.2(a)). In chemisorption, often referred to as chemical hydrogen storage, hydrogen can be bound in the form of a chemical compound within the molecular structure of the material (see Figures 2.2(b), (c) and (d)). Hydrogen molecules can

dissociate into hydrogen atoms that are integrated into the solid lattice framework (Figure 2.2(b)). This method makes possible the storage of hydrogen in large quantities at low pressure and at a temperature close to ambient [47]; volumetric storage densities greater than that of liquid hydrogen can be achieved through this type of chemical bonding, since the hydrogen molecule is dissociated into atomic hydrogen.

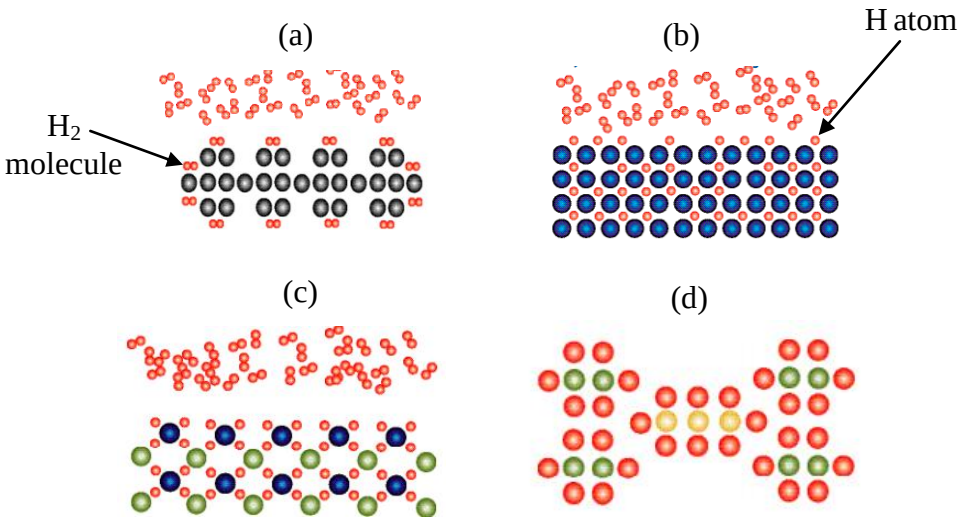

Figure 2.2: Schematic of hydrogen (a) physisorption as H_2 (b) chemisorptions via dissociation into H and incorporation into a solid-lattice framework; (c) chemisorption as complex hydride; and (d) chemisorption as a chemical hydride [47].

An efficient material is essentially characterized by a large storage capacity, rapid adsorption and discharge of hydrogen, a low weight and high reversibility. Several methods for hydrogen storage in solid materials are under investigation, including hydride formation [32,48], sequesteration within molecular cages (clathrates) [49], and adsorption in nanoporous solids [50-52]. Chemical and metal hydrides have the highest hydrogen storage capacity in materials that have been studied to date [53]. In these materials, however, adsorption is not always reversible and the desorption process usually requires a relatively high temperature [54]. Although there are many compounds with promisingly high hydrogen absorption capacities, there are still drawbacks with this method of storage. These issues are related to irreversibility and slow kinetics.

There is a growing belief that practical, low cost and efficient hydrogen storage cannot be achieved with the traditional materials and methods described thus far. This has led to a search for new materials, including composites, such as carbon based structures,

hydrogenated amorphous carbon, carbon nanostructures, zeolites, metal organic frameworks (MOFs), and boron nitride nanotubes, [55]. These materials have the potential to provide compact and lightweight hydrogen storage. A brief review of solid-state hydrogen storage methods and materials is given below. For more details, comprehensive reviews can be found in [56-59].

2.2.3.1 Chemisorption

In chemisorption processes, compounds are used to store hydrogen by bonding it chemically to the surface of the adsorbent material or through bonding with metals or liquids in the form of hydrides. This methods is rendered safe since no hydrogen can be released in the event of an accident. On the other hand, the materials are bulky, heavy and expensive. Moreover, heat is released due to the bonding of hydrogen with the material and, therefore, discharging of hydrogen requires the addition of an equivalent quantity of heat. Compared to physisorption, a higher storage capacity can be attained during chemisorption. Some of the possible candidate materials for this technique are listed below.

Metal hydrides

Metal hydrides are obtained from the reaction of hydrogen with a large number of metals in the periodic table, in addition to their alloys or inter-metallic compounds. There is a variation in the type of chemical binding forces ranging from covalent to ionic as well as multi-centred bonds and metallic bonding. Due to their remarkable impact in hydrogen storage technology, metal hydrides have gained popularity in the hydrogen storage research community in the last few years. Generally, the simplest method of storing hydrogen as a metal hydride involves the reaction of hydrogen with a metal or metal alloy (M) to form a metal hydride (MH_x) according to the following reaction:

$$M + \frac{x}{2} H_2 \rightarrow MH_x \qquad (2\text{-}1)$$

Conventional metal hydrides have been studied for various hydrogen storage applications for more than half a century. Different storage capacities and

thermodynamic properties can be observed in these materials. For example, alane (AlH_3) contains a considerable amount of hydrogen (10 wt. %), but it is impossible to produce alane directly from Al and H_2 under moderate pressures due to the weak binding energy, reflected in the low enthalpy (5–8 kJ mol^{-1} H_2) [60]. In contrast, metal hydrides such as VH_2 and $LaNi_5H_x$ have limited gravimetric densities since they contain impurities such as rare earth metals, although they may exhibit good thermodynamics ($\Delta H \cong 30–43$ kJ mol^{-1} H_2) [60].

A maximum hydrogen storage capacity of around 4 wt. % can be achieved with some conventional metal hydrides such as $LaNi_5H_6$, $FeTiH_{1.7}$ and $MgNiH_4$. Recent research on metal hydrides has focused on modifying the metal hydride compositions to achieve faster hydrogen kinetics while maintaining a desirable hydrogen gravimetric density [61].

Complex metal hydrides

Ionic hydrogen-containing complex anions such as amides [62], alanates [63] and borohydrides [64–66], together with ionic hydrogen-containing compounds mainly composed of cations of Li, Na, Mg, or Ca, are normally referred as complex hydrides. The most intensely studied metal hydrides are Lithium borohydride ($LiBH_4$) and sodium alanate ($NaAlH_4$) [67,68]. The theoretical hydrogen capacities of $LiBH_4$ and $NaAlH_4$ are 18.5 wt. % and 4-5 wt. %, respectively.

Clathrates

Hydrogen clathrates (a class of supramolecular compounds) have only recently emerged as candidate materials for hydrogen storage [69-72]. Clathrate compounds, which are cage-like host-guest structures, were one of the first supramolecular structures to be studied. Also referred to as host-guest complexes, clathrates are formed from a lattice of one molecular substance (the host) in which the molecules of a second substance (the guest) are trapped via inter-molecular interactions [73]. In the context of hydrogen storage, the guest molecule is hydrogen.

Specific examples of the hydrogen storage clathrate family are the clathrate hydrates. Clathrate hydrates are developed by applying immense pressure to water (approximately 2000 bar) at low temperature so that the structure of water becomes cage-like,

whereupon the hydrogen can be stored [74, 75]. Hydrogen can be released from the clathrate's cages by breaking the structure of these clathrates at ambient temperature and pressure. Theoretically, a considerable amount of hydrogen can be store in some clathrates. For example, 9.2 wt. % within Ar $(H_2)_2$, 5.0 wt. % within $H_2(H_2O)_2$ and 33.4 wt. % within $(H_2)_4(CH_4)$ [76].

2.2.3.2 Physisorption

As stated above, hydrogen can be stored in porous materials by means of van der Waals forces exerted by the surface of the material on the hydrogen molecules. Physisorption of hydrogen is achieved by multilayer coverage, in which the first layer is characterised by interaction between the surface and the hydrogen molecules while subsequent layers are characterised by interactions between the hydrogen molecules in adjacent layers [77]. This results from the fact that the critical temperature of hydrogen is 33 K, whereas physisorption is carried out at temperatures above 77 K for practical reasons, which rules out the possibility of volume filling and capillary condensation.

The available surface area for physisorption is an important consideration; materials with large surface areas and low densities are, therefore, of great interest [78]. There is a wide range of candidate (high surface area) materials that have dramatically different physical and chemical properties. Materials such as metal-organic frameworks [78] transition metal nitroprussides [79], carbon-based materials [80] and Prussian blue analogues [81] are of interest, by virtue not only of their high surface areas but also their high potentials for interaction between the open transition-metal ions (on the surfaces) and the molecular hydrogen.

Nitroprussides

Nitroprussides (NPs) of divalent transition metals form a family of microporous molecular materials with a diversity of crystalline structures and topologies (e.g. cubic, orthorhombic, rhombohedral, tetragonal, etc.) and an extensive range of cavities [79,82]. Chemically, they are salts of the pentacyanonitrosylferrate(II) anion $[Fe(CN)_5NO]^{2-}$, and of appropriate cations M. In this crystalline structure, only the nitrogen atoms of the cyanide group are able to link to the metal cation leaving the nitrosyl group unlinked at the oxygen atom. This results in porous materials with a network of channels that is appropriate for small molecule separation [83].

$Ni[Fe(CN)_5NO]$ and $Co[Fe(CN)_5NO]$ were two of the first materials evaluated for hydrogen storage. These materials are characterised by a cubic structure that is associated with three types of vacancies. The first is related to the absence of the building block $[Fe(CN)_5NO]$; intermediate sized vacancies are the interstitial free spaces; the third type are due to vacancies for the assembling metal. The reported hydrogen uptakes were 1.68 wt. % for Ni nitroprusside and 1.61 wt. % for Co nitroprusside at 77 K and 1 bar [84], and the maximum uptakes measured at the same temperature up to 10 bar were 7 and 5.5 wt. %, respectively [18].

Metal−Organic Frameworks

Metal–Organic Frameworks (MOFs) have been studied extensively as hydrogen storage materials over the past decade. MOFs are crystalline solids constructed from a periodic array of metal clusters linked through multi-topic organic struts [85, 86]. They can be synthesised from a wide range of multidentate ligands and metals or metal oxide clusters coordinated with organic or inorganic linkers, forming regular three-dimensional structures [18,87-89]. The ability to synthesise low-density MOFs with optimum pore sizes and shapes, together with the surface chemistry of the resulting materials, render them ideal candidates for storing hydrogen, methane or carbon dioxide [88].

MOFs can bind several molecules of hydrogen in the absence of any defects in their crystal structures. However, like all physisorption processes onto nano-materials, the intraction is relatively weak. The solid chemistry used in the building of MOF blocks has motivated the development of other highly porous crystalline materials such as Zeolitic Imidazolate Frameworks (ZIFs) [90] and Covalent Organic Frameworks (COFs) [91]. Furthermore, recent theoretical studies have shown that modifying lightweight MOFs by penetrating them with metal ions such as those of Li, has the potential to increase hydrogen uptake by increasing the hydrogen binding energy [88,89,92-95].

The first reported results of hydrogen adsorption uptake on a MOF was 4.5 wt. % at 77 K and pressures less than 1 atm, and 1.0 wt. % at room temperature at 20 bar on MOF-5 and IRMOF-1 [96]. Higher recorded hydrogen capacities at 77 K are: 7.5 wt. % at 70 bar in MOF-177; 3.1 wt. % at 55 bar in ZIF-8; 5.2 wt. % at 48 bar in MOF-5; 9.95 wt.

% at 56 bar in NU-100 with a total capacity of 16.4 wt. % at 70 bar [97]. The highest total H_2 storage capacity reported so far is 17.6 wt. % (excess 8.6 wt. %) in MOF-210 at 77 K and 80 bar [94,98]

Carbon based materials

Along with the recent advances in nanotechnology, hydrogen technology researchers are now looking towards developing efficient, reasonably inexpensive nano-materials with large internal surfaces, which can be built from lightweight elements, for hydrogen storage systems. Carbon-based materials, which can be synthesized from a variety of organic precursors, can be designed with a range of structures: carbon nanotubes, carbon fibres, carbon fullerenes and activated carbons [53-58,99].

Carbon nano materials such as single-walled carbon nanotubes (SWNT) have been investigated extensively as hydrogen storage materials [100-108]. Chen *et al.* [108] measured the hydrogen uptake of 14 nanostructured samples of graphite, activated carbons, graphitic nanofibres and SWNTs at different pressure and temperature conditions. Their recorded results were less than 1 wt. % for all samples and less than 0.1 wt. % for SWNTs at 295 K and 80 bar. The highest value observed was 2.9 wt. % (at 80 bar and 295 K). Similarly, the uptake in 60 samples of carbonaceous materials was measured by Zuttel *et al.* [109] for hydrogen adsorption at 293 K. The results showed low hydrogen uptake in some samples. For example, the amount of reversibly stored hydrogen in graphite samples ranged from 0.04 to 0.46 wt. % at the studied temperature of 293 K. For MWNTs, the maximum capacities ranged from 0.09 to 0.36 wt. %, while for different SWNT samples, values between 0.18 and 0.9 wt. % were measured. Carbon fibres showed the maximum uptake of around 1.2 wt. %.

Metal-Cyanide Frameworks

Microporous solid materials based on Metal-Cyanide Frameworks (MCF), particularly Prussian Blue (PB) analogues of the type $M_x[T(CN)_6]_y$, where M (T) is the external (internal) metal, form an important class of insoluble, mixed-valance compounds. MCFs have wide range of applications in magnetic materials [110,111], molecular sieves [112], some catalytic processes [113,114], ion exchange [115], solid state batteries, biosensors [116], and as medical treatments for animals and humans affected by nuclear

radiation [117,118]. All these potential applications are related to the crystal structures of PB analogues, which are known for only a few compositions. Research has tended to focus on the properties of bulk PB and its analogues. In recent years, however, nano-scale PB materials, with properties different from the bulk forms, have emerged as promising materials for a variety of applications [119].

The potential applications of PB analogues include H_2 storage. This is primarily due to the simplicity of their synthesis, the wide range of suitable metals available, their low framework densities, and their potentially high surface areas [120-123]. Typically, the solid PB materials consist of cubic shaped polycrystalline particles of sub-micrometre size [19,20,124]. In the general PB analogue structure, $[T(CN)_6]^{n-}$ complexes are linked by octrahedrally (or tetrahedrally) coordinated nitrogen-bound M^{2+} ions. Cavities in the structure, resulting from the presence of vacancies, house water molecules that can be removed upon heating, while the MCF is left intact. Combining $[T(CN)_6]^{3-}$ (hexacyanometalate) complexes with M^{2+} ions can lead to hydrated PB analogues of the type, $M_3[T(CN)_6]_2.x$H2O, which can feature vacancies at up to one third of the hexacyanometalate sites. When the PB analogue is dehydrated, hydrogen can interact with the coordinatively-unsaturated M^{2+} sites and possibly also with the polarisable electron clouds of the cyanide bridges [125]. The transport of molecular hydrogen in such large microporous crystals can limit the charge-discharge rates of possible storage devices.

Titanate nanotubes

Following the discovery of carbon nanotubes, attempts have been made to synthesise of micro- and nanotubes of metal oxides such as titanium oxide (TiO_2), using a variety of methods. Titanate nanotubes (TiNTs), nanofibers, and other one-dimensional nanostructures of titanium compounds have attracted considerable attention as a promising new class of materials for a wide range of applications. This is primarily due to the simplicity of preparation routes, the uniform and controllable structures and high surface areas [126]. Among these structures, TiNTs have been the most widely studied due to their unique combination of physico-chemical and structural properties [127]. These multilayered nanomaterials have well developed lamellar structures, in the form of certain crystal structures: $H_2Ti_3O_7$, $H_2Ti_2O_4(OH)_2$, $H_2Ti_4O_9.xH_2O$ or TiO_2-B [126]. Among the properties and characteristics of these mesoporous materials are: good

stability at high temperatures; high proton conductivity; high ion-exchange capacity for cations of different metals, and high specific surface area [126]. Potential applications include electrochromism, [127], bonelike apatite formation [128], proton conduction, photoinduced hydrophilicity, photocatalysts [129], dye-sensitized solar batteries [130], and hydrogen sensors [11]. In the present context, TiNTs exhibit a moderate capacity for hydrogen storage [31,32,131].

Many methods have been proposed for the synthesis of TiNTs, including electrochemical methods, the hydrothermal method, the sol–gel method and templating [126,132]. The hydrothermal method is used widely for synthesising metal oxide nanostructures since it can provide well-dispersed crystallised products with a tuneable morphology. Furthermore, the surface properties can be tuned by varying the solution composition, reaction temperature, pressure, solvent properties, additives and aging time. The alkaline hydrothermal method is well-suited to the synthesis of metal oxide nanostructures due to its low cost and simple chemistry, which does not require any special chemicals or expensive laboratory equipment. The first discovery of a simple method for TiNT preparation was made by Kasuga *et al.* in 1998 [133]. In this method, amorphous titanium oxide (TiO_2) was treated with a concentrated solution of sodium hydroxide. Recently, the hydrothermal method has been modified by Bavykin *et al.* [134] through the treatment of TiO_2 with a concentrated mixture of NaOH/KOH solution under hydrothermal reaction at moderate temperatures and atmospheric pressure. The resulting titanate nanotubes were pure Na-titanate ($Na_2Ti_3O_7$).

One of the characteristic properties of TiNTs is their good ion-exchange ability [135]. It is possible to exchange the Na^+ cations with H^+ ions after washing with dilute HCl acid, which yields protonated TiNT: H-TiNT (H_2Ti_3O7) [136]. Other metal cations, such as Ni^{2+}, Co^{2+}, Cu^{2+}, Cd^{2+}, Zn^{2+} and Ag^+, can be incorporated into the titanate structure using, e.g., an aqueous ammonia solution [137,138]. The resulting TiNTs exhibit modified magnetic and optical properties, with potential applications in catalysis, photocatalysis and adsorption.

PB/TiNTs composites

The transport of molecular hydrogen in large microporous crystals such as those of PB analogues can limit the charge-discharge rates of possible storage devices. One of the methods to stabilize the small nanoparticles of PB-type materials is their deposition onto the surface of a suitable support such as nanotubular titanates [139-141]. Indeed, due to the high specific surface area and good ion-exchange properties [134,142] TiNTs offer a convenient route for uniform deposition of PB nanoparticles on their surface.

Early studies have shown that ion exchange of TiNTs with Fe^{2+} followed by reaction with $K_3[Fe(CN)_6]$ results in the formation of spheroidal nanoparticles of PB, with diameters in the range 10 to 30 nm [143]. These PB particles are characterised by good interaction with TiNTs [144] (as well as with other metal oxide supports such as ZnO [145] and SnO_2 [146]) resulting in low rates of Fe^{II} ion leakage into the solution and efficient electrical contact between nanoparticles and the support, improving the electrocatalytic properties of the composite. Although, pure TiNTs exhibit only moderate values of hydrogen uptake (ca 4 wt. % at 77 K [131]), due to the high atomic weight of the titanium atoms, there are some indications that this value can be increased by the intercalation of transition metals between the layers of the TiNTs [147,148].

2.3 Summary

To summarize, several technical limitations of traditional compression and liquefaction storage methods render them impractical for widespread application. The storage of gaseous hydrogen is mainly restricted by very large volume requirements due to the relatively low density of hydrogen gas even at high pressures, resulting in high material costs. Although liquid hydrogen solves the problem of size, the energy cost associated with the cryogenic liquefaction process represents around 40% of the generated energy. To store sufficient quantities of hydrogen at high densities and in a safe manner, physical and chemical approaches are used to host hydrogen by means of hydrogen−solid interactions.

Chemical and metal hydrides have the highest hydrogen storage capacity in materials that have been reported up to date. Nevertheless, hydrogen stored as hydrides usually requires a relatively high sorption temperature and is not always reversible. However, hydrogen storage in solid materials offers great promise, but additional research is

required to better understand the mechanism of hydrogen storage under practical operating conditions and to tackle some of the difficulties and critical challenges related to capacity, the uptake and release of hydrogen (i.e., kinetics), management of heat during refuelling, cost, and life cycle impacts.

Finally, comparisons between the three storage options shows that solid-state storage offers many advantages compared to other storage methods: lower volume, lower pressure and higher energy efficiency (see Figure 2.3). Compressed gas and liquid hydrogen storage are, however, the only commercially viable options today. In an effort to present an overview, the achievable storage capacities of different hydrogen storage methods have been summarized in Figure 2.3 [149].

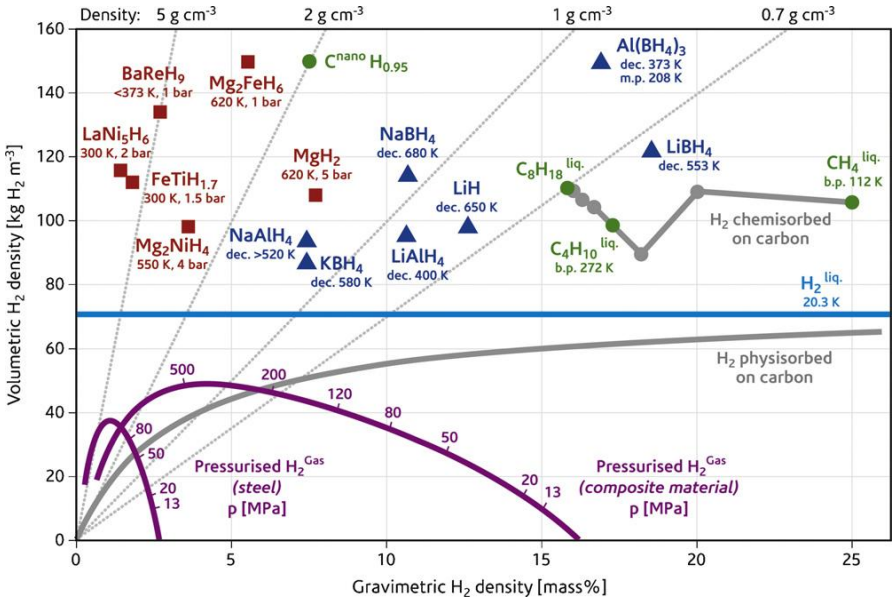

Figure 2.3: Storage capacities of different hydrogen storage methods and materials [149].

From this figure it can be observed Mg_2FeH_6 exhibits the highest known volumetric hydrogen density, 150 kg m^{-3}, which is more than double that of liquid hydrogen. $LiBH_4$, on the other hand, exhibits the highest gravimetric hydrogen density of 18 wt %.

References

[1] Züttel A., Borgshulte A., Schlapbach L., Hydrogen as a future energy carrier. Wiley VCH; 2008 .

[2] Edwards P.P., Kuznetsov V.L., David W.I.F., Brandon N.P., Energy Policy 36 (2008) 4356–4362.

[3] Edwards P.P., Kuznetsov V.L., David W.I.F., Phil. Trans. R. Soc. A 365 (2007) 1043–1056.

[4] Elisabet T.R., Preben F.H., Vie J.S., Ulleberg O., HIA-HCG Production, Technical Report, March 2005.

[5] Milbrandt A. and Mann M., Technical Report NREL/TP-560-42773 February 2009.

[6] Haryanto A., Fernando S., Murali N., Adhikari S., Energy and Fuels, 19 (2005) 2098–2106.

[7] Sen U., Skakdwipee M., Banerjee R., J. Sci. Ind. Res. 67 (2008) 980–993.

[8] Arean C. O., Bonelli B., Delgado M. R., Garrone E., Turk J. Chem. 33, (2009) 599–606.

[9] Thomas C.E., Int. J. Hydrogen Energy, 34 (2009) 6005–6020.

[10] Hirose K., Phil. Trans. Roy. Soc., A 368 (2010) 3365–3377.

[11] Zhou L., Renew. Sustain. Energy Rev., 9 (2005) 395–408.

[12] Kumar V.S., Raghunathan K., Kumar S., Int J Hydrogen Energy, 34 (2009) 5466–5475.

[13] Orimo S.I., Nakamori Y., Eliseo JR., Zuttel A., Jensen C.M., Chem. Rev. 107 (2007) 4111–4132.

[14] Xiong Z., Young C.K., Wu G., Chen P., Shaw W., Karkarmar A., Nat. Mater., 7 (2008) 138–141.

[15] Bhatia S.K., Myers A.L., Langmuir 22 (2006)1688–1700.

[16] Liu Y., Kabbour H., Brown C.M., Neumann D.A., Ahn C.C., Langmuir, 24 (2008) 4772–4777.

[17] Reguera L., Balmaseda J, Krap CP, Reguera E., J. Phys. Chem. C ,112 (2008) 10490–10501.

[18] Reguera L., Roque J., Hernandez J., Reguera E., Int. J. Hydrogen Energy 35 (2010) 12864–12869.

[19] Krap C.P., Balmaseda J., del Castillo L.F., Zamora B, Reguera E., Energy & Fuels, 24 (2010) 581–589.

[20] Avila M., Reguera L., Rodriguez-Hernandez J., Balmaseda J., Reguera E., J. Solid State Chem., 181 (2008) 2899–2907.

[21] Murray L.J., Dinca M., Long JR., Chem. Soc. Rev., 38 (2009) 1294–1314.

[22] Fletcher A.J., Thomas K.M., Rosseinsky M.J., J. Solid State Chem. 178 (2005) 2491–2510.

[23] Crabtree R.H., Energy Environ. Sci., 1 (2008) 134–138.

[24] Eblagon K.M., Rentsch D., Friedrichs O., Remhof A., Zuettel A., Ramirez-Cuesta A.J., Int J. Hydrogen Energy 35 (2010) 11609–11621.

[25] Strobel T.A., Taylor C.J., Hester K.C., Dec S.F., Koh C.A., Miller K.T., J. Phys. Chem. B 110 (2006) 17121–17125.

[26] McAlister R., Natural Science 1 (1999) 164–172.

[27] Greenwood N.N., and Earnshaw A., (1997) Chemistry of the Elements, Butterworth-Heinemann , Oxford; Boston.

[28] Cumalioglu I., Modeling and simulation of high pressure hydrogen storage tank with dynamic wall, (2005) PhD Thesis, Graduate Faculty, Texas Tech. University.

[29] Züttel A., Nützenadel Ch., Sudan P., Mauron Ph., Emmenegger Ch., Rentsch S., Schlapbach L., Weidenkaff A., Kiyobayashi T., J. Alloys Compounds 330-332 (2002) 676–682.

[30] Lamari Darkrim F., Malbrunot P., Tartaglia G.P., Int. J. Hydrogen Energy 27 (2002) 193–202

[31] Fakioglu E., Yürüm Y., Nejat Veziroglu T., Int. J. Hydrogen Energy 29 (2004) 1371–1376.

[32] Sakintuna B., Lmari-Darkrim F., Hirscher M., Int. J. Hydrogen Energy 32 (2007) 1121-1140.

[33] Cancelli C., Demichela M., Piccinini N., Cryogenics 45 (2005) 481–488.

[34] DOE technical report, Energy efficiency and renewable energy, Jan. 2011.

[35] Sherif S.A., Zeytinoglu N., Veziroglu T.N., Int. J. Hydrogen Energy 22 (1997) 683–688.

[36] Pehr K., Int. J. Hydrogen Energy 21 (1996) 387–395.

[37] Pehr K., Int. J. Hydrogen Energy 18 (1993) 773–781.

[38] Schmidtchen U., Behrend E., Pohl H.W., Rostek N., Renew. Sust. Energy Rev. 1 (1997) 239–269.

[39] Trouillet A., Marin E., Veillas C., Meas. Sci. Technol. 17 (2006) 1124–1128.

[40] Jochem E., Energy Environ. 2 (1991) 31–44.

[41] Gross K., The reversible hydride solution for hydrogen storage, G-CEP Hydrogen workshop, April 14–15, 2003 California. USA.

[42] Ogden J.M, (2001), The International Energy Agency, Golden, IEA/H2/TR02/002.

[43] Dunn S., Worldwatch Paper 157 (2001), Worldwatch Institute, Washington, DC.

[44] Solomon B.D., Banerjee A., Energy Policy 34 (2006) 781–792

[45] Evenson W.E., R&D of Energy technologies report Annex IV-Section 1 (2005) 209–215.

[46] Zhang J., Fisher T.S., Ramachandran P.V., Gore J.P., Mudawar I., J. Heat Trans. 127 (2005) 1391–1399.

[47] DOE, Hydrogen Storage: Basics, EERE - U.S. Department of Energy. 2008.

[48] Biniwale R.B., Rayalu S., Devotta S,. Ichikawa M., Int. J. Hydrogen Energy 33 (2008) 360–365.

[49] Di Profio P., Arca S., Rossi F., Filipponi M., Int. J. Hydrogen Energy 34 (2009) 9173–9180.

[50] Yuruma Y., Taralp A., Veziroglu T.N., Int. J. Hydrogen Energy 34 (2009)3784–3798.

[51] Li Y., Liu Y., Wang Y., Leng Y., Xie L., Li X., Int. J. Hydrogen Energy 32 (2007) 3411–3415.

[52] Li J., Cheng S., Zhao Q., Long P., Dong J., Int. J. Hydrogen Energy, 34 (2009) 1377–1382.

[53] Chen P., Xion Z.J., Luo J., Lin J., Tan L.K., J. Phys. Chem. B 107 (2003) 10967–10970.

[54] Janot R., Eymery J.B., Tarascon J.M., J. Phys. Chem. C 111 (2007) 2335–2340.

[55] Westerwaal R.J., Haije W.G., ECN-E-08-043, April 2008.

[56] Chaudhuri S., Muckerman J.T,. J. Phys. Chem. B 109, No. 15 (2005) 6952–6957.

[57] Bus E., van Bokhoven J.A., J. Phys. Chem C 9 (2007) 2894–290.

[58] Dzhurakhalov A.A., Peeters F.M., Carbon 49 (2011) 3258–3266.

[59] Maiti A., Chemical Phys. Lett. 508 (2011) 107–110.

[60] Yang J., Sudik A., Wolverton C., Siegel D.J., Chem. Soc. Rev. 39 (2010) 656–675.

[61] van den Berg A.W.C., Arean C.O., Chem. Commun. (2008) 668–681.

[62] Chen P., Xiong Z.T., Luo J.Z., Lin J.Y., K Tan. L., Nature 420 (2002) 302–304.

[63] Bogdanovic B., Schwickardi M., J. Alloys Compd., 253-254 (1997) 1–9.

[64] Zuttel A., Rentsch S., Fisher P., Wenger P., Sudan P., Mauron Ph., Emmenegger Ch., J. Alloys Compd. 515 (2003), 356–357.

[65] Zuttel A., Wenger P., Rentsch S., Sudan P., J. Power Sources 118 (2003) 1–7.

[66] Nakamori Y., Li H., Miwa K., Towata S., Orimo S., Mater.Trans. 47 (2006) 1898–1901.

[67] Ross D.K., Vacuum 80 (2006) 1084–1089.

[68] Parker S.F., Coordination Chemistry Reviews 254 (2010) 215–234.

[69] Dyadin Y.A., Larionov E.G., Manakov A.Y., Zhurko, F.V., Aladko E. Y., Mikina, T.V., Komarov V.Y., Mendeleev Comm. (1999) 209–210.

[70] Mao W.L., Mao H.K., Goncharov A.F., Struzhkin, V.V., Guo Q., Hu, J., Shu, J., Hemley R.J., Somayazulu, M., Zhao Y., Science 297 (2002) 2247–2249.

[71] Mao W.L., Mao H.K., Proc. Natl. Acad. Sci. 101 (2004) 708–710.

[72] Strobel T.A., Kim Y., Andrews G.S., Ferrell III J.R., Koh C.A., Herring A.M., Sloan E.D., J. Am. Chem. Soc. 130 (2008) 14975–14977.

[73] Powell, H.M., J. Chem. Soc. (1948) 61–73.

[74] Patchkovskii S., Tse J.S., Proc. Natl. Acad. Sci. 100 (2003) 14645–14650.

[75] Russina M., Ewout K., Celli M., Ulivi L., Mezei F., Journal of Physics, Conference Series 177 (2009) 12–13.

[76] Struzhkin V.V., Militzer B., Mao W.L., Mao H.K., Hemley R.J., Chem. Rev. 107 (2007) 4133−4151.

[77] Zhou L., Renew. Sust. Energy Rev. 9 (2005) 395–408.

[78] Murray L.J., Dinca M., Long JR., Chem. Soc. Rev. 38 (2009) 1294-1314.

[79] Reguera L., Balmaseda J., Krap C.P., Reguera E., J. Phys. Chem. B 112 (2008) 10490-10501.

[80] Strobel R., Garche J., P.T. Moseley, Jorissen L., Wolf G., Journal of Power Sources 159 (2006) 781–801.

[81] Krap C.P., Balmaseda J., Zamora B., Reguera E., Int. J. Hydrogen Energy 35 (2010) 10381–10386.

[82] Balmaseda J., Reguera E., Gomez A., Roque J., Vazquez C., Autie M., J. Phys. Chem. B 107 (2003) 11360−11369.

[83] Boxhoorn G., Moolhuysen J., Coolegem J.P.G., van Santen R.A., J. Chem. Soc. Chem. Commun., (1985) 1305–1307.

[84] Culp J.T., Matranga C., Smith M., Bittner E.W., Bockrath B. J. Phys. Chem. B. 110 (2006) 8325–8328.

[85] Maiti A., Chem. Phys. Lett. 508 (2011) 107–110.

[86] Slattery D.K., Hampton M.D., Proceedings of the 2002 US DOE Hydrogen Program Review, NREL/CP-610-32405, Florida (2002).

[87] Kondo M., Yoshitomi T., Seki K., Matsuzaka H., Kitagawa S., Angew. Chem. Int. Ed. 36 (1997) 1725–1727.

[88] Thomas K.M., Dalton Trans. (2009)1487–1505.

[89] Yaghi O.M., O'Keeffe M, Ockwig N.W., Chae H.K., Eddaoudi M., Kim J., Nature 423 (2003) 705–714.

[90] Park K.S., Ni Z., Cote A.P. , Choi J.Y., Huang R., UribeRomo F. J., . Chae H.K, O'Keeffe M, Yaghi O. M., Proc. Natl. Acad. Sci. U. S. A., 103 (2006) 10186–10191.

[91] Cote A.P., Bennin A.I., Ockwig N.W., O'Keeffe M., Matzger A.J., Yaghi O. M., Science 310 (2005) 1166–1170.

[92] Han S., Goddard III W., J. Am. Chem. Soc. 129 (2007) 8422–8423.

[93] Blomqvist A., Araujo C.M., Srepusharawoot P., Ahuja R., Proc. Natl. Acad. Sci. U.S.A. 104 (2007) 20173–20176.

[94] Suh M.P., Park H.J., Prasad T.K., Lim D.W., Chem. Rev. 112 (2012) 782–835.

[95] Collins D.J., Zhou H.C.J. Mater. Chem., 17 (2007) 3154–3160.

[96] Rosi N.L., Eckert J., Eddaoudi M., Vodak D. ., Kim J., O'Keefe M., Yaghi O.M., Science 300 (2003) 1127–1129.

[97] Farha O.K., Yazaydin A.O., Eryazici I., Malliakas C.D., Hauser B.G., Kanatzidis M.G., Nguyen S.T., Snurr R.Q., Hupp J.T., Nat. Chem. 2 (2010) 944–948.

[98] Furukawa, H., Ko, N., Go, Y. B., Aratani, N., Choi, S. B., Choi, E., Yazaydin, A. O., Snurr, R. Q., O'Keeffe, M., Kim, J., Yaghi, O. M., Science 329 (2010) 424–428.

[99] Li, Y., Liu Y., Wang Y., Leng Y., Xie L., Li X., Int. J. Hydrogen Energy 32 (2007) 3411−3415.

[100] Chen P., Wu X., Lin J., Tan K. L., Science 285 (1999) 91–93.

[101] Liu C., Fan Y.Y., Liu M., Cong H.T., Cheng H.M., Dresselhaus M.S., Science 286 (1999) 1127–1129.

[102] Yang R., Carbon 38 (2000) 623–626.

[103] Lee E., Kim Y., Jin Y., Chang K., Phys. Rev. B 66 (2002) 73415–73415.

[104] Kim Y.H., Zhao Y., Williamson A., Heben M.J., Zhang S.B., Phys. Rev. Lett. 96 (2006) 16102–16106.

[105] Sun Q., Jena P., Wang Q., Marquez M., J. Am. Chem. Soc. 128 (2006) 9741–9745.

[106] Chandrakumar K.R.S., Ghosh S.K., Nano Lett. 8 (2008) 13–19.

[107] Sun Q., Wang Q., Jena P., Appl. Phys. Lett. 94 (2009) 013111–013113.

[108] Chen X., Dettlaff-Weglikowska U., Haluska M., Hulman M., Roth S., Hirscher

M., Becher M., Mater. Res. Soc.Symp. Proc. (2002) 796.

[109] Zuttel A., Sudan P., Mauron Ph., Kiyobayashi T., Emmenegger Ch., Schlapbach L., Int. J. Hydrogen Energy 27 (2002) 203–212.

[110] Zhou, P.H., Xue, D.S., Luo, H.Q., Chen, X.G., Nano Lett., 2 (2002) 845–847

[111] Berseth P.A., Sokol J.J., Shores M.P., Heinrich J.L., Long J.R. , J. Am. Chem. Soc. 122 (2000) 9655–9662.

[112] Pyrasch M., Toutinanoush A., Jin W., Schnepf J., Tieke B., Chem. Mater. 15 (2003) 245–254.

[113] Kuyper J., Boxhoorn G., J. Catal. 105 (1987) 163–174.

[114] Reguera E., Fernández J., Duque J., Polyhedron 13 (1994) 479–484.

[115] Ayrault S., Jimenez B., Garnier E., Fedoroff M., Jones D.J., Loss-Neskovic C., J. Solid State Chem. 141 (1998) 475–480.

[116] Moscone D., D'Ottavi D., Compagnone D., Palleschi G., A. Amine, Anal. Chem. 73 (2001) 2529–2535.

[117] Arnaud M.J., Clement C., Getaz F., Tannhauser F., Schoenegge R., Blume J., Giese W., J. Dairy Res. 55 (1988) 1–13.

[118] Roberts L., Science 238 (1987) 1028–1031.

[119] Vien V., Minh N.V., Lee H.I., Kim J.M., Kim Y., Kim S.J., Mater. Chem. and Phys, 107 (2008) 6–8.

[120] Kaye S.S., Long JR., Catal. Today 120 (2007) 311–316.

[121] Reguera L., Krap C.P., Balmaseda J., Reguera E., J. Phys. Chem. C 112 (2008) 15893–15899.

[122] Jimenez-Gallegos J., Rodriguez-Hernandez J., Yee-Madeira H., Reguera E., J Phys Chem. C 114 (2010) 5043–5048.

[123] Yuan A.H., Chu C.X., Zhou H., Yuan P., Liu K.K., Li L., Eur. J. Inorg. Chem. 6 (2010) 866–871.

[124] Krap C.P., Zamora B., Reguera L., Reguera E., Microporous Mesoporous Mater. 120 (2009) 414–420.

[125] Kaye S.S., Long JR., J. Am. Chem. Soc. 127 (2005) 6506–6507.

[126] Bavykin D.V., Walsh F.C., Titanate and Titania Nanotubes: Synthesis, Properties and Applications. First ed 2009, Cambridge, UK: Royal Society of Chemistry.

[127] Tokudome H., Miyauchi M., Angew. Chem., Int. Ed., 44 (2005) 1974–1977.

[128] Kubota S., Johkura K., Asanuma K., Okouchi Y., Ogiwara N., Sasaki K., Kasuga

T., J. of Mater. Sci.15 (2004) 1031–1035.

[129] Tokudome H. , Miyauchi M., Chem. 33Lett (2004) 1108–1109.

[130] Uchida S., Chiba R., Tomiha M., Masaki N., Shirai, M., Electrochemistry 70 (2002) 418–420.

[131] Bavykin D.V., Lapkin A.A., Plucinski P.K., Friedrich J.M., Walsh F.C., J. Phys. Chem. B 109 (2005)9422–19427.

[132] Zhou W., Liu H., Boughton R.I., Du G., Lin J., Wang J., Liu D., J. Mater. Chem., 20 (2010) 5993–6008.

[133] Kasuga, T., Hiramatsu, M., Hoson, A., Sekino, T., Niihara, K., Langmuir 14 (1998) 3160–3163.

[134] Bavykin, D.V., Cressey, B.A., Light, M.E., Walsh, F.C., Nanotechnology 19 No. 27 (2008) 275604–275609.

[135] Sun X., Li Y., Chem. Eur. J. 9 (2003) 2229–2238.

[136] Ou H.H., Lo S.L., Separation and Purification Technology 58 (2007) 179–191.

[137] Li H., Zhang Y., Huang W., Nano Biomed. Eng. 1 (2009) 32–37.

[138] Sun X.M, Li Y.D, Chem. Eur. J. 9 (2003) 2229–2238.

[139] Chen X., Mao S.S., Chem. Rev. 107 (2007) 2891–2959.

[140] Bavykin D.V., Walsh F.C., Eu. J. Inorg. Chem. 8 (2009) 977–997.

[141] Chen Q., Peng L.M., Int. J. Nanotechnology 4 (2007) 44–65.

[142] Bavykin D.V., Walsh F.C., J. Phys. Chem. C 111 (2007) 14644–14651.

[143] Ivekovic D., Gajovic A., Ceh M., Pihlar B., Electroanalysis 22 (2010) 2202–2210.

[144] Lin L., Huang X., Wang L., Tang A., Solid State Sci. 12 (2010)1764–1769.

[145] Chu H.W., Thangamuthu R., Chen S.M., Electroanalysis 19 (2007)1944–1951.

[146] Rong Y., Kim S., Su F., Myers D., Taya M., Electrochim. Acta 56 (2011) 6230–6236.

[147] Qamar M., Kim S.J., Ganguli A.K., Nanotechnology 20 (2009) 455703–455708.

[148] Chen J., Li S.L., Tao Z.L., Shen Y.T., Cui C.X., J. Am. Chem. Soc.125 (2003) 5284–5285.

[149] Züttel, A., Materials today 6 (2003) 24-33.

Chapter 3: Materials and methods

3.1 Materials

The materials considered in this thesis are: the PB analogue $Cu_3[Co(CN)_6]_2$ (CoIIICu); the metal nitroprussides (NP) of $Ni_3[Fe(CN)_5NO]$ and $Co_3[Fe(CN)_5NO]$; the Metal-Organic Framework (MOF) $Cu_3(BTC)_2$; Cadmium Ferricyanide $Cd_3[Fe(CN)_6]_2$ (Cd_3Fe^{III}); titanate nanotubes (TiNTs); and hexacyanomettalates M_3Fe^{III}/TiNTs composites (M refers to the transition metals of Fe, Ni, Co, Cu, Cd, Zn, or Mn). The reagents used were analytical grade, obtained from Sigma-Aldrich and Evonik Degussa GmbH as listed in Table 3.1.

Table 3.1: List of materials used and their specifications.

Material	Supplier	Specifications
AEROXIDE ® TiO_2 P25 CAS-No. 13463-67-7 EC-No. 236-675-5	Evonik Degussa GmbH	Formula : TiO_2 Molecular Weight : 40.00 g mol^{-1} Form: powder Colour: white Density 3.8 g cm^{-3}
Hydrochloride Acid, 37% CAS-No. 7647-01-0 EC-No. 231-595-7 Index-No. 017-002-01-X	Sigma-Aldrich	Formula : HCl Molecular Weight : 36.46 g mol^{-1} Form: liquid Colour: light yellow Relative density: 1.18 g mL^{-1} at 25 °C
Sodium Hydroxide, pellets 97% CAS-No. 1310-73-2 EC-No. 215-185-5 Index-No. 011-002-00-6	Sigma-Aldrich	Formula : NaOH Molecular Weight : 40.00 g mol^{-1} Appearance Form: pellets Colour: white Bulk density 2.130 g cm^{-3}
Iron (II) Sulfate heptahydrate CAS-No. 7782-63-0 EC-No. 231-753-5 Index-No. 026-003-01-4	Sigma-Aldrich	Formula : $FeSO_4 \cdot 7H_2O$ Molecular Weight : 278.01 g mol^{-1} Form: solid pH 3.0 - 4.0 at 50 g/l at 25 °C Bulk density 1.300 g cm^{-3}
Nickel (II) Sulfate heptahydrate CAS-No. 10101-98-1 EC-No. 232-104-9 Index-No. 028-009-00-5	Sigma-Aldrich	Formula : $NiSO_4 \cdot 7H_2O$ Molecular Weight : 280.86 g mol^{-1} Form: crystalline Relative density 1.948 g cm^{-3} at 25 °C

Cobalt (II) Sulfate heptahydrate CAS-No. 10026-24-1 EC-No. 233-334-2 Index-No. 027-005-00-0	Sigma-Aldrich	Formula : $CoSO_4 \cdot 7H_2O$ Molecular Weight : 281.10 g mol^{-1} Form: crystalline Colour: red Bulk density 0.9 g L^{-1}
Copper (II) Sulfate CAS-No. 7758-98-7 EC-No. 231-847-6 Index-No. 029-004-00-0	Sigma-Aldrich	Formula : $CuSO_4$ Molecular Weight : 159.61 g mol^{-1} Form: powder Colour: light grey Bulk density 1.000 g cm^{-3}
Cadmium (II) Sulfate hydrate CAS-No. 15244-35-6 EC-No. 233-331-6 Index-No. 048-009-00-9	Sigma-Aldrich	Formula : $CdSO_4 \cdot H_2O$ Molecular Weight : 208.47 g mol^{-1} Form: powder Relative density 3.090 g cm^{-3}
Zinc (II) Sulfate heptahydrate CAS-No. 7446-20-0 EC-No. 231-793-3 Index-No. 030-006-00-9	Sigma-Aldrich	Formula :$ZnSO_4 \cdot 7H_2O$ Molecular Weight : 287.56 g mol^{-1} Form: Crystals with lumps Colour: white Water solubility 965 g L^{-1} at 20 °C
Manganese (II) Sulfate hydrate CAS-No. 15244-36-7 EC-No. 232-089-9 Index-No. 025-003-00-4	Sigma-Aldrich	Formula : $MnSO_4 \cdot H_2O$ Molecular Weight : 151.00 g mol^{-1} Form: solid Relative density 2.090 g cm^{-3}
Potassium hexacyanoferrate(III) CAS-No. 13746-66-2	Sigma-Aldrich	Formula : $K_3Fe(CN)_6$ Molecular Weight : 329.24 g mol^{-1} Form: crystalline Colour: red Relative density 1.890 g cm^{-3}

The samples were prepared and characterized according to the procedures described below.

3.1.1 Preparation of $Cu_3[Co(CN)_6]_2$

In the well-known synthetic route [1, 2], 0.01 mol dm^{-3} aqueous solutions of potassium hexacyanocobalate $K_3[Co(CN)_6]$ were mixed with 0.01 mol dm^{-3} of $CuSO_4$ solution. The resulting blue coloured precipitate was aged within the mother liqueur solution for 48 hr at room temperature. The formed precipitates were washed successively with distilled water, followed by atmospheric air-drying until a constant weight was obtained.

3.1.2 Preparation of $Ni_3[Fe(CN)_5NO]$ and $Co_3[Fe(CN)_5NO]$

The procedure described above was also used for the preparation of NP samples ($Ni_3[Fe(CN)_5NO]$ and $Co_3[Fe(CN)_5NO]$) by mixing 0.01 mol dm^{-3} aqueous solutions of

sodium nitroprusside ($Na_2[Fe(CN)_5NO]\cdot 2H_2O$) with excess amounts of solutions of sulphate (of the divalent transition metals involved (Co and Ni)). The use of the metal solution in excess relative to the complex anion guarantees that only one phase of the metal is produced.

3.1.3 Preparation of $Cu_3(BTC)_2$

A commercial grade of $Cu_3(BTC)_2$ obtained from Sigma-Aldrich laboratory was used as an example of the MOF family. The preparation procedure for $Cu_3(BTC)_2$ using methanol solvent (CuBTC-MeOH) can be found in Liu *et al.* [3].

3.1.4 Synthesis of titanate nanotubes (TiNTs)

TiNTs in the protonated form were prepared by alkaline hydrothermal reaction at atmospheric pressure using an aqueous mixture of NaOH and KOH [4]. 25 g of TiO_2 powder was dispersed in a mixture of 240 cm^3 of 10 mol dm^{-3} NaOH and 10 cm^3 of 10 mol dm^{-3} KOH aqueous solution in a PFA round-bottom flask and refluxed for 72 hrs at around 110 °C and atmospheric pressure. The resulting product was cooled to room temperature and washed with water repeatedly until the washing water pH values ranged between 7 and 8. In order to convert TiNTs into its protonated form (H-TiNT), 0.1 mol dm^{-3} HCl solution was added drop-wise until a constant pH value of 2 was attained, followed by water washing to achieve a pH of 5. The sample was filtered and vacuum dried overnight at ambient temperature.

3.1.5 Synthesis of $Cd_3[Fe(CN)_6]_2$

The bulk nanoparticles of $Cd_3[Fe(CN)_6]_2$ were prepared using the methods in [5]. In a typical synthesis, 50 cm^3 of 0.2 mol dm^{-3} $CdSO_4$ was mixed with 50 cm^3 of 0.1 mol dm^{-3} $K_3[Fe(CN)_6]$ under vigorous stirring. The resulting light-orange coloured precipitate was aged within the liqueur solution for 48 hr at room temperature. The precipitate was separated by filtration and washed several times with deionized water to remove any excess of the unreacted ions, until the electroconductivity of the solution was equal to around 4 μS. This was followed by drying of the powder at 298 K in air, until the weight remained constant.

3.1.6 Preparation of the M_3Fe^{III} / TiNT composite

The two step ion-exchange method of TiNT decoration with Cd_3Fe^{III} was adapted from [5]. This method was extended to synthesise novel composites of different transition metals of the hexacyanoferrate (III) in the form $M_3[Fe(CN)_6]_2$/TiNT (M_3Fe^{III}/TiNT), where M is one of the following transition metals: Fe, Ni, Co, Cu, Cd, Zn, or Mn [6]. In this method, the nanostructured composites of M_3Fe^{III}/TiNT were synthesised under atmospheric conditions (i.e. room temperature and 1 atm) according to the following steps:

1. The ion-exchange of TiNTs with M^{2+} ions

$$x\mathrm{M}^{2+}+(aq)+\mathrm{H_2Ti_3O_7}(s)\rightarrow \mathrm{M}_x\mathrm{H}_{2(1-x)}\mathrm{Ti_3O_7}(s)+2x\mathrm{H}^{+} \tag{3-1}$$

2. The reaction with $K_3[Fe(CN)_6]$

$$\mathrm{M}_x\mathrm{H}_{2(1-x)}\mathrm{Ti_3O_7}(s)+\frac{2x}{3}\mathrm{K_3[Fe(CN)_6]}(aq) \rightarrow \left(\mathrm{M_3[Fe(CN)_6]_2}\right)_{x/3}\mathrm{K}_{2x}\mathrm{H}_{2(1-x)}\mathrm{Ti_3O_7}(s) \tag{3-2}$$

In the first step, 1.5 g of H-TiNT was suspended in 150 cm^3 of 0.25 mol dm^{-3} MSO_4 aqueous solution under vigorous stirring for 36 hr at room temperature to achieve equilibrium. The sample obtained after ion exchange was filtered and thoroughly washed with deionized water. 150 cm^3 0.25 mol dm^{-3} $K_3[Fe(CN)_6]$ aqueous solution was then added drop-wise to the sample under vigorous stirring. After 24 hr the sample was filtered and washed with deionized water, and finally air dried under vacuum at room temperature. Figure 3.1 is a flow chart of the synthesis procedure.

In order to increase the amount of M_3Fe^{III} deposited on the TiNT surfaces, the M_3Fe^{III}/TiNT composite produced after the first cycle was subjected to another two cycles of the synthesis steps (ion-exchange with MSO_4 salts and reaction with $K_3[Fe(CN)_6]$) [5]. The resulting products were of different colours depending on the transition metal used. Photographic images of the as-synthesized TiNTs and M_3Fe^{III}/TiNT composite samples are shown in Figure 3.2.

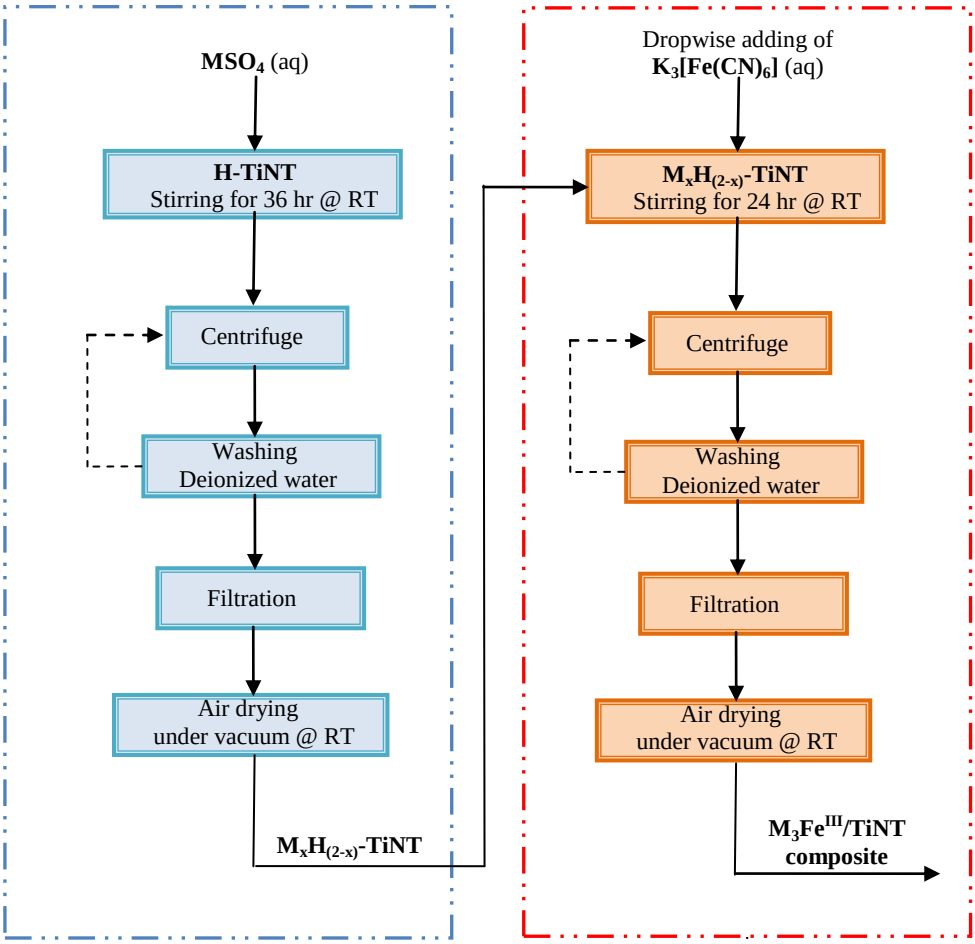

Figure 3.1: Flow chart of the preparation cycle of M_3Fe^{III}/TiNT composites at room temperature.

Figure 3.2: Photographic image of as synthesized TiNT, MxH(2-x)-TiNT and M_3Fe^{III}/TiNT composite samples (M= Fe (S1), Ni (S2), Co (S3), Cu (S4), Cd (S5), Zn (S6), and Mn (S7)).

3.2 Characterisation of the samples

The samples of as-prepared TiNT powders and all synthesised composites were characterised qualitatively and quantitatively based on surface analysis techniques and conventional characterisation methods. The characterisations techniques employed for each sample include Fourier transform infrared spectroscopy, scanning electron microscopy, transmission electron microscopy, X-ray diffraction, X-ray photoelectron spectroscopy, atomic force microscopy, thermo gravimetric analysis, chemical composition analysis, surface area and pore size distributions, and hydrogen adsorption capacity.

3.2.1 Fourier Transform Infrared (FTIR) spectroscopy

FTIR spectra were run in Nujol mulls in order to avoid the reduction of ferricyanide to ferrocyanide during composite milling and pressing with an alkali halide matrix [7]. FTIR spectra were performed using the KBr disc technique with a sample/KBr ratio of

1/10. All material spectra were recorded using a Perkin Elmer Spectrum One, in the frequency range 400-4000 cm^{-1}, with a spectral resolution of 8 cm^{-1}.

3.2.2 Scanning Electron Microscopy (SEM)

SEM images were obtained using a JEOL 6390 LV-SEM scanning electron microscope. The powders were coated with silver using a Sputter Coater Denton vacuum desk IV prior to examination. The coated samples were placed in a copper holder with the aid of carbon tape. The structural features of the raw and nanostructured titanate composites were observed at an accelerated voltage of 20 kV. Certain samples were characterised using a JEOL 6500 FEG-SEM scanning electron microscope.

3.2.3 Transmission Electron Microscopy (TEM)

TEM images were obtained using a JEOL 3010 transmission electron microscope operating at 300 kV; the powder sample was 'dry deposited' onto a copper grid covered with a perforated carbon film. The high-resolution images were obtained by using an A JEM-100S Transmission Electron Microscope operating at 80 kV. The composite powder was dispersed in methanol and a droplet of the slurry was transferred onto a carbon film-coated copper grid. The grid was left dry before the sample was mounted onto the microscope.

3.2.4 X-Ray Diffraction (XRD)

X-ray diffraction analysis was performed on a D-8 Advance Bruker AXS diffractometer using Cu Kα irradiation (λ =1.5406 Å), with a nickel filter in secondary beam and a scintillation detector. Fine powder samples were loaded and spread onto a glass sample holder and the XRD patterns were measured in a diffraction angle range (2θ) of 5^{o}–60^{o} using the step scan mode with a step size of 0.02°- 0.25° and a count time of 9-17 s per step.

3.2.5 X-Ray Photoelectron Spectroscopy (XPS)

The XPS measurements were carried out on K-Alpha Thermo Scientific model instrument. The instrument operates at 140 W employing a monochromated Al K*α* X-ray source with a photon energy (*hν*) = 1486.6 eV. The limits of detection are in an

interval of 0.1 to 0.5 % atomic with a space resolution of ≤ 6 mm. Binding energies and oxidation states were obtained from the XPS spectra using Casa XPS software.

3.2.6 Atomic Force Microscopy (AFM)

AFM measurements were performed using a Veeco Multimode V atomic force microscope, USA. The high resolution images were obtained with tapping mode in air and at room temperature, using a PZT scanner and a silicon nitride tip of 2 μm in length and nominal tip diameter of less than 10 nm. The image processing was carried out using Nanoscope Analysis Software version 1.40 from Bruker.

3.2.7 Thermo Gravimetric Analysis (TGA)

TGA profiles were determined using a high-resolution modulated thermo-gravimetric analyzer Q5000 IR (TA Instruments, Inc. USA). A certain mass of each sample, ranging between 5 and 10 mg, was placed in an open platinum pan and heated from ambient temperature to up to 800 °C. The process was carried out in a nitrogen atmosphere at a heating rate of 5 °C min^{-1} with a temperature perturbation amplitude of ± 2 °C and a period of 60 s. The results were analyzed using the TA Instruments Universal Analysis 2000 software.

3.2.8 Elemental analysis (EA)

Elemental analysis (EA) of the samples was performed using the following methods:

(i) Energy Dispersive Spectroscopy (EDX)
(ii) Organic Elemental Analysis (OEA)
(iii) Atomic Absorption Spectrophotometry (AAS)

EDX analyzes the characteristic X-rays emitted by the sample during SEM. Chemical composition analysis was performed using the EDX detector INCA X-sight 7582 (Oxford Instruments), housed at the JEOL 6390 LV-SEM Core. The mass and atomic composition was determined using the INCA Microanalysis Suite software. EDX is useful for determining the characteristics of small parts of the samples, but is ineffective at determining their bulk chemical characteristics. Therefore, EA of the organic content in the samples, i.e., hydrogen, carbon and nitrogen, was determined by using a PerkinElmer N2411362 Elemental Analyzer. In this analyzer, 10 to 20 mg of each

sample was placed in a tared large tin capsule and weighed precisely using a PerkinElmer AD6 Autobalance. All samples were dried at 353 K prior to analysis. Perkin-Elmer model 420 atomic absorption spectrophotometer (AAS) equipped with a HGA-76 graphite furnace was used in all samples for elemental analysis of titanium, potassium and the transition metals.

3.3 Adsorption Measurement Techniques

Adsorption measurements were performed to determine the adsorption characteristics of the studied materials, including adsorption isotherms, **s**urface areas**,** pore textural properties, kinetics and heats of adsorption. As mentioned previously (Chapter 2), the most widely used adsorption measurement techniques are the volumetric and gravimetric methods. In this thesis, adsorption measurements of the samples were carried out using the volumetric method.

3.3.1 Sample evacuation

Before any gas uptake measurements, the samples were degassed under vacuum conditions for a certain period of time to remove any moisture or other adsorbed gases from the surfaces of the solid. To ensure complete removal of moisture or other contaminants without any dissolution and/or damage to the pore structure of the samples appropriate temperatures and degassing times were selected according to the

Table 3.2: Evacuation conditions for the studied samples.

Sample	*T* (K)	Heating rate (K min^{-1})	Evacuation time (hr)
TiNT	408	5	7
$Cd_3[Fe(CN)_6]_2$	373	5	7
Cd_3Fe^{III}/TiNT @ pH= 2	423	5	6
Cd_3Fe^{III}/TiNT @ pH =4	423	5	6
Cd_3Fe^{III}/TiNT @ pH= 8	423	5	6
Cd_3Fe^{III}/TiNT @ pH=10	423	5	6
Fe_3Fe^{III}/TiNT	353	5	7
Ni_3Fe^{III}/TiNT	413	5	7
Co_3Fe^{III}/TiNT	393	5	7
Cu_3Fe^{III}/TiNT	373	5	7
Cd_3Fe^{III}/TiNT	408	5	7
Zn_3Fe^{III}/TiNT	373	5	7
Mn_3Fe^{III}/TiNT	403	5	7

results of thermal gravimetric analyses (shown in the relevant chapters). The determined preparation conditions for each sample are shown in Table 3.2. The adsorption and characterisation experiments were carefully monitored to avoid leakage and temperature fluctuations in order to generate reliable results.

3.3.2 Determination of the surface area and pore characteristics

The surface area and pore size distributions of the Cd_3Fe^{III}, TiNT and Cd_3Fe^{III}/TiNT samples were deduced from nitrogen adsorption isotherms at 77 K, obtained on a Micromeritics Gemini 2375 instrument, while the rest of the samples were characterised using a Micromeritics ASAP 2050 analyzer. The nitrogen adsorption-desorption isotherms measured at relative pressures up to $P/P_0 = 0.98$ were employed to determine the pore textural properties and BET surface areas. 100−150 mg of each sample was loaded into the sample holder of the instrument. Before the nitrogen adsorption measurements, the samples were degassed under vacuum conditions according to the preparation procedure mentioned above. The specific surface areas were calculated using the Brunauer-Emmett-Teller (BET) method [8] and the pore size distributions were determined using the Barret-Joyner-Halenda (BJH) method [8] with the built-in software (in the Micromeritics Gemini 2375 and Micromeritics ASAP 2050).

3.3.3 Hydrogen sorption measurements

Hydrogen sorption on the investigated materials was accomplished using high purity hydrogen (BOC, 99.99% purity) in all experiments. The hydrogen adsorption characteristics were measured volumetrically at low and high pressures using different adsorption apparatuses.

3.3.3.1 Hydrogen adsorption measurements in a Micromeritics ASAP 2050

The H_2 adsorption isotherms of CoIIICu were obtained using a Micromeritics ASAP 2020 analyzer. The H_2 excess adsorption isotherms for the NPs up to 10 bar were recorded using an ASAP 2050 analyzer (Micromeritics). In this type of material, the most reliable H_2 adsorption data, using an optimal measurement time, were obtained with a relatively small amount of sample (approximately 40 mg). Prior to the H_2 adsorption study, each sample was activated under primary vacuum conditions to

remove moisture and adsorbed gases from the surface of the solid. The activation conditions were: 24 hrs at 353 K for CoIIICu and 24 hrs at 333 K for the NP samples [1, 2]. Adsorption and desorption measurements were performed at liquid nitrogen temperatures (75 K or 77 K, depending on the local atmospheric pressure). The hydrogen storage capacities of the samples are reported in mg of hydrogen per g of the solid skeleton. The 'free space' of the sample holder was measured by adsorption of helium at a temperature equal to that used for hydrogen adsorption.

3.3.3.2 Hydrogen adsorption measurements in a PCTPro 2000

The isotherms of hydrogen adsorption on Cu_3(BTC), Cd_3Fe^{III}, TiNT and Cd_3Fe_2/TiNT samples were measured using a commercial Sievert-type apparatus, the PCTPro 2000 (Hy-Energy/Setaram), with a cryogenic attachment CryoPro-2009. In each experiment, 300─400mg of the sample powder was loaded into a sample holder equipped with a thermocouple (type K) located at the centre of the sample holder. Prior to the adsorption process:

- The $Cu_3(BTC)_2$ and bulk Cd_3Fe^{III} samples were activated by evacuation for 4 hr at 353 K, followed by 20 hrs at room temperature
- The TiNT and Cd_3Fe^{III}/TiNT samples were activated by evacuation for 7 hr at 408 K.

Gas adsorption isotherms were recorded in the range of pressures from 0 to 150 bar, for temperatures in the range 77 K to 298 K. Each data point in the pressure composition temperature (PCT) plot was measured by allowing the system to achieve adsorption/desorption equilibrium (the relative change of the hydrogen uptake was less than 10^{-4} wt. % min^{-1}). The thermal stability of the sample holder was 0.01 K for a temperature of 77 K and 0.05 K for temperatures between 80 K and 110 K. The 'free space' of the sample holder was measured by adsorption of helium at a temperature equal to that used for hydrogen adsorption. The hydrogen uptake was recorded in weight percentage units.

Hydrogen adsorption kinetic analyses of the Cd_3Fe^{III}, TiNT and Cd_3Fe^{III}/TiNT materials were also performed in the PCTPro 2000 apparatus. Evacuation of the samples was achieved using the procedure mentioned in the previous paragraph. Kinetic isotherms were measured:

- At 77 K with an initial hydrogen pressure of 135 bar for the Cd_3Fe^{III} and TiNT samples
- At 77 K, 88.5 K and 95 K with a pressure ranging from 50 to 135 bar for Cd_3Fe^{III}/TiNT composite.

The amount of hydrogen adsorbed was observed as a function of time and the final adsorption uptake was recorded as the adsorption equilibrium amount at the given hydrogen pressure.

3.3.3.3 Hydrogen adsorption measurements in a BELSORP-HP

Hydrogen adsorption isotherms for the Cd_3Fe^{III}/TiNT composites prepared at different pH solutions and for the M_3Fe^{III}/TiNT composite family were obtained using the automatic gas adsorption measurement apparatus BELSORP-HP (BEL Japan Inc.) provided with a BELCryo cryogenic system working in temperature range of 50-473 K by means of compressed liquid helium. The sample temperature was measured with a Pt sensor and the thermal stability of the sample holder was ±0.01 K for temperatures between 50 K and 323 K. Adsorption measurements were taken at two temperatures (77 and 87 K) for each of the samples of Cd_3Fe^{III}/TiNT prepared at different pH solutions and for the M_3Fe^{III}/TiNT composite family up to a hydrogen pressure of 1 bar. For each sample, 200–300 mg was loaded into a sample holder mounted inside the cryo unit. All samples were degassed at the conditions shown in Table 3.2. Leakage tests and 'dead volume' measurement were carried out automatically prior to the adsorption process. The measured hydrogen adsorption data were analysed with the BEL Master^{TM} software.

3.4 Mathematical modelling and software

Define $m_e^{(i)}$ to be the theoretical excess capacity at a pressure P_i and define $\tilde{m}_e^{(i)}$ to be the equilibrium capacity obtained from experiment at the same pressure P_i, where *i* ranges from 1 to *n* (the number of data points) [9]. The nonlinear least-squares method minimises the difference between the vector of model estimates:

$$\mathbf{m}_e = (m_e^{(1)}, m_e^{(2)}, \ldots, m_e^{(n)})$$

and the vector of experimental data values:

$$\hat{\mathbf{m}}_e = (\hat{m}_e^{(1)}, \hat{m}_e^{(2)}, \ldots, \hat{m}_e^{(n)})$$

in the following sense:

$$\min \left\| \mathbf{m}_e - \hat{\mathbf{m}}_e \right\|^2 = \min \left(\sum_{i=1}^{n} m_e^{(i)} - \tilde{m}_e^{(i)} \right)^2 \tag{3-3}$$

where $\|\cdot\|$ represents the Euclidean norm. The quantity $\left\| \mathbf{m}_e - \hat{\mathbf{m}}_e \right\|^2$ in (3-3) contains the parameter values that are to be determined, say k_j, where $j = 1, \ldots l$ (l is the number of parameters). It is viewed as a function $\phi(\mathbf{k}) = \left\| \mathbf{m}_e - \hat{\mathbf{m}}_e \right\|^2$ of the vector of parameter values $\mathbf{k} = (k_1, \ldots k_l)$, and the problem is posed as one of finding the value of $\mathbf{k}$ that minimizes the 'objective' function $\phi(\mathbf{k})$. This value of $\mathbf{k}$ is denoted $\arg\min_{\mathbf{k}} \phi(\mathbf{k})$ and yields the parameter values sought.

There are several methods for minimizing nonlinear objective functions, most of which are gradient based (meaning that information related to the gradient is utilised). Typically, from an initial guess for $\mathbf{k}$ (say $\mathbf{k}_0$), the gradient:

$$\nabla_{\mathbf{k}} \phi = (\partial \phi / \partial k_1, \ldots, \partial \phi / \partial k_l)$$

and/or other information related to the function $\phi(\mathbf{k})$ is approximated using a Taylor series expansion of $\phi(\mathbf{k})$. The information is used to determine a direction in which to proceed (towards a minimum). The size of the step taken in this direction ($\Delta\mathbf{k}$) is chosen such that the function is minimized in that direction only (a 'line search'). The process is repeated iteratively with the new end point (in step 1 this is $\mathbf{k}_1 = \mathbf{k}_0 + \Delta\mathbf{k}$) as the new starting point in each iteration, until a pre-set convergence criterion is met. The Origin 8.0 software used in this thesis employs the gradient-based Levenberg-Marquardt algorithm. The results were verified using an interior-point method implemented in Matlab.

One measurement of the quality of the fit is the *coefficient of determination* (defined below), although for nonlinear least squares it has no direct relationship to the correlation:

$$R^2 = \frac{\sum_{i=1}^{n}\left(m_e^{(i)} - \bar{m}_e\right)^2}{\sum_{i=1}^{n}\left(m_e^{(i)} - \bar{m}_e\right)^2 + \sum_{i=1}^{n}\left(m_e^{(i)} - \tilde{m}_e^{(i)}\right)^2} \tag{3-4}$$

where $\bar{m}_e$ is the average value of $\tilde{m}_e^{(i)}$, i.e., of the experimental excess measurements. Deviations of R^2 from unity (an 'ideal' match) represent differences between the final fitted form and the experimental data.

References

[1] Reguera L., Krap C.P., Balmaseda J., Reguera E., J. Phys. Chem. C 112 (2008) 15893−15899.

[2] Reguera L., Roque J., Hernandez J., Reguera E., Int. J. Hydrogen Energy 32 (2010) 12864−12869.

[3] Liu J., Culp J.T., Natesakhawat S., Bockrath B.C., Zande B., Sankar S.G., Garberoglio G., Johnson J.K., J. Phys. Chem. C 111 (2007) 9305–9313.

[4] Bavykin D.V., Kulak A.N., Walsh F.C., Crystal Growth & Design 10 (2010) 4421–4427.

[5] Ivekovic D., Gajovic A., Ceh M., Pihlar B., Electroanalysis 22 (2010) 2202–2210.

[6] Al-Hajjaj A.A., Zamora B., Bavykin D.V., Shah A.A., Walsh F.C., Reguera E., Int. J. Hydrogen Energy 37 (2012) 318–326.

[7] Fernández-Bertrán J., Reguera E., Solid State Ionics 93 (1997) 139–146.

[8] Lowell S., Shields J.E., Thomas M.A., Thommes M., Characterisation of Porous Solid and Powders: Surface Area, Pore Size and Density, Kluwer, 2004, Academic Publishers.

[9] Al-Hajjaj A.A., Zamora B., Shah A.A., Reguera E., Bavykin D.V., Walsh F.C., Int. J. Hydrogen Energy 36 (2011) 14464–14476.

Chapter 4: The application of standard isotherms to hydrogen sorption in microporous materials

4.1 Introduction

The amount of a gas adsorbed changes with pressure and can be measured in a number of ways. Equilibrium relationships that correlate the amount of gas adsorbed on a solid surface with the applied gas pressure at a constant temperature are known as *adsorption isotherms*. In this chapter, the main features of adsorption isotherms are summarized and a detailed mathematical framework for simulating standard isotherms for microporous materials is developed. The validity of standard isotherm models is also assessed by application of the modelling framework to data from several classes of microporous materials.

4.2 Types of isotherms

Different type of adsorption isotherms can be obtained for the adsorption of gases (adsorbate) on solids (adsorbent) depending on the nature of the adsorbate, structure of the adsorbent and the intermolecular interactions between the adsorbent and adsorbate. The first systematic classification of physical adsorption isotherms was introduced by Brunauer and co-workers [1,2]. They categorised isotherms into five characteristic types, commonly referred to as the BDDT classification. This set of BDDT isotherm types was later expanded by Sing [3] to include an isotherm characterized by steps. The BDDT and Sing classification has become the basis of the modern International Union of Pure and Applied Chemistry (IUPAC) standard classification of adsorption isotherms [4]. The six different types of isotherms are depicted in Figure 4.1. Several isotherms observed in practice do not, however, fit into the IUPAC standard classification. Some of these isotherms may be described as ‘mixed’ adsorption isotherms. For example, gas adsorption for a porous sample with large surface area may generate a compound

isotherm comprising two or more of isotherms I to IV dominating in different, non-overlapping regions of pressure [5].

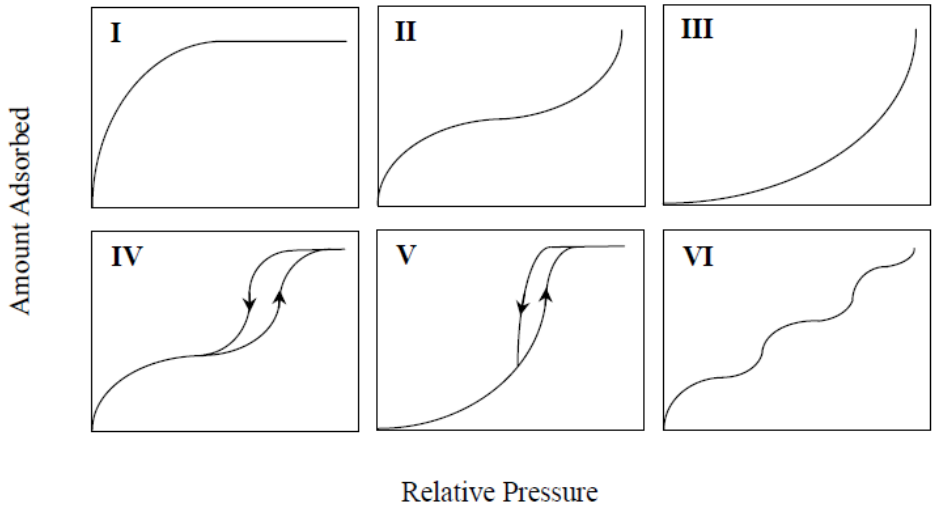

Figure: 4.1: IUPAC classification of adsorption isotherms [4].

1) The type I isotherm is common to microporous materials (pore size <2 nm) and is characterised by a steep increase in the hydrogen uptake at low pressures (corresponding to progressive filling of the micropores), followed by a plateau in the adsorbed mass at higher pressures as monolayer coverage is approached. The steep rise at low pressures is proportional to the heat of adsorption; the stronger the interaction between gas and adsorbent, the steeper the increase in the mass of adsorbed gas with increasing pressure.

2) The type II isotherm represents the typical form for unrestricted monolayer-multilayer adsorption obtained with a non-porous or macroporous (pore size >50 nm) adsorbent. It has a concave shape at low relative pressure, and then a linear shape for a small pressure range after completion of the monolayer coverage. The isotherm becomes convex in the region where multilayer adsorption takes place.

3) The type III isotherm is uncommon and is exhibited by nonporous or highly macroporous adsorbents. It is convex in shape over the entire range of the relative pressure, P/P_0, indicating that adsorbate-adsorbent interactions are weak and that adsorbate-adsorbate interactions play an important role.

4) Isotherm IV is common to mesoporous (2 nm <pore size <50 nm) adsorbents. The initial part of the type IV isotherm is assigned to monolayer-multilayer adsorption since it resembles the corresponding part of the type II isotherm. The uptake at high pressure is limited, resulting in a plateau of the isotherm, which indicates complete pore filling.

5) In contrast to the type IV isotherm, the initial part of the type V isotherm is similar to that of the type III isotherm, due to weak adsorbent-adsorbate interactions. This isotherm is highly uncommon and is exhibited by certain mesoporous solids. Moreover, type IV and V isotherms are characterized by a hysteresis loop of the form shown in Figure 4.1, i.e. the adsorption and desorption isotherms do not coincide over the entire range of pressure. The hysteresis loop is associated with the secondary process of capillary condensation, which results in the complete filling of the mesopores at P/P_0 <1 [6].

6) The type VI isotherm may be attributed to the formation of multiple layers of the adsorbate in nonporous solids with a very uniform surface [3], particularly by spherically-symmetrical, non-polar adsorbates. The height of each step can represent the monolayer capacity for each layer. This isotherm is rarely encountered and its importance comes primarily from theoretical point of view.

In most cases, the isotherm is approximately linear at sufficiently low surface coverages, a region that is termed the Henry's Law region. More detailed discussions on the shape and features of desorption isotherms can be found in many texts [3,4,7-9].

4.3 Modelling of standard isotherms to hydrogen sorption in microporous materials

Modelling of adsorption isotherm data is important for predicting and comparing adsorption performance. Due to the small pore dimensions of microporous materials, adsorption of gaseous substances in such materials is limited to only one or a few molecular layers [7]. Many isotherm models are available for modelling monolayer adsorption data: Freundlich, Langmuir, Freundlich−Langmuir, Dubinin−Astakhov, Toth, and UNILAN are the most commonly used [10,11]. Despite the widespread use of

these isotherms, there have been few systematic appraisals of their ability to capture the adsorption/desorption behaviour in specific classes of materials.

A model for hydrogen storage in porous materials was developed by Zhou and co-workers [12-15]. The authors derived a two-parameter relation for the absolute (total) hydrogen in the solid [12] and used low-pressure (up to approximately 0.05 atm) excess data to fit the two model parameters. The same two-parameter expression was then reused to estimate the adsorbed volume by fitting it to the entire set of data (up 10 atm pressure), a procedure that required a prior fit of the bulk gas density as a polynomial in pressure [15]. After subsequently fitting the adsorbed-phase volume to a polynomial in pressure and developing a second three-parameter expression for the absolute mass, which did not obey the Henry's law limit at low pressure and was in fact an expression for the adsorbed-phase mass, a further nonlinear regression analysis was performed using the entire data set to determine the three new parameters [15].

In this section, a complete modelling framework that explicitly incorporates the two phases of hydrogen (adsorbed and compressed) is developed. Analytical expressions for the adsorbed phase, compressed (gas) phase, absolute (total) and excess hydrogen masses in the porous solid are derived (under equilibrium conditions), within a framework that allows them be used in conjunction with *any* model isotherm. These relations are valid in the entire range of pressures and the model parameters are determined by a single nonlinear regression analysis comparing the predicted excess mass to experimental excess data, thereby ensuring consistency and far greater accuracy. The model predictions using several well-known equilibrium isotherm relations are compared to experimental data for three classes of microporous materials, with results that are consistent with available data in the literature.

The data used for the regression analysis and appraisal of the model corresponds to:

(1) The Prussian blue analogue $Cu_3[Co(CN)_6]_2$ (CoIIICu).
(2) The two NPs $M_3[Fe(CN)_5NO]$ with M=Ni and Co.
(3) The metal-organic framework $Cu_3(BTC)_2$.

The physical and structural properties of all materials considered are listed in Table 4.1. The densities and pore volumes of CoIIICu and the NPs were calculated from XRD and TGA analyses. Property values for $Cu_3(BTC)_2$ were taken from Liu *et al.* [16].

Table 4.1: Physical properties and parameters of studied materials.

Material	Cell parameter (Å)	Cell volume (cm^3)	ρ_s (g cm^{-3})	Pore volume (cm^3 g_{solid}^{-1})	Porosity ε
NpCo	10.26	1.08×10^{-21}	1.267	2.49	0.47
NpNi	10.18	1.06×10^{-21}	1.296	1.25	0.41
CoIIICu	10.06	1.02×10^{-21}	1.012	4.43	0.24
$Cu_3(BTC)_2$ *	—	—	0.880	0.61	0.30

** Literature value [16]*

4.4 Mathematical model

The total (absolute) mass of hydrogen stored in a volume of a porous material is the sum of the mass adsorbed at the surface of the solid component $M_{H_2(a)}$ (adsorbed phase) and the mass contained in the remaining pore volume (compressed or bulk phase) $M_{H_2(g)}$ [13, 14]:

$$M = M_{H_2(g)} + M_{H_2(a)} \tag{4-1}$$

Adsorption takes place in a volume V_a (on the gas side) in a region above the solid surface, termed the adsorption or interfacial layer (see Figure 4.2). As the bulk gas phase is approached from the solid surface, the hydrogen density decreases continuously towards the bulk gas value. Throughout the bulk phase, the gas density ρ_g remains constant. The hydrogen mass in the bulk gas phase is given by:

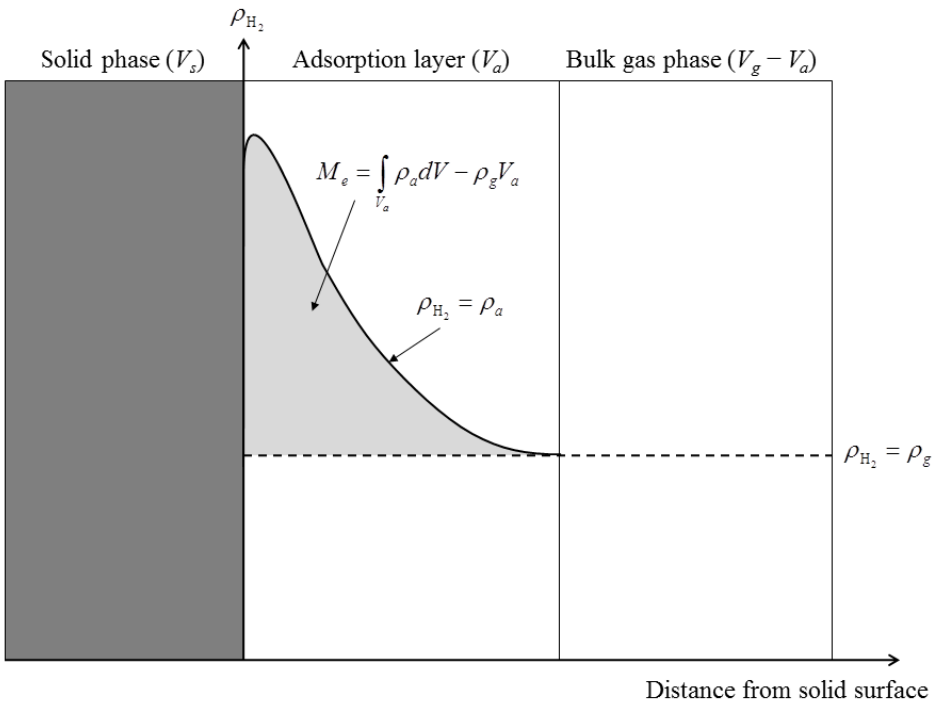

Figure 4.2: A schematic of the adsorption of H_2 in a porous material. The total pore volume is V_g and the adsorption volume is V_a. The bulk (compressed) gas resides in a volume $V_g - V_a$ at a pressure ρ_g. The condensed gas is located in the adsorption layer at a density ρ_a, which decays to zero at the solid surface and approaches ρ_g as the bulk region is approached.

$$M_{H_2(g)} = \rho_g (V_g - V_a) \tag{4-2}$$

where V_g is the total pore volume in the porous solid. The total specific surface area (per unit mass of the solid) for adsorption in a porous solid can be estimated from the relation:

$$S = \frac{q_m A_{H_2} N_A}{m_{H_2}} \quad ` \tag{4-3}$$

where q_m is the maximum adsorbed mass at monolayer coverage per unit mass of the solid skeleton, N_A is Avogadro's number, A_{H_2} is the occupied surface area of one

hydrogen molecule and m_{H_2} is the molecular mass of hydrogen. The surface area covered by (adsorbed) hydrogen is given by the product of the total surface area and the surface fractional coverage or occupancy ratio θ, which can be defined as the ratio of the condensed mass q_{H_2} to the maximum condensed mass at monolayer coverage: $\theta = q_{H_2} / q_m$. Note that q_{H_2} is the mass of hydrogen adsorbed *per unit mass of the solid skeleton*, i.e., $q_{H_2} = M_{H_2(a)} / M_s$. Using these definitions and equation (4-3) to express q_m in terms of the surface area, the adsorbed mass can be written as follows:

$$M_{H_2(a)} = \frac{m_{H_2} \rho_s V_b (1-\varepsilon)}{A_{H_2} N_A} S\theta \tag{4-4}$$

in which the relationships $\varepsilon = V_g / V_b$ (sample porosity), $(1-\varepsilon) = V_s / V_b$ (solid skeleton volume fraction) and $\rho_s = M_s / V_s$ (solid skeleton density) were used; V_g is the total gas volume, V_s is the solid skeleton volume and V_b is the total volume of the sample.

Substituting equations (4-2) and (4-3) into equation (4-1) and using the definition of porosity yields a new expression for the absolute mass of hydrogen in the system:

$$M = \rho_g \left(\varepsilon V_b - V_a \right) + \frac{m_{H_2} \rho_s (1-\varepsilon) V_b}{A_{H_2} N_A} S\theta \tag{4-5}$$

The hydrogen gas density is given by the equation of state $\rho_g = g(P,T)$, in which P is the pressure associated with the compressed phase and T is the system temperature. For an ideal gas, $g(P,T) = m_{H_2} P / RT$, where R is the molar gas constant. In what follows, the ideal gas law will be used for the simplicity of presentation; it is straightforward, however, to replace this law with an arbitrary equation of state throughout, leaving the analysis otherwise unaltered. The process of adsorption is usually studied through a relation known as the adsorption isotherm, which describes the coverage θ as a function of the applied gas pressure P at constant temperature:

$$\theta = f(P) \tag{4-6}$$

The absolute mass is now given by equation (4-5) combined with the gas law and equation (4-6):

$$M(P) = \underbrace{\frac{m_{H_2}\left(\varepsilon V_b - V_a\right)P}{RT}}_{M_{H_2(g)}} + \underbrace{\frac{m_{H_2}\rho_b V_b S}{A_{H_2} N_A} f(P)}_{M_{H_2(a)}} \tag{4-7}$$

where the definition $\rho_b = \rho_s(1-\varepsilon)$ of the bulk density of the material has been used. This expression demonstrates how the absolute mass can be predicted using only the applied pressure P as the dependent variable. The two components of this mass are given explicitly in terms of quantities that are measurable, with the exception of the interfacial layer volume V_a. Calculation of V_a is key to fully describing the adsorption process and the procedure for estimating this volume is discussed later in this section.

The so-called (Gibbs surface) *excess* M_e is defined as the total mass of hydrogen in the system above the mass that would reside in the pore volume at the same pressure and temperature. Equivalently, it is given by the difference between the mass in the interfacial layer and the mass that would reside in the interfacial layer if the gas had a density ρ_g (the bulk value):

$$M_e = M - \rho_g V_g = M_{H_2(a)} - \rho_g V_a \tag{4-8}$$

Using equations (4-7) and (4-8), the excess mass can be estimated as follows:

$$M_e = m_{H_2}\left(\frac{\rho_b V_b S}{A_{H_2} N_A} f(P) - \frac{P V_a}{RT}\right) \tag{4-9}$$

In the vast majority of cases, only the excess mass is directly measurable, so that an expression for this quantity is needed to perform a regression analysis. For practical purposes, however, the absolute hydrogen mass in the system (M) is the more useful measure. The only quantity in equation (4-9) that cannot be measured independently (e.g. using nitrogen or argon) is V_a. It is well known that this volume increases with

pressure. To determine the functional form of V_a the definition $\theta = V_a / V_m$ of the surface coverage can be used, in which V_m is the volume occupied by a monolayer. This implies a relationship of the form:

$$V_a = V_m \theta = V_m f(P) \tag{4-10}$$

so that equation (4-9) becomes:

$$M_e = m_{\mathrm{H}_2} f(P) \left(\frac{\rho_b V_b S}{A_{\mathrm{H}_2} N_A} - \frac{P V_m}{RT} \right) \tag{4-11}$$

Equation (4-11) provides the basis for a strategy to simultaneously determine several quantities of interest (if they are unknown): the parameters in the isotherm model $f(P)$ the surface area S (or, equivalently, q_m) and the volume associated with a monolayer V_m (and, therefore, V_a from equation (4-10)). A nonlinear regression analysis using experimental excess isotherms in the entire range of pressure can be applied once to equation (4-11) in order to compute the parameters. Once determined, these parameters can be substituted into equation (4-11) to make predictions under different operating conditions, provided they are well characterised at different pressures and temperatures.

The excess capacity of a material to store hydrogen can be given in two main forms, gravimetric m_e and volumetric $\tilde{m}_e$. Depending on the target application, one of these capacity measures could take on greater importance. Since they are used in the discussion to follow, explicit expressions are provided for each. The gravimetric capacity is defined as the mass of hydrogen (excess or absolute) per unit mass of the solid skeleton. For the excess capacity, for example, the expression is given by:

$$m_e = \frac{M_e}{\rho_b V_b} = \left(\frac{S}{A_{\mathrm{H}_2} N_A} - \frac{P V_m}{\rho_b V_b RT} \right) m_{\mathrm{H}_2} f(P) \tag{4-12}$$

In order to convert this measure to the volumetric measure (mass per unit volume of the bulk porous material), it is multiplied by the bulk density of the porous solid, i.e.,

$\tilde{m}_e = \rho_b m_e$. Note that these measures are quite specific and require careful interpretation; highest gravimetric capacity does not necessarily imply highest volumetric capacity.

One of the main challenges in quantifying adsorption is to convert the conventional (gravimetric or volumetric) measurement of the excess hydrogen capacity to the absolute capacity. According to equation (4-8), $M/(\rho_b V_b) = M_e/(\rho_b V_b) + \rho_g V_g/(\rho_b V_b)$, so that the absolute capacity (per unit mass of the solid skeleton) is given by:

$$m_t = m_e + \left(\frac{\varepsilon}{(1-\varepsilon)\rho_s}\right)\frac{m_{H_2} P}{RT} = m_e + V_{pore}\frac{m_{H_2} P}{RT} \tag{4-13}$$

in which the ideal gas law has been used and m_e represents the experimental or analytical excess capacity. The second equivalent form on the right-hand side uses the *specific pore volume* V_{pore}, which is defined as the pore volume per unit mass of the solid skeleton and can be estimated independently, e.g., through nitrogen adsorption experiments.

Hydrogen adsorption/desorption kinetics are as important as the equilibrium adsorption behaviour since the time required for re-fuelling and discharging in dynamic applications, such as automotive fuel cell stacks, is restricted [17]. Furthermore, the kinetic data is required for selecting optimum operating conditions for the design and modelling of full-scale processes [18]. In cases where adsorption occurs at equilibrium or quasi equilibrium, the model developed above could be used to determine the time taken to reach a required pressure P with an initial pressure of P_0 if the flow rate of hydrogen into the system or from the system $(\dot{m} = dM/dt)$ is constant. In such a system, the mass at time t is given by $M = M_0 + \dot{m}t$, where M_0 is the initial mass in the system, which is given by equation (4-7) with $P = P_0$; noting also that $V_a(t=0) = V_m f(P_0)$. The time taken to reach a final pressure P is then given by:

$$t = \frac{\varepsilon V_b m_{H_2}}{\dot{m}RT}(P - P_0) - \frac{V_m m_{H_2}}{\dot{m}RT}\left(Pf(P) - P_0 f(P_0)\right) + \frac{m_{H_2}\rho_b V_b S}{\dot{m}A_{H_2} N_A}\left(f(P) - f(P_0)\right) \tag{4-14}$$

which can be applied to any isotherm $\theta = f(P)$. For applications requiring the constant release of hydrogen from a storage vessel, setting $P = 0$ in this expression gives an upper bound t_f on the time to full release (noting that in this case $\dot{m} < 0$) since it assumes that equilibrium is maintained at all times:

$$t_f = -\frac{m_{H_2} P_0}{\dot{m} R T}\left(\varepsilon V_b - V_m f(P_0)\right) - \frac{m_{H_2} \rho_b V_b S}{\dot{m} A_{H_2} N_A} f(P_0) \tag{4-15}$$

Note that $f(0) = 0$ was used in the derivation of equation (4-15).

4.4.1 Standard isotherm models

Among the most widely used isotherms $\theta = f(P)$ are the Freundlich, Langmuir, Freundlich-Langmuir (Sips), Dubinin-Astakhov, Toth, and UNILAN models. A brief description of these isotherms will be given next. Further details can be found in [11]. The Freundlich isotherm is derived from the assumption that the adsorption sites are distributed exponentially with respect to the heat of adsorption. The general form, considering q_m to be equal to unity, is given by the following equation:

$$\theta = KP^{1/n} \tag{4-16}$$

where K and n are empirical constants that are characteristic of the given adsorbent-adsorbate system at a particular temperature.

The semi-empirical Langmuir isotherm is derived from a proposed kinetic mechanism and the assumption of monolayer adsorption on the active sites of the adsorbent surface [18]. It can be expressed as follows:

$$\theta = \frac{K_L P}{1 + K_L P} \tag{4-17}$$

where K_L is the temperature-dependent Langmuir (or affinity) constant.

One of the disadvantages of the Freundlich isotherm is that it is not generally valid at low and high pressures. In an attempt to circumvent this problem, Sips extended the

Freundlich isotherm to include a finite limit at sufficiently high pressures [11], resulting in the Langmuir-Freundlich (L-F) isotherm:

$$\theta = \frac{K_{LF} P^{1/n_{LF}}}{1 + K_{LF} P^{1/n_{LF}}} \tag{4-18}$$

where K_{LF} is the temperature-dependent L−F affinity constant and n_{LF} is a parameter associated with the degree of heterogeneity. At low pressures, however, the L−F isotherm inherits the poor performance of the Freundlich isotherm.

The Dubinin-Astakhov (D−A) isotherm equation (given below) was developed originally using the theory of volume filling of micropores and the Polanyi concept of desorption potential [19, 20].

$$\theta = \exp\left\{ -\left[K_{DA} \ln\left(\frac{P_s}{P} \right) \right]^{n_{DA}} \right\} \tag{4-19}$$

where n_{DA} is the heterogeneity parameter, K_{DA} is the adsorbent-adsorbate affinity constant and P_s is a pseudo saturation vapour pressure. The pseudo saturation vapour pressure of hydrogen is estimated using the Dubinin approach [21]:

$$P_s = \left(\frac{T}{T_c} \right)^2 P_c \tag{4-20}$$

where P_c and T_c are the critical pressure and temperature of hydrogen, respectively.

Toth proposed an alternative empirical model based on monolayer adsorption (given below), which can describe many systems with sub-monolayer coverage by virtue of its ability to capture the behaviour at both low and high pressures [22, 23]:

$$\theta = \frac{P}{\left(b + P^{n_T} \right)^{1/n_T}} \tag{4-21}$$

where n_T is the degree of system heterogeneity and b is an affinity parameter. Note that for $n_T = 1$ this isotherm reduces to the Langmuir isotherm after dividing both the numerator and denominator by b and identifying the resulting constant as the Langmuir constant.

The UNILAN isotherm is another empirical relation derived under the assumption of a uniform distribution of energy on the solid surface. It is a modified form of the Langmuir isotherm, from which the name UNILAN originates: 'uniform distribution' and 'Langmuir local isotherm' [11]. It takes the following form:

$$\theta = \frac{1}{2s}\ln\left(\frac{c + P\exp(s)}{c + P\exp(-s)}\right) \tag{4-22}$$

where (c) is an adjustable parameter and (s) is a dimensionless parameter that characterises the heterogeneity of the surface, as well as the adsorption energy distribution [18], according to the following expression:

$$s = \frac{E_{\max} - E_{\min}}{2RT} \tag{4-23}$$

in which $E_{\max}$ and $E_{\min}$ are the maximum and minimum energies of the distribution, respectively. The UNILAN equation reduces to the classical Langmuir equation in the limit $s \to 0$ (the range of energy distribution approaches zero), taking into account that $\ln(1+x) \sim x$ for $x \to 0$. The adjustable parameters *b* and *c* in the last two isotherms are, in principle, reciprocals of the affinity constant.

4.4.2 Proposed models

Equations (4-17)−(4-19), (4-21) and (4-22) were used in combination with equation (4-12) to simulate excess hydrogen adsorption isotherms at liquid-nitrogen temperatures (77 K or 75 K depending on the local atmospheric pressure) for the materials listed in Section 2. The form of equation (4-12) for each of the isotherms is shown explicitly in Table 4.2.

Table 4.2: Proposed model for excess adsorption m_e (g g^{-1}) using different standard isotherms.

Isotherm	**Fractional surface coverage θ**	**Formula for excess capacity m_e (equation (10))**
Langmuir	$\frac{K_L P}{1+K_L P}$	$\left(\frac{S}{A_{\mathrm{H_2}} N_A}-\frac{PV_m}{\rho_b V_b RT}\right)\left(\frac{m_{\mathrm{H_2}} K_L P}{1+K_L P}\right)$
Langmuir–Freundlich	$\frac{K_{LF} P^{1/n_{LF}}}{1+K_{LF} P^{1/n_{LF}}}$	$\left(\frac{S}{A_{\mathrm{H_2}} N_A}-\frac{PV_m}{\rho_b V_b RT}\right)\left(\frac{m_{\mathrm{H_2}} K_{LF} P^{1/n_{LF}}}{1+K_{LF} P^{1/n_{LF}}}\right)$
Dubinin–Astakhov	$\exp\left\{-\left[K_{DA}\ln\left(\frac{P_s}{P}\right)\right]^{n_{DA}}\right\}$	$\left(\frac{m_{\mathrm{H_2}} S}{A_{\mathrm{H_2}} N_A}-\frac{m_{\mathrm{H_2}} PV_m}{\rho_b V_b RT}\right)\exp\left\{-\left[K_{DA}\ln\left(\frac{P_s}{P}\right)\right]^{n_{DA}}\right\}$
Toth	$\frac{P}{\left(b+P^{n_T}\right)^{1/n_T}}$	$\left(\frac{S}{A_{\mathrm{H_2}} N_A}-\frac{PV_m}{\rho_b V_b RT}\right)\frac{m_{\mathrm{H_2}} P}{\left(b+P^{n_T}\right)^{1/n_T}}$
UNILAN	$\frac{1}{2s}\ln\left(\frac{c+P\exp(s)}{c+P\exp(-s)}\right)$	$\left(\frac{S}{A_{\mathrm{H_2}} N_A}-\frac{PV_m}{\rho_b V_b RT}\right)\frac{m_{\mathrm{H_2}}}{2s}\ln\left(\frac{c+P\exp(s)}{c+P\exp(-s)}\right)$

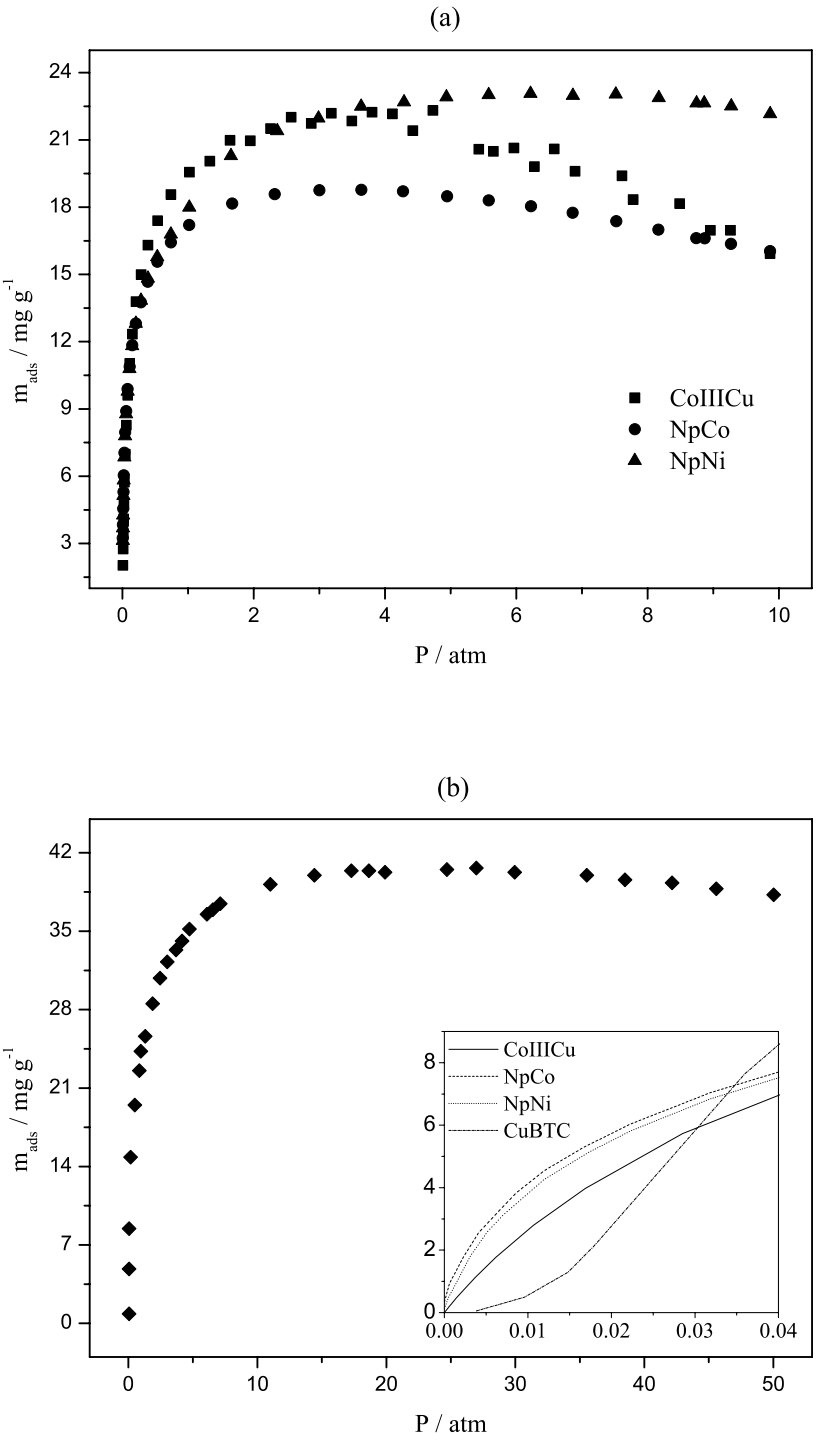

Figure 4.3: (a) Excess H_2 adsorption isotherms (experimental) for NpNi, NpCo and CoIIICu up to 9.86 atm at 75 K. (b) The excess isotherm for CuBTC up to 52 atm at 77 K. The inset in Figure 4.1(b) shows the low-pressure behaviour for all four materials.

4.5 Results and discussion

4.5.1 Experimental results

To aid the modelling analysis, the equilibrium isotherms for the four materials are first discussed briefly. The excess hydrogen adsorption isotherms for NpCo, NpNi and CoIIICu at 75 K and up to 9.86 atm pressure are presented in Figure 4.3(a), while the corresponding adsorption isotherm for $Cu_3(BTC)_2$ up to 52 atm pressure is shown in Figure 4.3(b). Figure 4.3 is the first direct comparison of the four materials. According to this figure, $Cu_3(BTC)_2$ exhibits the highest gravimetric excess capacity (41 mg g^{-1}) at 9.86 atm, while CoIIICu and NpCo exhibit the lowest (both around 16 mg g^{-1}). The absolute (total) capacity can be obtained from the excess value using equation (4-13) and will be discussed later in this section. The excess capacities based on the data used in Figure 4.3 are similar to those measured previously, namely ca. 2 wt. % at 1 bar for CoIIICu [24] and ca. 4 wt. % at 25 bar for $Cu_3(BTC)_2$ [25]. Comparisons for the NP values are not possible due to lack of available data.

The adsorption isotherms of all materials studied exhibit a type I adsorption isotherm up to saturation [7], which is typical of physisorption in microporous materials. In this isotherm, the plateau in the adsorbed mass is reached when monolayer coverage of the adsorbent surface is realised. In contrast, the excess mass, which is the quantity shown in Figure 4.3, decreases beyond a maximum value that is reached when the adsorbate surface is saturated. This is due to the definition of excess mass in equation (4-8) as the difference (under isothermal conditions) between the actual adsorbed-phase mass in the adsorption layer ($M_{\mathrm{H}_2(a)}$) and the mass that would exist in the adsorption layer at the pressure of the bulk gas ($m_{\mathrm{H}_2} PV_a/(RT)$ if the ideal gas law is used). While the adsorbed phase mass reaches a finite maximum at saturation, $m_{\mathrm{H}_2} PV_a/(RT)$ continues to increase as the pressure is increased.

4.5.2 Estimated parameter values

Equations (4-12) and (4-13) can be used to simulate the excess and absolute uptake values and to estimate the isotherm parameters (associated with Langmuir, L−F, D−A, Toth or UNILAN), the surface area S (if it is unknown) and the maximum adsorption

volume V_m using nonlinear regression. The analysis was performed using the software Origin 8.0, which implements the nonlinear least-squares method (details are given in section 3.4). The values of the coefficient of determination for each model are given in Table 4.3. It must be pointed out that the quality of the fit to the experimental data (measured, e.g., through R^2) should be interpreted with caution. Even with values of R^2 close to unity, there is no guarantee that the predictions of the underlying parameter values are accurate. The surface area, for example, will depend on the functional form of the isotherm, i.e., on *prior* information incorporated in the model. The predicted values of the parameters should, therefore, be examined and compared to independent measurements or estimates in order to fully judge the accuracy of the model.

Table 4.3: Coefficients of determination (R^2) related to the fitting of Equation (4-12), used with the standard isotherms, to the experimental data, at liquid nitrogen temperatures.

Sample	T / K	Langmuir	L-F	D-A	Toth	UNILAN
CoIIICu	75	0.97696	0.99405	0.99531	0.99567	0.99700
$Cu_3(BTC)_2$	77	0.97312	0.98561	0.98643	0.98673	0.98748
NpCo	75	0.96282	0.99936	0.99968	0.99987	0.99991
NpNi	75	0.94709	0.99811	0.9985	0.99805	0.99805

At the liquid nitrogen temperature, the value of the estimated affinity constant K_L (shown in Table 4.4) increased in the following order: $Cu_3(BTC)_2$<CoIIICu<NpNi <NpCo. Higher values of K_L indicate a stronger degree of interaction between the gas and the solid surface. The surface area estimates based on the Langmuir model (Table 4.4) are considerably smaller than the typical experimental values available in the literature, as well as the values predicted by the other isotherms, with the exception of the value for $Cu_3(BTC)_2$. The reason for this is the assumption of an energetically homogeneous surface in the derivation of the Langmuir model; in the case of a heterogeneous surface, the actual total surface required for the same mass of adsorbed hydrogen would, therefore, be higher than that predicted by the Langmuir equation. $Cu_3(BTC)_2$, however, possesses the lowest degree of heterogeneity of the four materials (see Table 4.4 and the discussion below), yielding a more accurate estimate when the Langmuir isotherm is used.

Using the L−F equation, the values of K_{LF} (the affinity constant) at the liquid nitrogen temperature can be arranged as follows: $Cu_3(BTC)_2$<NpNi<CoIIICu<NpCo, as shown in Table 4.4, which agrees with the Langmuir model, except in the case of NpNi and CoIIICu. In contrast to the Langmuir model, the L−F model does not give the correct Henry's law limit. The behaviour at high pressures, however, is more accurately captured in L−F through the parameter n_{LF}, which characterises the heterogeneity of the surface (typically an integer between 1 and 5 [26]). This heterogeneity could stem from the solid, the adsorbate or a combination of both and depends on the dimensions of the micropores, the pore size distribution and the nature of active adsorption centres. Since neither the Langmuir nor the L−F equations is valid through the entire range of pressure, it is unsurprising that the results using these two models do not entirely agree.

The degree of heterogeneity ($1/n_{LF}$) at the liquid nitrogen temperature, also shown in Table 4.4, was ordered as follows: $Cu_3(BTC)_2$<CoIIICu<NpCo<NpNi. The value obtained for CoIIICu is in excellent agreement with the value of 1.65 obtained in [27], also using an L−F model fitted to experimental results. The values for NpNi and NpCo are similar to those obtained in [28] using L-F, i.e., 2.4 and 2.2, respectively; the discrepancies are likely to result in part from the fact that the regression analysis in [28] was performed with data obtained up to only 1 atm pressure, well before the onset of saturation. Table 4.5 shows the influence of variations in pressure range on the calculation of the parameters in the case of NpCo using the Toth isotherm. The parameters b, n_T and S are determined primarily by the low-pressure data points; the differences between the estimated values obtained from the range $0 < P \leq 3$ and those obtained from the entire range of pressure $0 < P \leq 9.86$ are around 10 %. The parameter V_m, on the other hand, continues to vary substantially as points are added in the high pressure region, only reaching a plateau as the upper limit on the pressure is approached (with a 60 % difference between $0 < P \leq 3$ and $0 < P \leq 9.86$). Similar results were observed using the other isotherm models as well as the data relating to the other three materials. It is clear, therefore, that in order to estimate the adsorption volume accurately, the data must extend well beyond the saturation point.

Table 4.4: A summary of the estimated physical parameters for each material using each of the standard isotherm models; nonlinear least-squares using equation (4-12) combined with the relevant isotherm.

Isotherm	Parameter	CoIIICu (75 K)	$Cu_3(BTC)_2$ (77 K)	NpCo (75 K)	NpNi (75 K)
Langmuir	q_m / mg g^{-1}	23.7	41.2	18.0	23.9
	S / m^2 g^{-1}	778.2	1329.0	589.9	748.4
	V_m / cm^3 g^{-1}	1.954	0.107	0.350	0.364
	K_L	7.3	1.53	16.6	7.6
L-F	q_m / mg g^{-1}	30.5	48.2	24.6	34.2
	S / m^2 g^{-1}	1002.5	1582.7	807.9	1121.9
	V_m / cm^3 g^{-1}	3.94	0.47	2.20	1.79
	K_{LF}	2.05	0.97	2.46	1.18
	n_{LF}	1.57	1.53	1.86	2.16
D-A	q_m / mg g^{-1}	28.7	41.3	22.7	28.9
	S / m^2 g^{-1}	943.0	1355.9	746.2	949.8
	V_m / cm^3 g^{-1}	3.74	0.19	2.02	1.49
	K_{DA}	6.33	5.27	7.14	6.29
	n_{DA}	2.61	2.69	2.52	1.99
Toth	q_m / mg g^{-1}	35.5	53.7	28.6	34.2
	S / m^2 g^{-1}	1164.5	1761.3	938.3	1122.6
	V_m / cm^3 g^{-1}	4.89	0.64	2.80	1.29
	b	0.271	0.468	0.193	0.234
	n_T	0.436	0.475	0.358	0.340
UNILAN	q_m / mg g^{-1}	33.4	48.7	25.0	30.6
	S / m^2 g^{-1}	1096.6	1599.0	822.07	1005.6
	V_m / cm^3 g^{-1}	4.76	0.57	2.48	1.28
	c	0.436	1.06	0.200	0.418
	n_U	3.47	3.01	3.90	4.22

Table 4.5: Summary of the parameter values obtained for the Toth isotherm equation applied to NpCo at liquid nitrogen temperature using different pressure ranges.

Pressure range (atm)	S (m^2 g^{-1})	V_m (cm^3 g^{-1})	b	n_T
0−1.01	795.50	0.144	0.163	0.417
0−2.32	836.34	1.442	0.172	0.399
0−3.00	850.60	1.746	0.175	0.394
0−4.27	868.14	2.042	0.179	0.386
0−4.94	881.93	2.231	0.182	0.381
0−6.22	897.21	2.413	0.185	0.374
0−6.85	903.84	2.483	0.186	0.372
0−8.15	922.83	2.663	0.190	0.364
0−9.26	937.47	2.790	0.193	0.358
0−9.86	938.33	2.796	0.193	0.358

The parameter values obtained using the L−F D−A, Unilan and Toth models (Table 4.4) are in good qualitative agreement. The last three are capable of capturing the low- and high-pressure behaviour with greater accuracy than either of the Langmuir or L−F equations. Table 4.4 shows that the degree of heterogeneity (increasing s in UNILAN, decreasing n_{DA} and n_T in D−A and Toth, respectively) follows the order $Cu_3(BTC)_2$<CoIIICu<NpCo<NpNi in all cases, which also agrees with the L−F isotherm. The affinity constants (K_{DA} in D−A, 1/b in Toth and 1/c in UNILAN) follow the ordering $Cu_3(BTC)_2$<CoIIICu<NpNi<NpCo; in the case of D−A, the ordering is $Cu_3(BTC)_2$<CoIIICu≈NpNi<NpCo. The reason for the low values for $Cu_3(BTC)_2$ can be seen in the inset in Figure 4.3(b), which shows the excess adsorption isotherms at low pressure for all four materials. At these very low pressures, $Cu_3(BTC)_2$ attains the lowest excess capacity of the four samples. Thus, fitting of the model to the experimental $Cu_3(BTC)_2$ data leads to the lowest value for Henry's constant and, therefore, the smallest affinity constant. For pressures above a few kPa, however, the large surface area of $Cu_3(BTC)_2$ and its low degree of heterogeneity (Table 4.4) lead to the highest excess capacity of all four materials. Further evidence of the low affinity is suggested by the fact that $Cu_3(BTC)_2$, along with CoIIICu, possesses the lowest heat of

adsorption: between 6 and 7 kJ mol^{-1} [28,29], 7.5 kJ mol^{-1} for NpNi and 8.5 kJ mol^{-1} for NpCo [30].

The surface area estimates agree across all isotherms, and are ordered in the manner: NpCo<NpNi<CoIIICu< $Cu_3(BTC)_2$. Estimated values for $Cu_3(BTC)_2$ using standard BET or Langmuir models fitted to nitrogen adsorption data fall in the range 1100−2300 $m^2\ g^{-1}$ [25], while the values predicted in this work fall in the range 1329−1599 $m^2\ g^{-1}$; it is well known that the surface area is a function of the method of preparation and activation [25], and that estimates depend on the probe molecule and equation used (typically Langmuir or BET) [30, 31], which leads to the wide range of values obtained even for the same material. Significant differences between Langmuir and BET are frequently observed [25]. The value estimated by Liu *et al.* in [16] (from where the data originates) using the Langmuir isotherm applied to nitrogen adsorption data was 1482 $m^2\ g^{-1}$, which falls within the range of values predicted in this report. The values predicted for CoIIICu, NpNi and NpCo are higher than the only available estimated values of 730 $m^2\ g^{-1}$ [30], 634 $m^2\ g^{-1}$ and 523 $m^2\ g^{-1}$ [32], respectively; these estimates were based on data for argon adsorption at 77 K up to only 1 atm using BET (CoIIICu) or nitrogen adsorption at 77 K using BET (NpNi and NpCo).

The predicted values of q_m for each material using each isotherm model are also shown in Table 4.4. Eliminating the value obtained from the Langmuir isotherm, for the reasons explained above, the ranges of values for NpNi (29.5−34.8 mg g^{-1}) and NpCo (23.2−25.5 mg g^{-1}) are consistent with experimentally-estimated values of 31.5 mg g^{-1} and 25.7 mg g^{-1}, respectively [33]. Likewise, the range of values obtained for $Cu_3(BTC)_2$ (41.2−53.7 mg g^{-1}) is consistent with the maximum obtained excess capacity for $Cu_3(BTC)_2$ in Liu *et al.* [16] (around 41 mg g^{-1}). The latter is not identical to q_m but represents a lower bound on the actual value. The values for CoIIICu (29.3−36.1 mg g^{-1}) are somewhat higher than the measured value of 18 mg g^{-1} in [30]. The lower limit, on the other hand, is close to the value of 26.1 mg g^{-1} reported in [27]. The major cause of these differences is the method of preparation and activation.

4.5.3 Adsorption isotherms

Figure 4.4(a) (CuIIICo), Figure 4.5(a) ($Cu_3(BTC)_2$), Figure 4.6(a) (NpCo) and Figure 4.7(a) (NpNi) show the comparison between the experimental and model excess

capacities in mg H_2 per g of solid using the five model isotherms. The corresponding excess (predicted and experimental), absolute and compressed-gas specific masses in mg H_2 per g of solid are shown in Figures 4.4(b), 4.5(b), 4.6(b) and 4.7(b). From Figures 4.4(a)−4.7(a), it is clear that the Langmuir isotherm performs poorly for pressures above 1 atm, which is also evident from the low coefficients of determination R^2 in Table 4.4. The L−F, D−A, Toth and Unilan perform extremely well in all cases, as is also seen from Table 4.4.

Figures 4.4(b) and 4.7(b) show that, in contrast to the excess results, CoIIICu exhibits a markedly higher absolute capacity than the NpNi sample (almost 32 mg g^{-1} compared to around 27 mg g^{-1} at 10 atm). The term $\varepsilon/\left((1-\varepsilon)\rho_s\right)$ (or V_{pore}) in equation (4-13) is the material-dependent part of the compressed gas term $\rho_g V_g/(\rho_b V_b)$ and as Table 4.1 shows, the value of V_{pore} for CoIIICu is appreciably higher than the equivalent value for NpNi. The slope of the straight line ($\rho_g V_g/(\rho_b V_b)$) in Figure 4.4(b) is therefore steeper than the slope of the equivalent line in Figure 4.7(b).

It is not possible to measure the adsorbed mass $M_{\mathrm{H}_2(a)}$ directly; as has already been discussed, the experimentally accessible quantity is the excess value m_e. With knowledge of V_a (which itself is not directly measureable), however, the adsorbed mass can be estimated from equation (4-8). The adsorption volume can also be used to estimate the average number of adsorbate layers $\lambda = V_a/s\sigma$, where σ is the average reach of an adsorbate molecule [34]. Figure 4.8 shows the simulated adsorption volumes V_a as functions of pressure for CoIIICu and NpCo using each of the five isotherms (results for the other two materials are similar). It is immediately noticeable that the Langmuir isotherm yields significantly smaller volumes than the other isotherms. This is not surprising since the assumption of a homogeneous surface implies a smaller adsorption-layer thickness. The curves obtained using Unilan and Toth agree well in both cases, as do the curves obtained using D−A and L−F. There are, on the other hand, relatively small but significant differences between these two sets of curves. A similar picture emerges in the curves for the adsorbed mass $m_a = M_{\mathrm{H}_2(a)}/\rho_b V_b$ (in mg g^{-1}) shown in Figure 4.9.

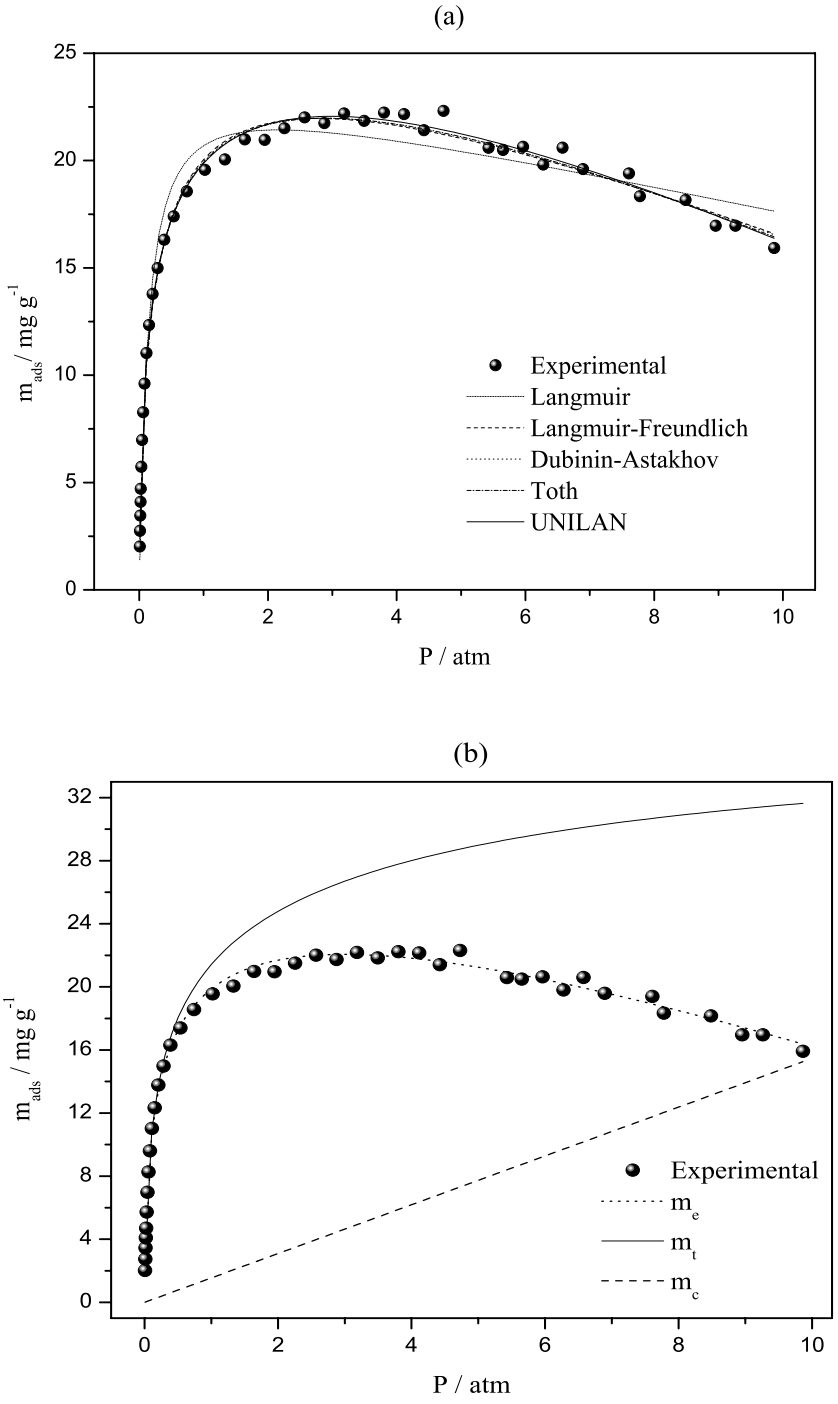

Figure 4.4: (a) A comparison between the experimental and model excess capacities for CuIIICo at 75 K (in mg H_2 per g of solid) using the five model isotherms.(b) The corresponding excess, absolute and compressed-gas specific masses (in mg H_2 per g of solid).

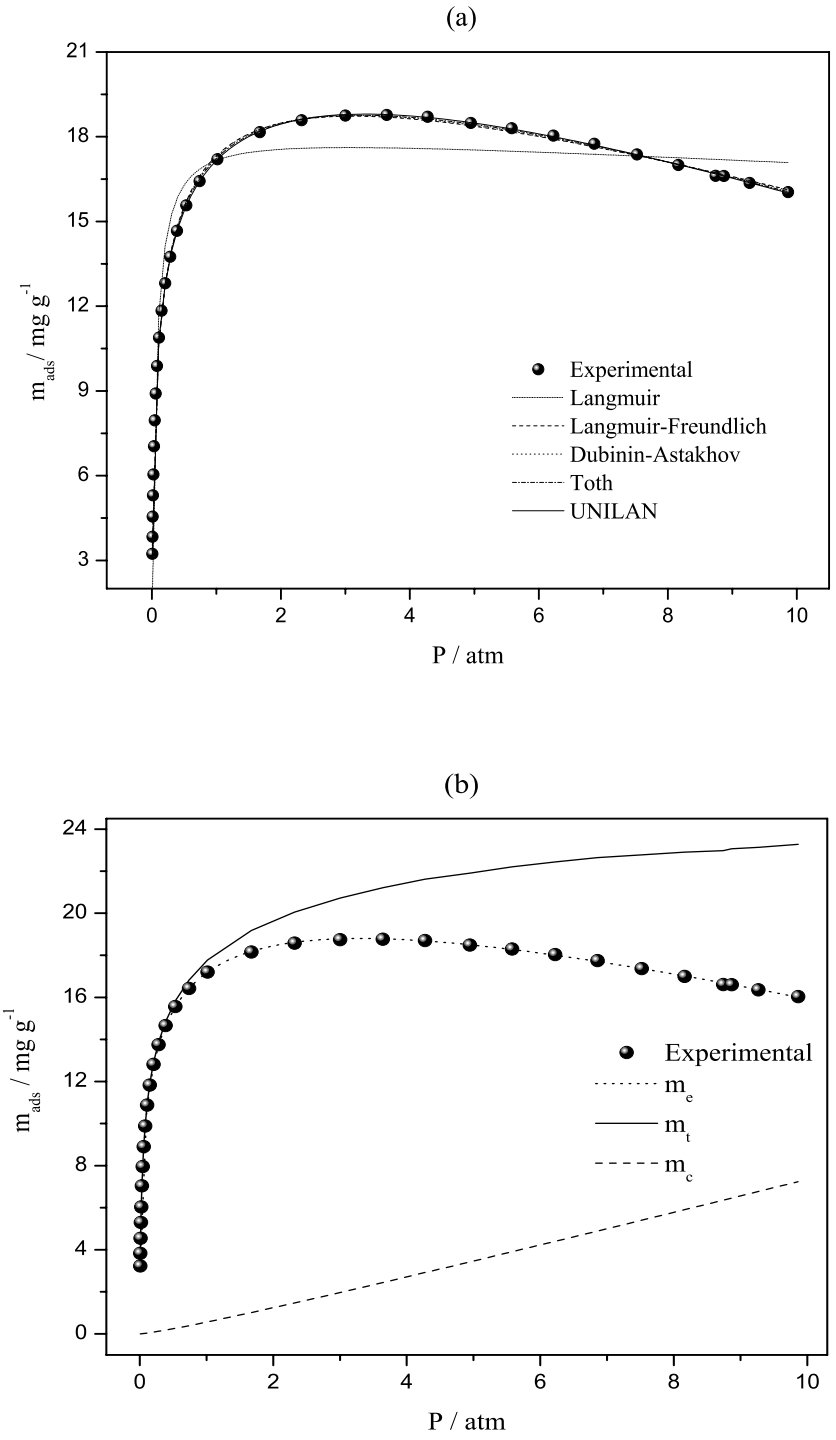

Figure 4.5: (a) A comparison between the experimental and model excess capacities for $Cu_3(BTC)_2$ at 77 K (in mg H_2 per g of solid) using the five model isotherms. (b) The corresponding excess, absolute and compressed-gas specific masses (in mg H_2 per g of solid).

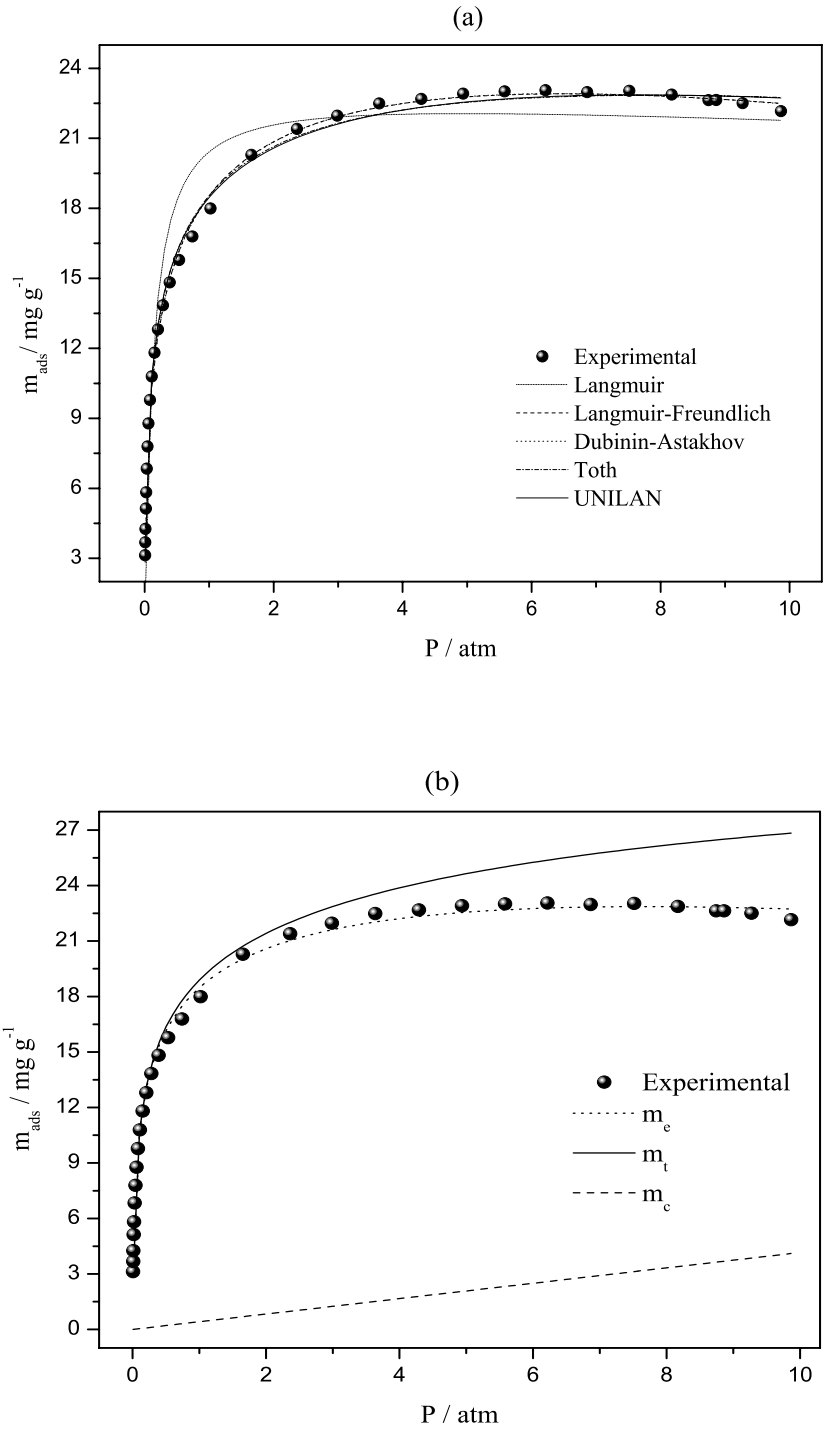

Figure 4.6: (a) A comparison between the experimental and model excess capacities for NpCo at 75 K (in mg H_2 per g of solid) using the five model isotherms. (b) The corresponding excess, absolute and compressed-gas specific masses (in mg H_2 per g of solid).

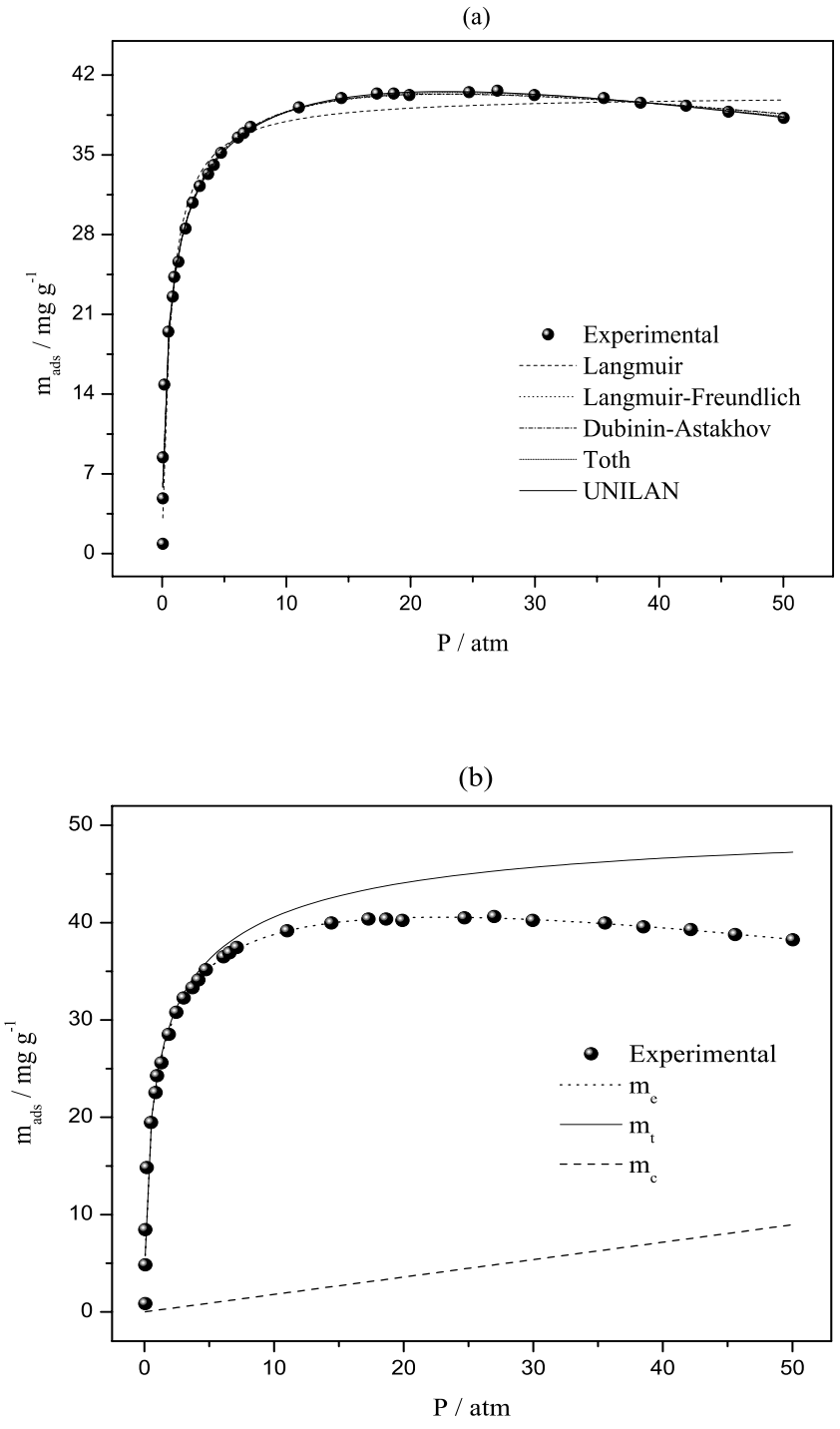

Figure 4.7: (a) A comparison between the experimental and model excess capacities for NpNi at 75 K (in mg H_2 per g of solid) using the five model isotherms. (b) The corresponding excess, absolute and compressed-gas specific masses (in mg H_2 per g of solid).

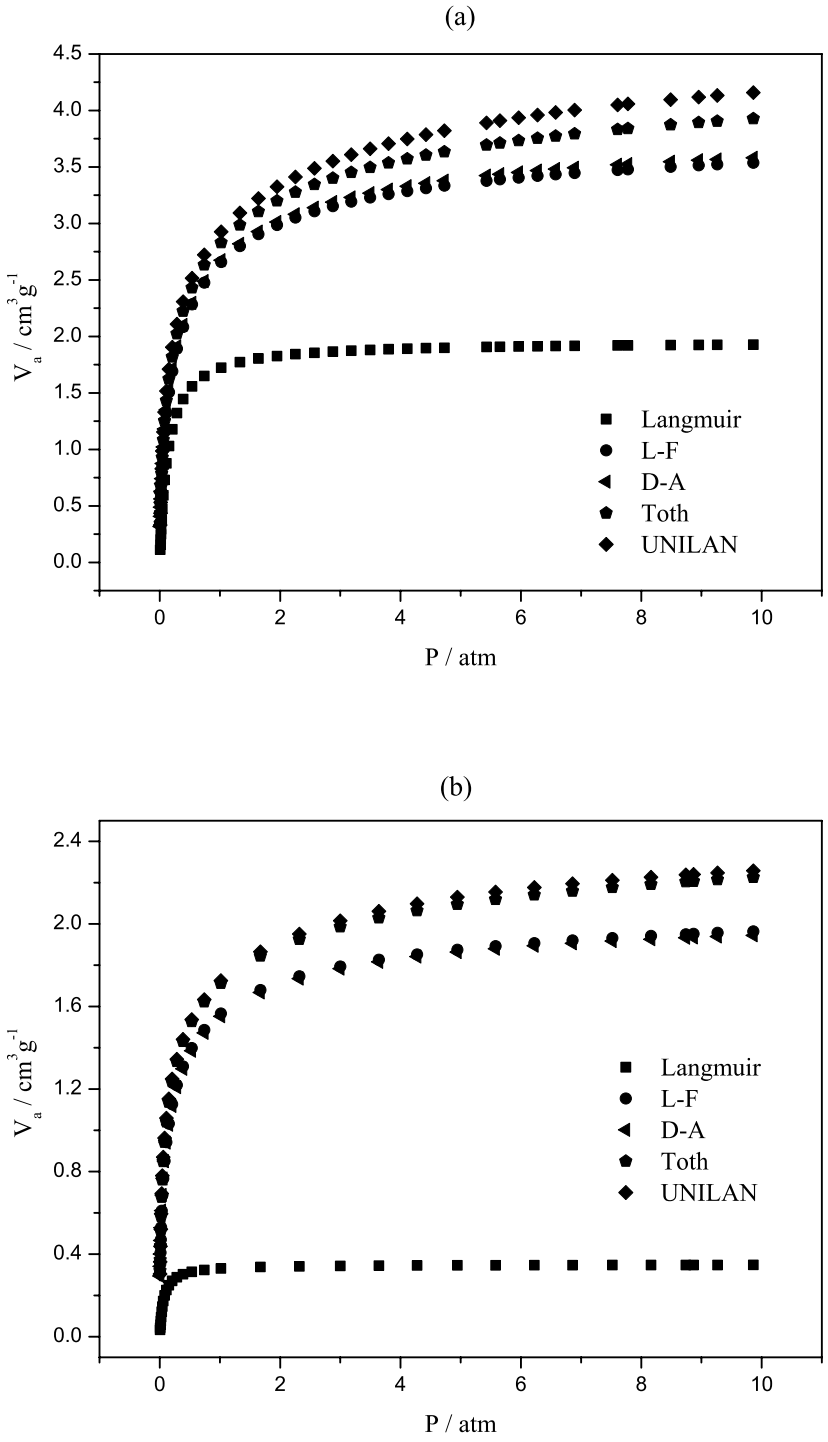

Figure 4.8: Simulated adsorption volumes V_a as functions of pressure corresponding to adsorption in (a) CoIIICu and (b) NpCo at 75 K using equation (10) and each of the five standard isotherms.

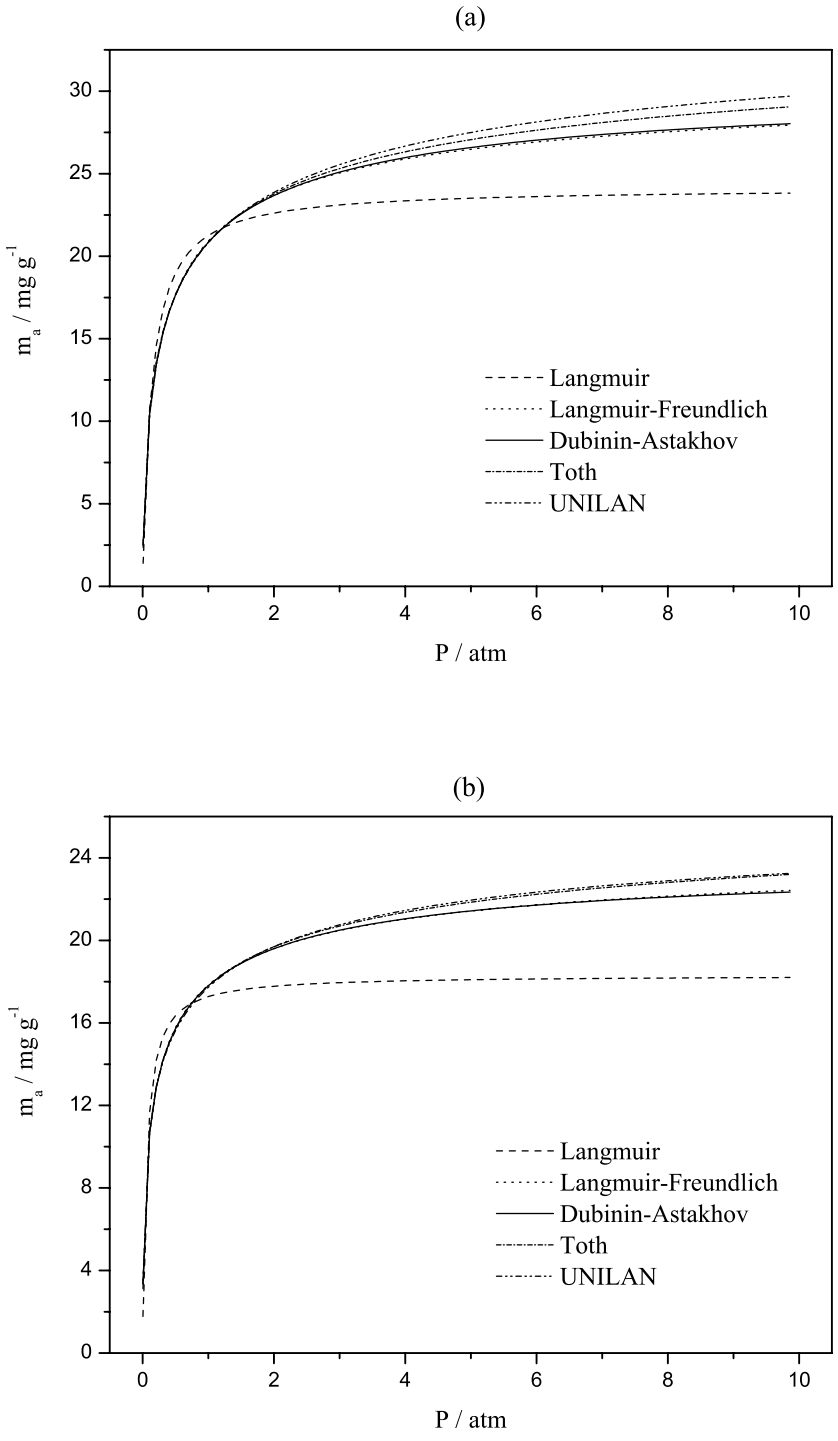

Figure 4.9: Simulated condensed-phase masses $m_a = M_{\mathrm{H}_2(a)} / \rho_b V_b$ corresponding to adsorption in (a) CoIIICu and (b) NpCo at 75 K using equation (8) and each of the five standard isotherms.

Neither the L−F isotherm nor the D−A isotherm obays Henry's law at low pressures. The D−A equation also relies on the saturation vapour pressure P_s at the adsorption temperature T to estimate the adsorption potential $\psi = RT\ln(P_s/P)$. Under super-critical temperatures, i.e. above 33 K, P_s is replaced with a pseudo saturation vapour pressure. Amankwah and Schwarz [35] proposed a general form $P_s = P_c(T/T_c)^r$ for the Dubinin expression, where r is a free parameter (a value of r = 2 was used here) and showed that the values of r lie between 2.7 and 4.16 for hydrogen storage in four microporous carbon materials. For these reasons, it is suspected that the Toth and Unilan models provide more accurate predictions, although this cannot be verified at the present time.

The effects of gas compressibility (at high pressures) on the parameter values derived can be illustrated by replacing the ideal gas law in the above analysis with the modified gas law:

$$\rho = \frac{pm_{H_2}}{ZRT} \tag{4-24}$$

where the compressibility factor Z is given by [36]:

$$\begin{aligned} Z = &\left[1.000547 - \left(6.07\times10^{-7}\right)T\right] + \left[0.000912 - \left(1.0653\times10^{-6}\right)T\right]P \\ &+ \left[\left(7.373407 - 0.0901T\right)10^{-7}\right]P^2 \end{aligned} \tag{4-25}$$

with units of atm for the pressure and K for the temperature. For the conditions under consideration in this paper, the highest value of the compressibility factor (50 atm, 77 K) is around 1.04. When the contribution of the gas phase to the total mass is taken into account, the differences between the values with and without the use of the compressibility factor are negligibly small, e.g., the surface area changed by 0.17% using the Langmuir model applied to $Cu_3(BTC)_2$. For higher temperatures and/or higher pressures, the differences can, on the other hand, be significant.

References

[1] Brunaur S., Deming L.S., Deming W.S., Teller E., J. Am. Chem. Soc. 62 (1940) 1723−1732.

[2] Khalfaoui M., Knani S., Hachicha M.A., Ben Lamine A., J. Coll. Inter. Sci. 263 (2003) 350–356.

[3] Gregg S.J., Sing K.S.W., Adsorption, Surface Area and Porosity, 1982, Academic Press, London and New York.

[4] Sing K.S.W., Everett D.H., Haul R.A.W., Moscou L., Pierotti R.A., Rouquerol J., Siemieniewska T., Pure Appl. Chem. 57 (1985) 603−619.

[5] Rouqerol F., Sing K.S.W., Adsorption by powder and porous solids, 1999, Academic Press Inc., London.

[6] Chang S., Clair B., Ruelle J., Beauche J., Di Renzo F., Quignard F., Zhao G.J., Yamamoto H., J. Experimental Botany 60 (2009) 3023–3030.

[7] Sing S.W., Everett D.H., Haul R.A.W., Moscou L., Pierotti R.A., Rouquerol J., Siemienswska T., Pure Appl. Chem. 57 (1985) 603–619.

[8] Gelb L.D., Gubbins K.E., Radhakrishnan R., Sliwinska-Bartkowiak M., Reports on Progress in Physics 62 (1999) 1573–1659.

[9] Lowell S., Shields J.E., Thomas M.A., Thommes M., Characterisation of Porous Solid and Powders: Surface Area, Pore Size and Density, Kluwer, 2004, Academic Publishers.

[10] Lowell S., Shields J.E., Powder Surface Area and Porosity. 3rd ed., 1991: Chapman & Hall.

[11] Do D.D., Adsorption Analysis: Equilibria and Kinetics, 1998: Imperial College Press, London.

[12] Zhou L., Zhou Y.P., Chem. Eng. Sci. 53 (1998) 2531–2536.

[13] Zhou L., Zhou Y.P., Sun Y., Int. J. Hydrogen Energy 29 (2004) 319−322.

[14] Zhou L., Zhou Y.P., Sun Y., Int. J. Hydrogen Energy 31 (2006) 259−264.

[15] Zhou L, Zhang J., Langmuir 17 (2001) 5503–5507.

[16] Liu J., Culp J.T., Natesakhawat S., Bockrath B.C., Zande B., Sankar S.G., Garberoglio G., Johnson J.K., J. Phys. Chem. C 111 (2007) 9305–9313.

[17] Mori D., Hirose K., Int. J. Hydrogen Energy 34 (2009) 4569-4574.

[18] Kalavathy M.H., Karthikeyan Rajgopal T.S., Miranda L.R., J. Coll. Int. Sci. 292 (2005) 354−362.

[19] Bering B.P., Dubinin M.M., Serpinskii V.V., J. Coll. Int. Sci. 38 (1972) 185–194.

[20] Dubinin M.M., Progress in Membrane and Surface Science, Vol. 9, Chapter 1, 1975: Academic Press, New York.

[21] Dubinin M.M., Chem. Rev. 60 (1960) 235−241.

[22] Himeno S., Komatsu T., Fujita S., J. Chem. Eng. Data 50 (2005) 369−376.

[23] Terzyk A.P., Chatlas J., Gauden P.A., Rychlicki G., Kowalczyk P., J. Coll. Int. Sci. 266 (2003) 473−476.

[24] Murray L.J., Dinca M., Long J.R., Chem. Soc. Rev. 38 (2009) 1294−1314.

[25] Thomas K.M., Dalton Trans. (2009) 1487−1505.

[26] Zhan L., Li K.X., Zhang R., Liu Q.F., Lu C.X., Ling L.C., J. Supercrit. Fluids 28 (2004) 37−45.

[27] Krap C.P., Balmaseda J., del Castillo L.F., Zamora B., Reguera E., Energy & Fuels 24 (2010) 581−589.

[28] Reguera L., Balmaseda J., Krap C.P., Reguera E., J. Phys. Chem. B 112 (2008) 10490−10501.

[29] Balmaseda J., Reguera E., Gomez A., Roque J., Vazquez C., Autie, M., J. Phys. Chem. B 107 (2003) 11360−11369.

[30] Kaye S.S., Long J.R., J. Am. Chem. Soc. 127 (2005) 6506−6507.

[31] Düren F., Millange T.F., Férey G., J. Phys. Chem. C 111 (2007) 15350–15356.

[32] Culp J.T., Matranga C., Smith M., Bittner E.W., Bockrath B., Phys. Chem. B 110 (2006) 8325–8328.

[33] Reguera L., Roque J., Hernandez J., Reguera E., Int. J. Hydrogen Energy 35 (2010) 12864−12869.

[34] Zhou L., Bai S., Su W., Yang J., Zhou Y., Langmuir 19 (2003) 2683–2690.

[35] Amankwah K.A.G., Schwarz J.A., Carbon 33 (1995) 1313-1319.

[36] Ye Y., Interaction of hydrogen with novel carbon materials. PhD Thesis, California Institute of Technology, 2001.

Chapter 5: Sorption of hydrogen on titanate nanotubes decorated with nanostructured Prussian blue analogues

5.1 Introduction

Titanate nanotubes (TiNTs) have attracted a great deal of interest for a number of potential applications due their promising properties. Although pure TiNTs exhibit only moderate values of hydrogen uptake (*ca*. 4 wt. % at 77 K [1]), due to the relatively high atomic weight of the titanium atoms, there are some indications that this value can be increased by the intercalation of transition metals between the layers of multi-walled nanotubes (MWNT) [2,3]. In this chapter, the Prussian Blue (PB) analogue, cadmium hexacyanoferrate (III), $Cd_3[Fe(CN)_6]_2$ (denoted Cd_3Fe^{III} in the sequel), which is known to have good hydrogen sorption properties [4], was deposited on the surfaces of TiNTs by a two-step method: the ion-exchange of TiNTs with Cd^{2+} ions and the reaction with $K_3[Fe(CN)_6]$, given by Eqns. (3-1) and (3-2). In the particular case of Cd, to form the composite Cd_3Fe^{III}/TiNT, the reactions are:

$$x\mathrm{Cd}^{+2}(aq) + \mathrm{H_2Ti_3O_7}(s) \rightarrow \mathrm{Cd}_x\mathrm{H}_{2(1-x)}\mathrm{Ti_3O_7}(s) + 2x\mathrm{H}^{+} \tag{5-1}$$

$$\mathrm{Cd}_x\mathrm{H}_{2(1-x)}\mathrm{Ti_3O_7}(s) + \frac{2x}{3}\mathrm{K_3[Fe(CN)_6]}(aq) \rightarrow \left(\mathrm{Cd_3[Fe(CN)_6]_2}\right)_{x/3}\mathrm{K}_{2x}\mathrm{H}_{2(1-x)}\mathrm{Ti_3O_7}(s) \tag{5-2}$$

Note that the ion-exchange reaction cannot involve complete exchange of hydrogen with Cd, as show in equation (5-1). During the second step (5-2), cadmium ions contained in the TiNTs exchange with the potassium to form insoluble –Fe–CN–Cd– chains deposited on the TiNT surfaces. The negative charge on the Ti_3O_7 following the formation of $Cd_3[Fe(CN)_6]_2$ on the TiNT surfaces is balanced by potassium ions. The

choice of Cd as the outer metal in the PB analogue was motivated by hydrogen adsorption experiments that are discussed at the end of this chapter.

The peculiarities of hydrogen sorption onto the Cd_3Fe^{III}/TiNT composite were investigated over a wide range of pressures (up to 150 bar) and temperatures (from 77 K to 298 K). The results suggest a strong synergy between the TiNT and Cd_3Fe^{III} in the composite, resulting in a considerably higher level of hydrogen uptake than for each of the bulk materials. In the following, the morphology, structure, composition and, properties of hydrogen adsorption onto the Cd_3Fe_2/TiNTs composite will be discussed in details.

5.2 Results and discussion

5.2.1 Cd_3Fe^{III}/TiNTs composite characterization

EDX spectra confirm the incorporation of cadmium ions to TiNTs when these nanostructures interact with an aqueous solution of Cd^{2+} (see Figure 5.1). The spectra recorded for the powder obtained after the immersion of the exchanged samples in a solution of $K_3[Fe(CN)_6]$ reveals the presence of K and Fe. This confirms that in the second step (5-2), K^+ ions are present at the TiNT surfaces in order to balance the negative charge on the Cd_3Fe^{III}/TiNT structure. According to the results of the EDX analysis, the solid Cd_3Fe^{III}/TiNT composite obtained by the combined reactions, (5-1) and (5-2), consists of approximately 10 wt. % of Cd_3Fe^{III} and 90% of H-TiNTs ion-exchanged with potassium ions.

Figure 5.2a shows a TEM image of nanostructured Cd_3Fe^{III} deposited on the surface of the TiNT nanotubes. In contrast to CdS [5], precipitated Cd_3Fe^{III} does not form spheroidal particles on the surfaces of the TiNTs, but is instead deposited in the form of an unstructured, discontinuous film with an extended interface. The SEM image composite in Figure 5.2b shows that Cd_3Fe^{III} is evenly distributed throughout the sample of nanotubes without significant change in morphology of nanotubes. Occasionally, probably due to the reaction of $K_3[Fe(CN)_6]$ with impurities of unwashed $CdSO_4$ in the bulk solution, there is appearance of large (ca. 100 nm) particles of

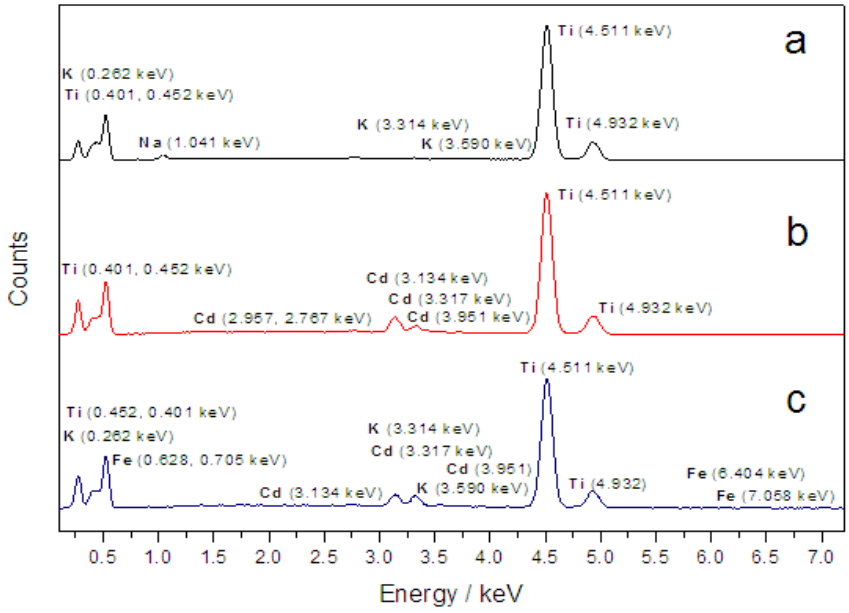

Figure 5.1: EDX spectra for: (a) TiNT (b) Cd_3Fe^{III}; (c) Cd_3Fe^{III}/ TiNTs composite.

Cd_3Fe^{III} (see the inset in Figure 5.2b) loosely attached to the nanotubes. Comparisons of TEM images of the original and modified with Cd_3Fe^{III} nanotubes (see Figure 5.2a and c) shows that after deposition both the inner and outer smooth surfaces of the nanotubes are corrugated, which suggests that precipitation of Cd_3Fe^{III} occurs on both surfaces of the nanotubes. It also results in smearing of the lattice fringes of initial uncoated TiNT observed in all TEM images. Furthermore, the observed morphology of the Cd_3Fe^{III} nanostructures is very different from the morphology obtained by precipitation in the absence of TiNTs. Figure 5.2d shows that the pure bulk Cd_3Fe_2 forms cuboidal shape crystals with sizes varying from 100 to 200 nm.

Figure 5.3 shows the XRD patterns for original TiNTs, the bulk Cd_3Fe^{III} and the composite Cd_3Fe^{III}/TiNT. The diffraction pattern from the composite sample contains characteristic reflections from both TiNT and Cd_3Fe^{III} nanoparticles, indicating that reactions (5-1) and (5-2) do not significantly alter the crystal structure of the TiNTs during reversible ion-exchange and that the precipitates of Cd_3Fe^{III} possess a well-established crystal structure. Cadmium ferricyanide in the composite is found to form a well structured phase on the TiNT surfaces. This supports the hypothesis that

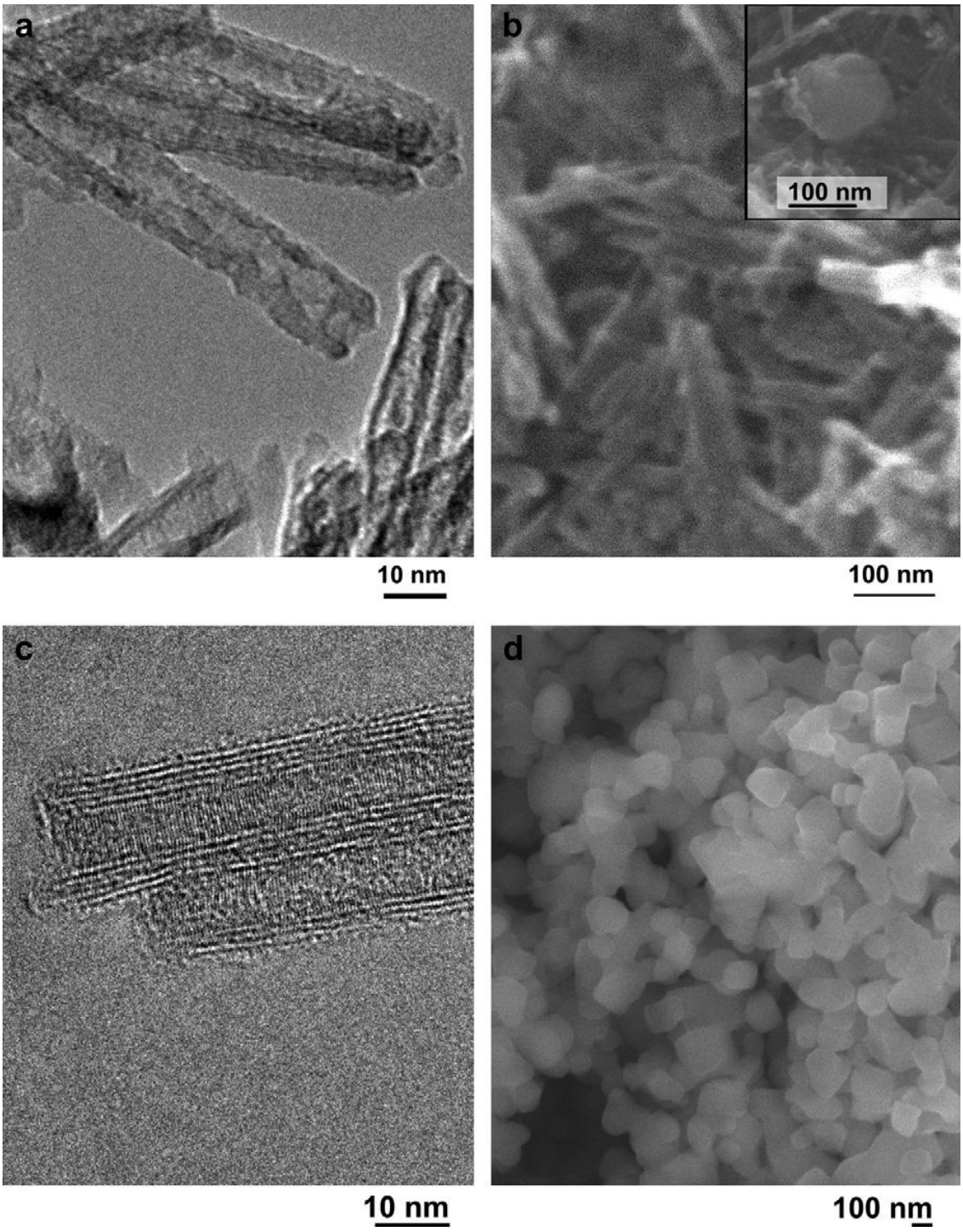

Figure 5.2: Electron microscope (a) TEM and (b) SEM images of nanostructured $Cd_3[Fe(CN)_6]_2$ deposited on the surface of titanate nanotubes; (c) HRTEM image of uncoated TiNTs, (d) SEM image of bulk $Cd_3[Fe(CN)_6]_2$. Inset in (b) shows an occasional single nanoparticle of $Cd_3[Fe(CN)_6]_2$.

upon the addition of $K_3[Fe(CN)_6]$ aqueous solution to cadmium exchanged TiNTs, the cadmium ions migrate to the nanotube surfaces to form –Fe–CN–Cd– chains. This process is accompanied by the incorporation of K^+ ions into the exchangeable sites of TiNTs.

The grain size of crystallites for bulk Cd_3Fe^{III} and the composite Cd_3Fe^{III}/TiNT can be calculated using a well-known Scherrer formula [6]:

$$D_p = \frac{K\lambda}{\beta \cos\theta} \tag{5-3}$$

where D_p is the mean diameter, K is the Scherrer constant (between 0.89–0.94), which is dependent on the crystallite shape, λ is wavelength of the X-ray used, β is the full-width at half maximum (FWHM), and θ is the angle of diffraction. The FWHM of the (200) reflections from cadmium hexacyanoferrate (III) in both the bulk and composite samples are approximately equal to 0.12185 and 0.0996 deg, respectively. From the Scherrer formula, the size of the coherent scattering domains can be estimated as 69 and 84 nm for bulk Cd_3Fe^{III} and the composite Cd_3Fe^{III}/TiNT, respectively, which is in agreement with SEM data (see Figure 5.2d and inset in Figure 5.2b). Such large particles of Cd_3Fe^{III} in the composite are characterised by poor adhesion to the TiNT, resulting in their progressive removal under treatment of the aqueous suspension of the composite with ultrasound followed by washing.

FTIR spectra sheds light on the nature of the obtained composite. Figure 5.4 shows the ν(CN) vibration region of the bulk Cd_3Fe^{III} and the composite Cd_3Fe^{III}/TiNT. The range of wavenumbers characteristic to the vibrations of CN groups (between 2200 and 2000 cm^{-1}) confirms the presence of the PB analogue in the composite. Both samples are characterised by the presence of a band at 2154 cm^{-1} (attributed to the stretching vibrations of cyanic group in the $-Fe^{3+}-CN-Cd^{2+}-$ chains [8]), which is slightly shifted to lower energies in the case of the composite (2152 cm^{-1}). Two weak bands at 2120 and 2116 cm^{-1} can be ascribed to impurities of Cd_3Fe^{III} trapped in the composite structure or associated with the strong interface between Cd_3Fe^{III} and TiNT in the composite. The sample of pure TiNTs is transparent in the studied region of wavenumbers. The information derived from FTIR spectra is consistent with the results with the results from EDX spectra discussed above (Figure 5.1).

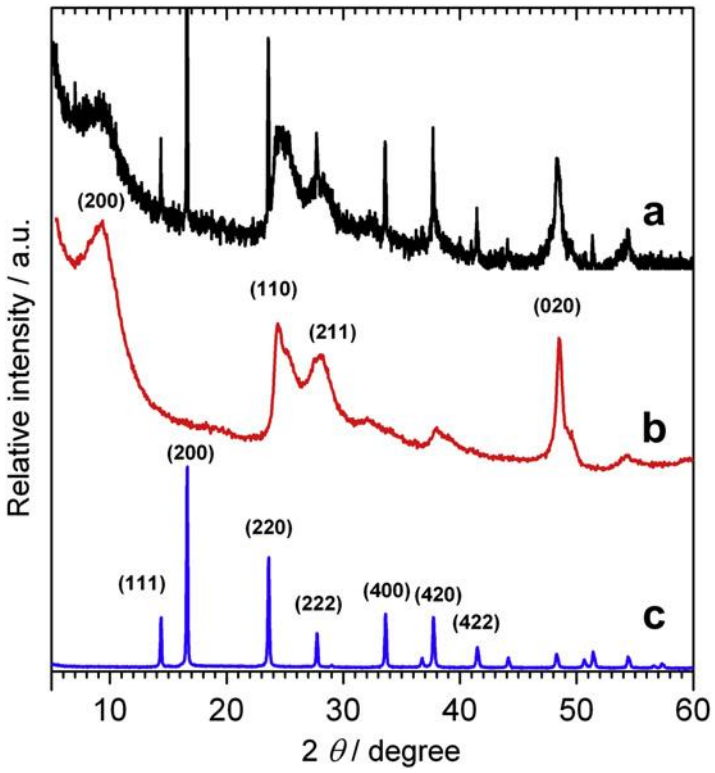

Figure 5.3: XRD patterns of (a) Cd_3Fe^{III}/TiNT composite, (b) TiNT support and (c) bulk Cd_3Fe^{III} nanoparticles. Miller indexes for Cd_3Fe^{III} were taken from reference [7] and for TiNT, from reference [1].

Nitrogen adsorption data confirmed a high degree of dispersion of Cd_3Fe^{III} in the composite. According to the IUPAC classification (see Chapter 4), the isotherm of nitrogen adsorption on the surface of the Cd_3Fe^{III}/TiNT composite ((Figure 5.5) can be described as a combination of type I and type IV isotherms, with a characteristic hysteresis associated with the mesoporous structure of TiNT [9]. In contrast, the isotherm of nitrogen adsorption on bulk Cd_3Fe^{III} corresponds to a type I isotherm, attributable to adsorption in microporous materials [7], with a mild hysteresis associated with capillary condensation in the pores formed by the agglomeration of cuboidal particles.

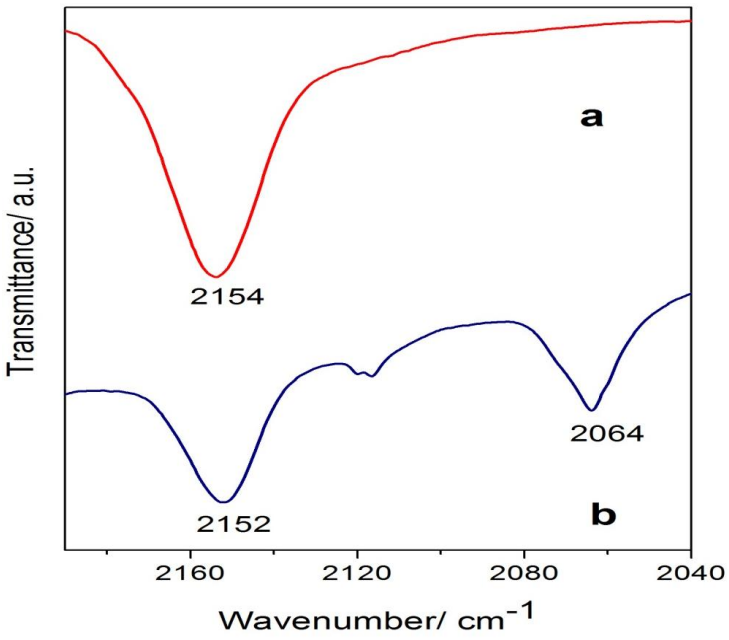

Figure 5.4: FTIR spectra of (a) bulk Cd_3Fe^{III} nanoparticles and (b) Cd_3Fe^{III}/TiNT composite. (TiNT are transparent in the region from 2040 to 2200 cm^{-1}).

Overall, the nitrogen adsorption properties of the composite are similar to those of mesoporous TiNTs. Decoration of the nanotubes with Cd_3Fe^{III}, however, results in an increase in the BET surface area from 210 m^2 g^{-1} to 244 m^2 g^{-1}, and an increase in the total pore volume from 0.64 cm^3 g^{-1} to 0.67 cm^3 g^{-1}. This confirms that, despite blocking of the titanate surfaces, the precipitated material develops the microporous structure of the base metal of ferricyanide, which does not block access to the mesoporeses of the nanotubes. Taking into account that the BET surface area of bulk Cd_3Fe^{III} is approximately 556 m^2 g^{-1} and that the loading of Cd_3Fe^{III} on TiNTs is approximately 10 wt. %, the combined surface area is estimated to be $0.9 \times 210 + 0.1 \times 556 = 245$ m^2 g^{-1}, which is very close to the observed specific surface area of the composite.

The BJH pore size distributions for the composite and the pure components are shown in Figure 5.6. The peak for the composite is shifted to a slightly larger pore diameter compared to the pure TiNT. This may be due to changes in the agglomeration of the nanotubes after decoration, such that the average distance between the agglomerates increases. The BJH pore size distribution of bulk Cd_3Fe^{III} reveals only a small

contribution from the mesopores to the total pore volume (0.36 $cm^3 g^{-1}$), suggesting that the total pore volume corresponds primarily to micropores. These micropores are also present in the composite sample, as can be concluded from the increased values of the pore volume at small pore sizes in Figure 5.6.

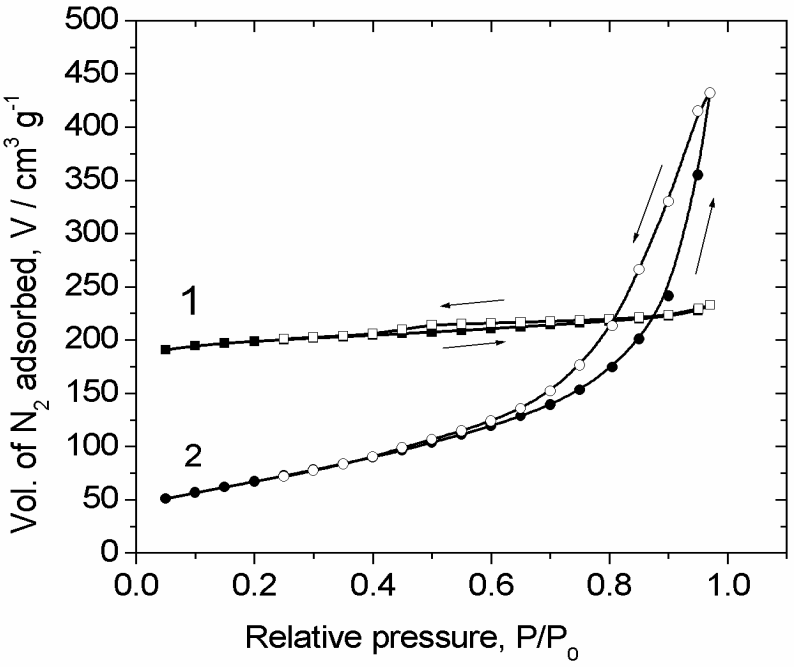

Figure 5.5: Isotherm of nitrogen adsorption and desorption at 77 K on the surface of (1) bulk Cd_3Fe^{III} and (2) Cd_3Fe^{III}/TiNTs composite. Arrows indicate the direction of pressure change.

5.2.2 Hydrogen sorption properties

Figure 5.7 shows the isotherms of excess adsorption and desorption of hydrogen in the Cd_3Fe^{III}/TiNT composite at 77 K, measured in the range 0 to 45 bar. The excess is defined as the amount of hydrogen taken up beyond what would be contained within a free volume equivalent to the total pore volume of the sample (at the same temperature and pressure) [10]. The adsorption/desorption behaviour is characterised by a broad hysteresis loop, which can be associated with the existence of two types of adsorption sites in the composite. The hydrogen adsorption curve for the composite can be considered as a two-step isotherm of type VI according to the IUPAC classification (Chapter 4), where the first step is observed over the range of pressures from 0 to ca. 5 bar and the second occurs at higher pressures.

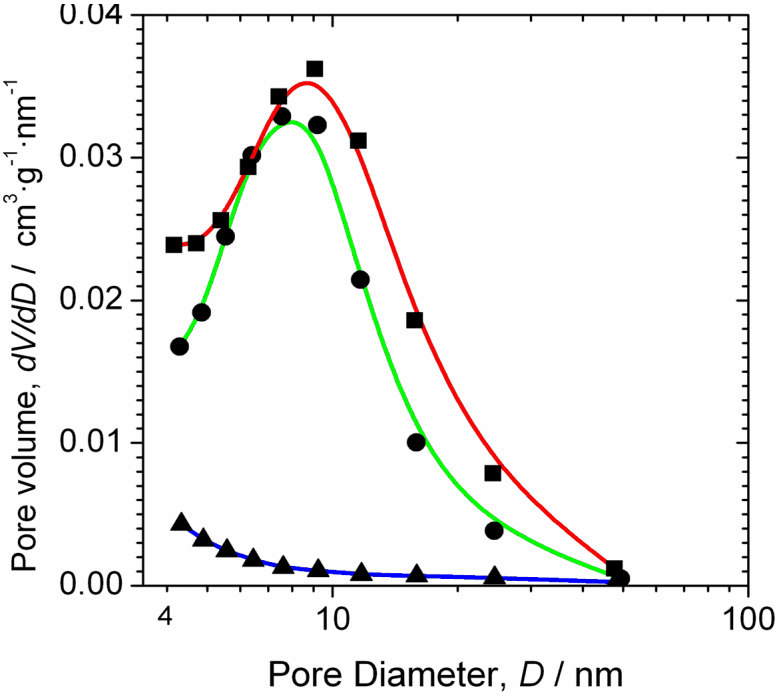

Figure 5.6: Pore volume distribution (BJH desorption of nitrogen) of (●) titanate nanotubes; BET surface area 210 m^2g^{-1}; total pore volume 0.64 cm^3g^{-1}, (■)Cd_3Fe^{III}/TiNTs composite; BET surface area 244 m^2g^{-1}; total pore volume 0.67 cm^3g^{-1} and (▲) bulk Cd_3Fe^{III}; BET surface area 556 m^2g^{-1}; total pore volume 0.36 cm^3g^{-1}.

The hydrogen adsorption in the lower pressure range occurs on the centres that are always accessible to the hydrogen, whereas at higher pressure and larger surface coverage, the enhancement of adsorption can be initiated by the local electric field gradient intrinsic to PB analogue systems [11]. Such isotherms are usually characterised by a broad hysteresis. The adsorption curve in the Cd_3Fe^{III}/TiNT composite is characterised by good reproducibility after several adsorption/desorption cycles, indicating a high degree of reversibility of the hydrogen storage composite.

The two-step nature of the adsorption isotherm is more pronounced when a broader range of pressures is used. Figure 5.8 shows a hydrogen adsorption isotherm on the uncoated TiNT, bulk Cd_3Fe^{III} and Cd_3Fe^{III}/TiNT composite up to 140 bar at 77 K. The shape of the isotherm of excess hydrogen adsorption in Cd_3Fe^{III} is consistent with previous reports [4,12], i.e., a monotonic two-step increase followed by a decrease of

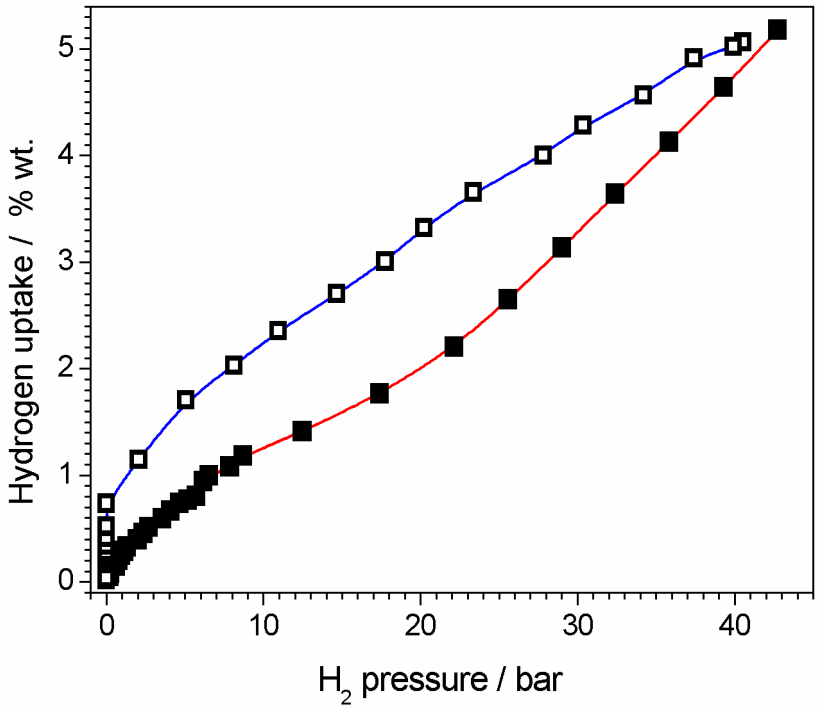

Figure 5.7: Experimental isotherm of hydrogen adsorption (■) and desorption (□) at 77K on the surface of Cd_3Fe^{III}/TiNTs composite.

the excess hydrogen uptake beyond a maximum value of 4 wt. % at approximately 90 bar. The decrease of excess hydrogen uptake after 90 bar is due to saturation of the adsorbent surface with hydrogen, while the bulk gas density continues to increase [12]. This behaviour has been observed in other PB-type materials, often at much lower pressures, for example, at around 3 bar for $Cu_3[Co(CN)_6]_2$ [13].

In contrast, adsorption of hydrogen into the pores of TiNT is characterised by a featureless monotonically increasing function (adsorption curve), reaching approximately 4.5 wt. % of hydrogen uptake at 90 bar. The hydrogen uptake at pressures below 2 bar (see the inset in Figure 5.8) is greater for the bulk Cd_3Fe^{III} than for the nanotubes, probably as a result of the smaller BET surface area of the nanotubes and the availability of unsaturated metal coordination sites in the structure of Cd_3Fe^{III}, which typically contain transition metals with an open coordination environment and are highly attractive to hydrogen molecules [12,14]. At pressures above 90 bar, on the other hand, the level of hydrogen sorption on the nanotubes is higher, which may be attributed to the restricted access of molecular hydrogen to the interstitial cavities between layers in the nanotube walls [1].

The isotherm of hydrogen adsorption of hypothetical 10:90 wt.:wt. mixture of non interacting Cd_3Fe^{III} with TiNT can be calculated as a linear combination of the original isotherms for each component, weighted by the corresponding mass fractions (see Figure 5.8). The simulated curve fits the experimental data up to a pressure of 2 bar. Further increasing the pressure leads to an increasingly severe underestimation of the excess hydrogen uptake. The experimentally determined uptake of hydrogen in the composite steadily grows until approximately 15 wt. % at a pressure of 150 bar, while according to the simulated curve, the excess uptake should be only 4.3 wt. % at the same pressure. Such a large difference between the simulated and measured isotherms indicates that hydrogen adsorption on the composite cannot be approximated by a linear combination of isotherms for each component, due to a strong interaction between the nanostructured film of Cd_3Fe^{III} and the TiNT substrate. The two-step shape of the isotherm curve for the composite material is similar to that for bulk Cd_3Fe^{III}, suggesting that a similar mechanism of adsorption into the micropores of deposited Cd_3Fe^{III} dictates the adsorption in the composite. In the case of the composite, however, the capacity is increased dramatically.

The strong interaction between Cd_3Fe^{III} and TiNT is also suggested by the well-developed interface between these two phases, as seen in Figure 5.2a. This can be attributed to the good ion-exchange properties of TiNTs, which facilitates the exchange of all cations, including Cd^{2+}, K^+ and H^+, leading to an increased affinity of cadmium hexacyanoferrate (III) to the TiNTs surface. Moreover, the close proximity of K^+ ions within the TiNT lattice to the film of nanostructured Cd_3Fe^{III} can create local charge centres capable of participating in hydrogen adsorption through electrostatic interactions [12], which usually dominate adsorption at relatively high coverage/pressure. Such centres are probably interfaced between TiNT and Cd_3Fe^{III} phases, creating a local electric field gradient which is an additional contribution to the adsorption potential for the hydrogen molecule [11]. Further studies of the alteration of the Cd_3Fe^{III} /TiNT interface, achieved by variation of the preparation methods (including pH, mixing sequence, presence of additives) accompanied by further studies of hydrogen sorption in such composites, would reveal a better understanding of the high hydrogen uptake observed in this novel composite.

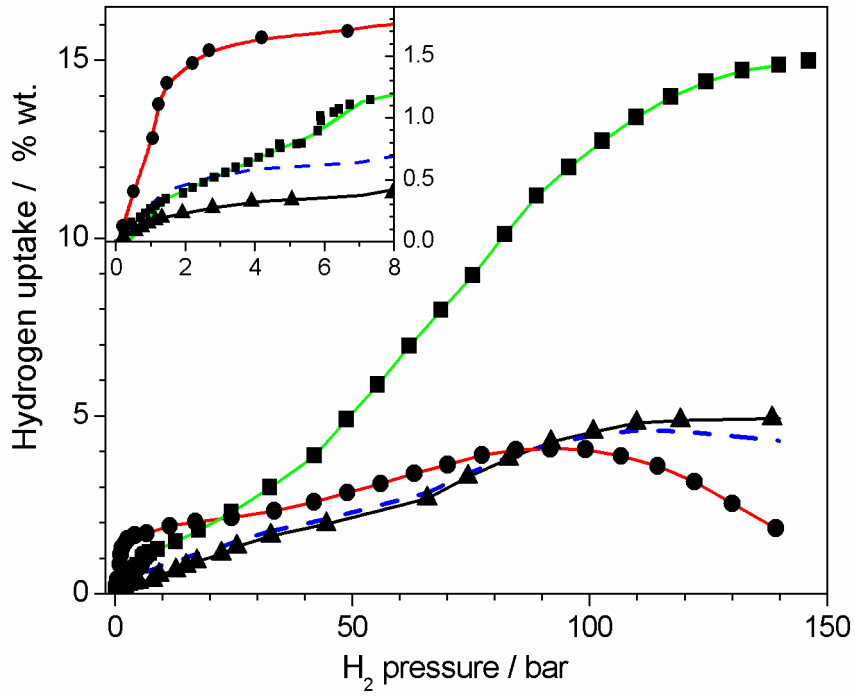

Figure 5.8: Isotherms of hydrogen adsorption at 77K into the pores of Cd_3Fe^{III}/TiNTs composite (■), bulk Cd_3Fe^{III} (●) and neat TiNTs (▲). The dashed line is simulated isotherm of hydrogen adsorption on hypothetical mixture of 10 wt. % of Cd_3Fe^{III} with 90 wt. % of TiNTs obtained by superposition of the isotherms for pure compounds.

As shown Figure 5.9, an increase in the temperature results in a decrease in the level of hydrogen uptake by the Cd_3Fe^{III}/TiNTs composite, without significant alteration of the two-step shape of the adsorption isotherm.

5.2.3 Enthalpy of adsorption

The apparent isosteric enthalpy of adsorption of hydrogen into the pores of the composite, ΔH_{ads} can be estimated from the data for different surface coverages using Van't Hoff's equation:

$$\left(\frac{\partial(\ln P)}{\partial(1/T)}\right)_{\theta} = \frac{\Delta H_{ads}}{R} \qquad (5\text{-}4)$$

in which P is the pressure of hydrogen, T is the temperature, R is the molar gas constant, and θ is the surface coverage. From the isotherms of adsorption onto the Cd^3Fe^{III}/TiNT

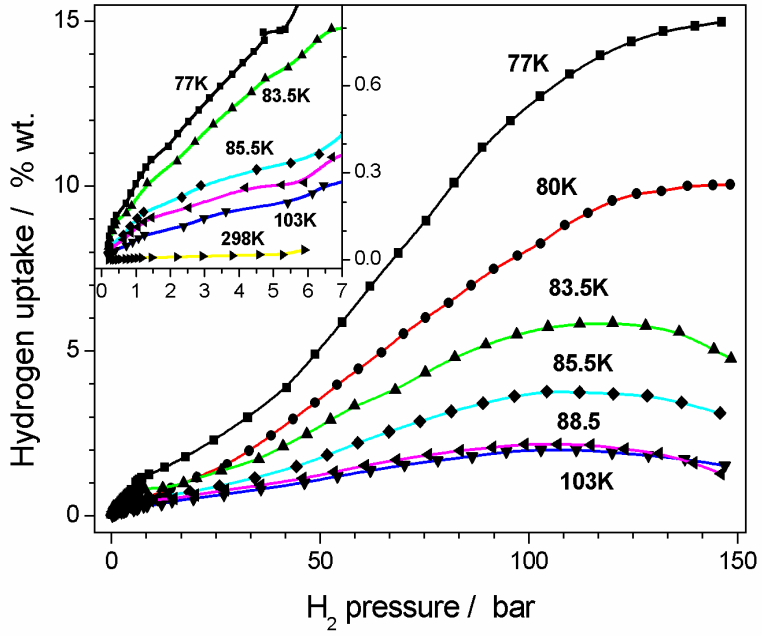

Figure 5.9: Isotherms of hydrogen adsorption onto the pores of nanostructured Cd_3Fe^{III}/TiNTs composite at selected temperatures.

composite at various temperatures (Figure 5.9) for two selected values of hydrogen uptake (0.3 wt. % and 3 wt. %) the logarithm of hydrogen pressure is plotted against 1/*T* in Figure 5.10. The slope of the lines multiplied by the universal gas constant is equal to the isosteric heat of adsorption. The calculations suggest values of –8.14 ± 2.3 kJ mol^{-1} and –5.14 ± 0.9 kJ mol^{-1} for 0.3 wt. % and 3 wt. % hydrogen uptake, respectively. These values are higher than that for bulk cadmium hexacyanoferrate (III) (–2.1kJ mol^{-1} at 0.3 wt. % hydrogen uptake) [4], indicating a modification in the nature of the hydrogen adsorption centres in the composite.

5.3 Hydrogen adsorption properties of $M_3[Fe(CN)_6]_2$/TiNT composites

The selection of Cd as the outer metal in the PB analogue used to form the composite with TiNTs was motivated by the results of H_2 adsorption experiments on a series of bulk PB analogues (M = Cu, Co, Cd, Mn, Zn, Ni, Fe) showing that $Cd_3[Fe(CN)_6]_2$ exhibits the highest adsorption capacity [8] at 1 bar. In order to confirm the selection, a series of samples was prepared with M = Cu, Co, Cd, Mn, Zn, Ni, Fe following the

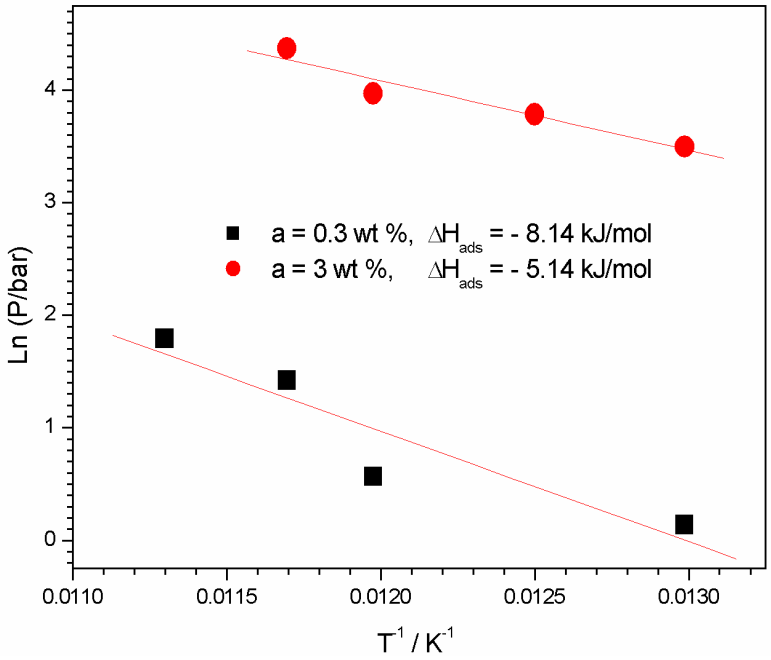

Figure 5.10: The pressure of hydrogen as a function of temperature for two values of hydrogen uptake in the Cd_3Fe^{III}/TiNTs composite.

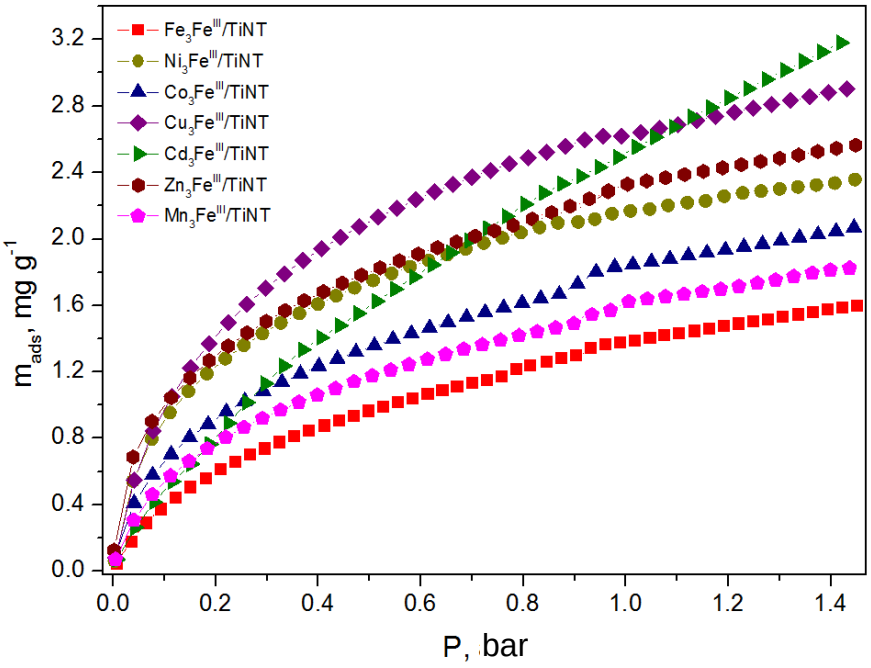

Figure 5.11: Comparative hydrogen adsorption isotherms at 77 K for the family of $M_3[Fe(CN)_6]_2$/TiNT composite (M refers to the transition metal of (a) Fe, (b) Ni, (c) Co, (d) Cu, (e) Cd, (f) Zn, (g) Mn).

synthesis procedure described in section 3.1.6. The results of H_2 adsorption experiments on the resulting composites are depicted in Figure 5.11. Clearly, the highest capacity at pressures over 1.5 bar (also see Table 5.1) is attained by the Cd_3Fe^{III}/TiNT composite.

The morphologies of the composite materials were investigated using N_2 adsorption. The BET surface areas (SSA_{BET}) are comparable across all samples (with Cd_3Fe^{III}/TiNT exhibiting one of the largest values) but there is more variation in the cumulative pore volume (CPV), with Cd_3Fe^{III}/TiNT attaining a value that is around 28 % higher than the next highest value (for Zn_3Fe^{III}/TiNT). The enthalpies of adsorption of the composite sample, ΔH_{ads}, were estimated from the H_2 equilibrium adsorption at 77 K and 87 K using a variant of the Clausius-Clapeyron equation (equation 5-5) combined with the Langmuir-Freundlich (L-F) isotherm model (full details of the procedure will be provided in section 7.3.3).

$$\Delta H_{ads} = R\left(\frac{T_2 - T_1}{T_1 T_2}\right)\ln\left(\frac{P_1}{P_2}\right) \tag{5-5}$$

An example of the fit to the data is shown in Figure 5.12 for the Fe_3Fe^{III}/TiNT and Cd_3Fe^{III}/TiNT samples, clearly showing that the L-F model provides the best fit of three standard models across the range of pressure and the two temperatures. The Cd_3Fe^{III}/TiNT composite exhibits the highest value of ΔH_{ads}, approximately 31 % higher than the next highest value (for Cu_3Fe^{III}/TiNT) and approximately 96 % higher than the lowest value (for Fe_3Fe^{III}/TiNT). Overall, therefore, the Cd_3Fe^{III}/TiNT composite possesses superior properties for H_2 adsorption compared to the other broad range of M_3Fe^{III}/TiNT composites tested.

In the next chapter, the kinetic adsorption properties of the Cd_3Fe^{III}/TiNT composite and are investigated. In Chapter 7, the effects of pH on the synthesis route (with respect to gas adsorption) are studied, and a detailed characterisation of the sample is performed.

Table 5.1: Structural and adsorptive properties of M_3Fe^{III}/TiNT composites.

Sample	M_3Fe^{III} wt. %	SSA_{BET}[1] ($m^2\ g^{-1}$)	CVP[2] ($cm^3\ g^{-1}$)	H_2 uptake 1.5 bar, 77 K ($mg\ g^{-1}$)	ΔH_{ads} (kJ/mol) 1 mg g^{-1}
Fe_3Fe^{III}/TiNT	19.58	227	0.406	1.60	–3.40
Ni_3Fe^{III}/TiNT	6.55	243	0.446	2.36	–3.80
Co_3Fe^{III}/TiNT	8.66	208	0.515	2.07	–4.03
Cu_3Fe^{III}/TiNT	12.67	245	0.421	2.90	–5.07
Cd_3Fe^{III}/TiNT	11.30	244	0.670	3.19	–6.66
Zn_3Fe^{III}/TiNT	16.74	218	0.524	2.57	–4.00
Mn_3Fe^{III}/TiNT	5.77	227	0.502	1.83	–4.41

[1] SSA = Specific Surface Area
[2] CPV = Cumulative Pore Volume

(a)

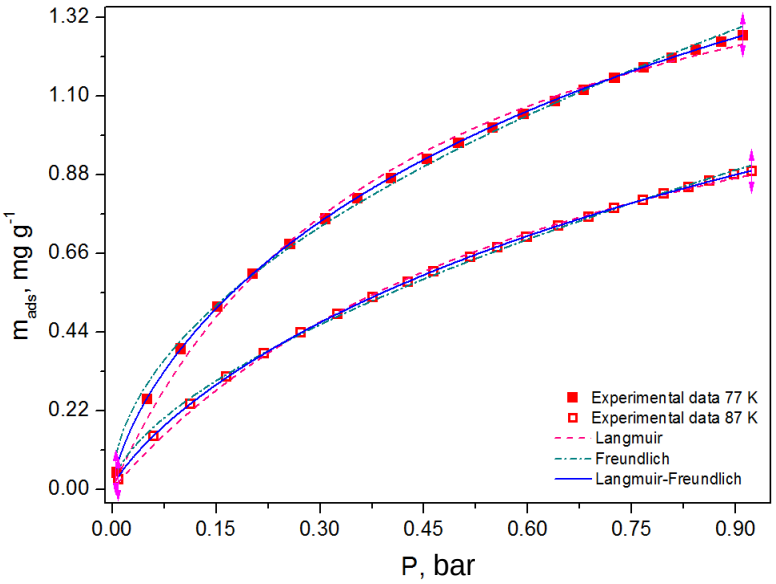

(b)

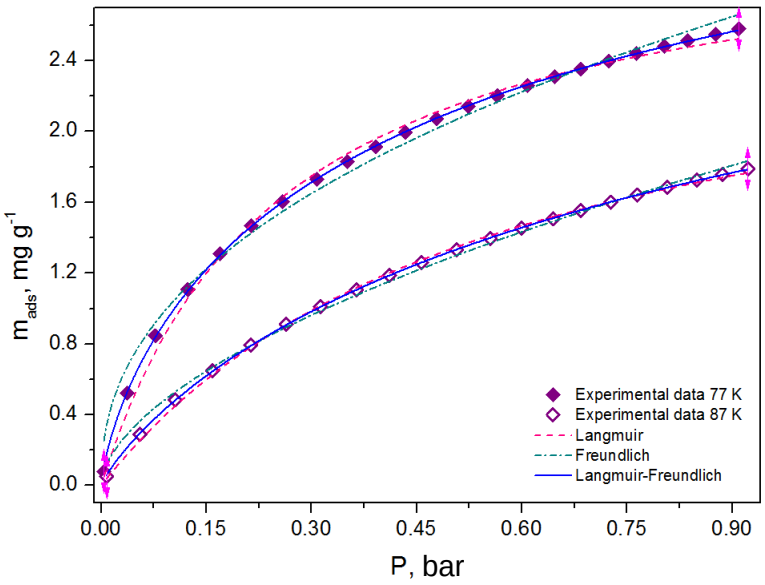

Figure 5.12: A fit of hydrogen equilibrium adsorption data at 77 K and 87 K for (a) $Fe_3[Fe(CN)_6]_2$/TiNT and (b) $Cd_3[Fe(CN)_6]_2$/TiNT to three model isotherms.

References

[1] Bavykin D.V., Lapkin A.A., Plucinski P.K., Friedrich J.M., Walsh F.C., J. Phys. Chem B 109 (2005) 19422–19427.

[2] Qamar M., Kim S.J., Ganguli A.K., Nanotechnology 20 (2009) 455703–455708.

[3] Chen J., Li S-L., Tao Z.L., Shen Y.T., Cui C-X., J. Am. Chem. Soc. 125 (2003) 5284–5285.

[4] Krap C.P., Balmaseda J., Zamora B., Reguera E., Int. J. Hydrogen Energy 35 (2010) 10381–10386.

[5] Hodos M., Horvath E., Kukovecz A., Konya Z., Kiricsi I., Chem. Phys. Lett. 399 (2004) 512–515.

[6] Shakti N., Gupta P.S., Appl. Phys. Res. 2 (2010) 18–26.

[7] Balmaseda J., Reguera E., Rodríguez-Hernández J., Reguera L., Autie M., Micro. Meso. Mater. 96 (2006) 222-236.

[8] Nakamoto K. Infrared and Raman spectra of inorganic and coordination compounds. Academic Press, 2000.

[9] Bavykin D.V., Parmon V.N., Lapkin A.A., Walsh F.C., J. Mater Chem. 14 (2004) 3370–3377.

[10] Murray L.J., Dinca M., Long J.R., Chem. Soc. Rev. 38 (2009) 1294–1314.

[11] Reguera E.**,** Int. J. Hydrogen Energy 34 (2009) 9163–9167.

[12] Krap C.P., Balmaseda, J., del Castillo L.F., Zamora B., Reguera E., Energy Fuels 24 (2010) 581–589.

[13] Reguera L., Krap C.P., Balmaseda J., Reguera E., J. Phys. Chem. C 112 (2008) 15893–15899.

[14] Reguera L., Roque J., Hernandez J., Reguera E., Int. J. Hydrogen Energy 35 (2010) 12864–12869.

Chapter 6: Kinetic and thermodynamic studies of hydrogen adsorption on TiNTs decorated with nanostructured Cd_3Fe^{III}

6.1 Introduction

Hydrogen adsorption/desorption kinetics are as important as the equilibrium adsorption behaviour since the time required for re-fuelling and discharging in dynamic applications, e.g., automotive fuel cell stacks, is restricted. Furthermore, kinetic data is required for selecting optimum operating conditions for the design and modelling of full-scale process [1-3]. Despite its undoubted importance, the kinetic behaviour of most hydrogen storage materials is rarely studied. Other important criteria for assessing the feasibility of a material for hydrogen storage relate to the thermodynamic properties of adsorption. The enthalpy, for example, provides valuable information on the adsorption process mechanism and the energetic and structural heterogeneity of the adsorbents.

In this chapter, the kinetics of hydrogen uptake in the Cd_3Fe^{III} / TiNT composite are studied (up to 135 bar and at different temperatures) in order to determine the rate controlling step in the adsorption process and to confirm the high uptake values observed in equilibrium adsorption measurements. Values for the surface diffusion coefficient, the diffusion time constant and the activation energy of diffusion are rigorously determined at different temperatures and pressures using the kinetic data. The apparent isosteric heat of adsorption, the Gibbs free energy change and the entropy change are calculated using the Clausius–Clapeyron equation in conjunction with the Dubinin–Astakhov (DA) isotherm, which is used for extracting parameters from equilibrium isotherm data.

6.2 Results and discussion

The adsorbed mass of hydrogen (mg g^{-1}), m_{ad}, at 77 K and 135 bar in each of the TiNT, Cd_3Fe^{III} and Cd_3Fe^{III}/TiNT composite samples is shown in Figure 6.1, as a function of time. There is an initial rapid adsorption for all samples, followed by a slower rate of approach towards an equilibrium value, m_e. In the first rapid stage, a high number of free adsorption sites are available and the molecules adsorb with ease. The rate slows as monolayer coverage is reached. The large value of the equilibrium (maximum) adsorbed amount for the composite confirms the previous equilibrium adsorption results [4]. Moreover, the time taken to reach 99 % of the equilibrium value is lowest for the composite material (under 100 s). It is not possible to compare this value with the small number of equivalent studies on other hydrogen storage materials such as MOF [1-3] since the pressure in the present case (135 bar) is much higher than the typical maximum of 1 bar used in most studies.

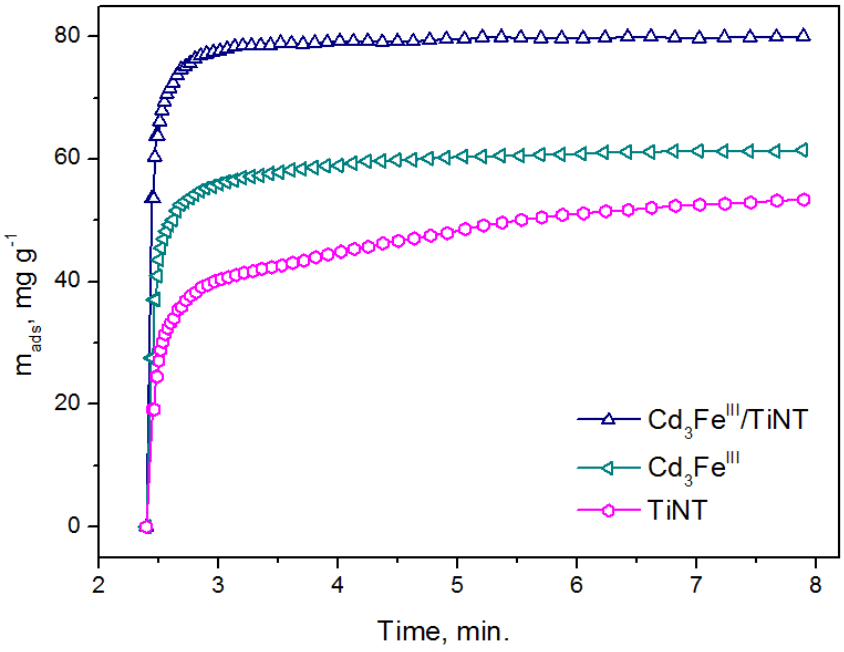

Figure 6.1: Hydrogen adsorption kinetic data for the TiNT, Cd_3Fe^{III} and Cd_3Fe^{III}/TiNT composite samples at 77 K and 135 bar.

Figure 6.2(a) shows m_{ad} as a function of time for the Cd_3Fe^{III}/TiNT composite material for an initial pressure of 100 bar at different temperatures, while Figure 6.2(b) is a plot

(a)

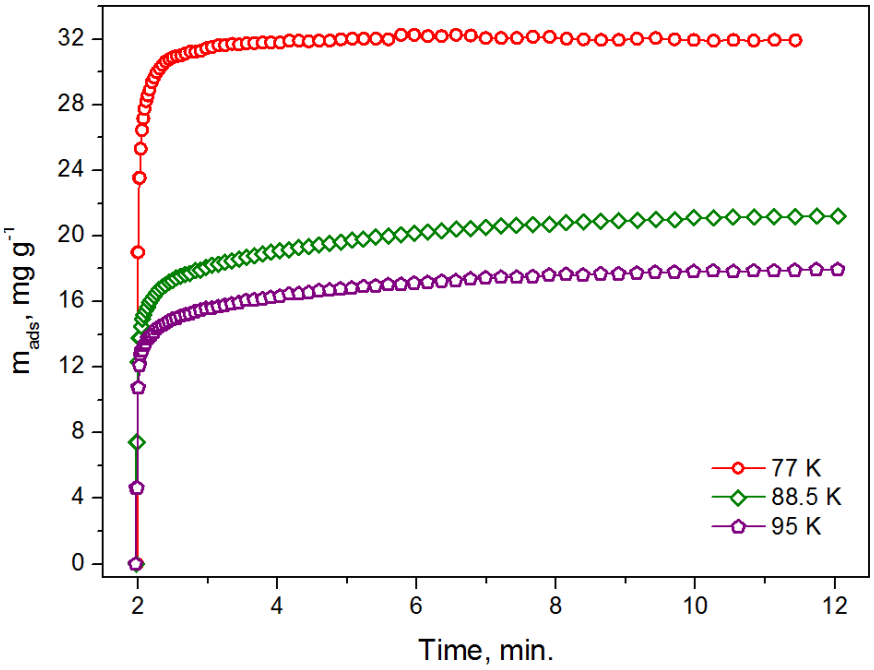

(b)

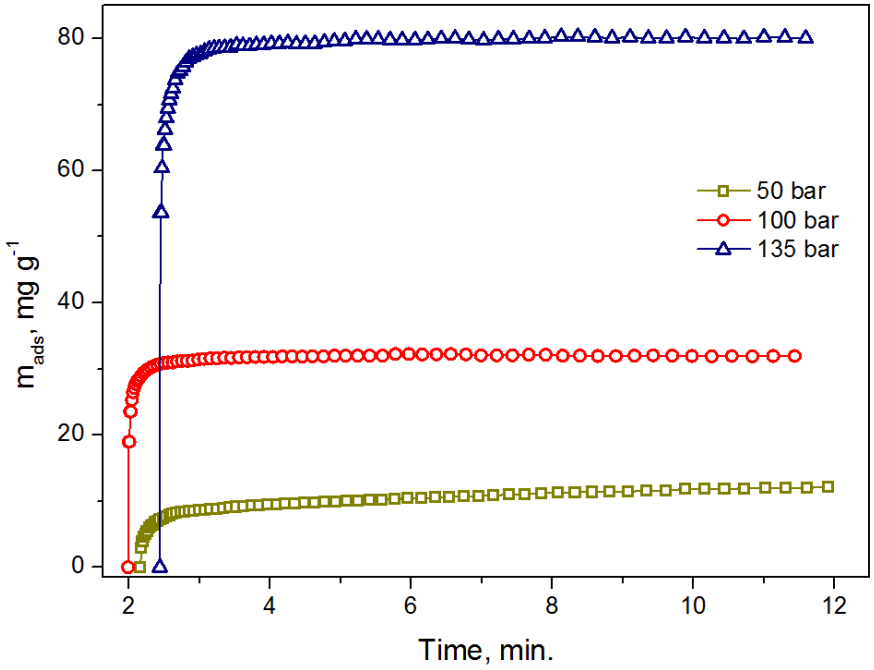

Figure 6.2: (a) Hydrogen adsorption kinetic data for the Cd_3Fe^{III}/TiNT composite at an initial pressure of 100 bar and three different temperatures. (b) Hydrogen adsorption kinetic data for the Cd_3Fe^{III}/TiNT composite at 77 K and three different initial pressures.

of m_{ad} for the Cd_3Fe^{III}/TiNT composite material for temperature of 77 K at three different initial pressures up to 135 bar. An increase in the temperature at a fixed initial pressure and an increase in the initial pressure at a fixed temperature result in a decrease in the maximum (equilibrium) level of hydrogen uptake, as would be expected. These results, along with those contained in Figure 6.1 will be used in the kinetic modelling study described below.

6.2.1 Adsorption kinetic models

In general sorption processes, the mass transfer of the sorbate to the sorbent particles and within the sorbent pores, comprises several steps, which directly affect the adsorption rate. Sorption models can be used to identify the rate-determining step. Kinetic sorption models generally fall into two categories: 'reaction' models and diffusion models. Adsorption 'reaction' models, which were first applied to chemical reaction kinetics, attempt to encapsulate the entire adsorption kinetic process in a single step. In adsorption diffusion models, on the other hand, the individual resistances are modelled as consecutive steps:

1. Transport of the sorbate from the bulk region to a *hypothetica*l exterior film or boundary layer surrounding the adsorbent particle.
2. Diffusion of the sorbate molecules across the external boundary layer to the external surface sites.
3. Migration of the sorbate molecules within the pores of the sorbent to free sites, which it termed 'intraparticle' diffusion.
4. Sorption of sorbate molecules at internal surface sites, termed 'mass action'.

In general, all of these processes are involved in the rate of adsorption but typically one or two steps are dominant. In the majority of systems, mass transport from the bulk solution to the external surface (step 1) and the adsorption surface sites (step 4) are (relatively) rapid processes; for hydrogen gas adsorption on a porous solid, step 1 is controlled by the rate of gas diffusion, which is a fast process in comparison to diffusion through a film or boundary layer, particularly at elevated pressures. Steps 2 and 3, on the other hand, are typically slow processes, and form the basis for most diffusion adsorption models. The relative importance of the diffusion components in porous

materials (steps 2 and 3) can be evaluated through the consecutive application of different kinetic sorption models.

6.2.2 Pseudo first and second order models

A number of reaction models have been developed to describe the uptake process/mechanism. Lagergren's pseudo first-order [5] (also called a linear driving force model [6]) and Ho's second-order [7] rate models have been applied extensively to sorption processes, from the sorption of pollutants [7], to gas adsorption in carbon nanotubes [8]. Similar models exist for applications in chemical reaction kinetics, but are distinguished from sorption models by the use of a concentration rather than an adsorption capacity. The adsorption process is controlled by a 'film' diffusion mechanism (a hypothetical boundary layer surrounding the sorbent particles) when the rate of adsorption changes linearly with concentration (or pressure) [9]. In order to determine whether this type of diffusion is the rate-controlling step in the hydrogen adsorption process in the Cd_3Fe^{III}/TiNT composite, the adsorption kinetic data was analysed with the aid of the pseudo first-order and second-order rate models.

The first-order rate expression of Lagergren [5] is given by:

$$\frac{dm_{ads}}{dt} = k_1(m_e - m_{ads}) \tag{6-1}$$

in which m_e is the amount of hydrogen adsorbed at equilibrium (mg g^{-1}); m_{ads} is the amount of hydrogen adsorbed at time t (mg g^{-1}); and k_1 is the equilibrium rate constant of pseudo-first order adsorption (s^{-1}). Integrating equation (6-1) subject to the initial condition that $m_{ads} = 0$ (no adsorption) at $t = 0$ yields the following:

$$\ln\left(1 - \frac{m_{ads}}{m_e}\right) = -k_1 t \tag{6-2}$$

A plot of $\ln(1 - m_{ads}/m_e)$ vs. t is linear if pseudo first-order kinetics are applicable, and k_1 and m_e can be determined from the slope and intercept of the plot, respectively.

The pseudo second-order equation [7] is expressed as follows:

$$\frac{dm_{ads}}{dt} = k_2(m_e - m_{ads})^2 \tag{6-3}$$

in which k_2 is the equilibrium rate constant (g mg^{-1} min^{-1}). The integrated form can be obtained from using the initial condition $m_{ads} = 0$ at $t = 0$:

$$\frac{1}{m_e - m_{ads}} = \frac{1}{m_e} + k_2 t \tag{6-4}$$

Equation (6-4) can be rearranged to obtain a linear form:

$$\frac{t}{m_{ads}} = \frac{1}{k_2 m_e^2} + \frac{t}{m_e} \tag{6-5}$$

A plot of t/m_{ads} versus t will yield a straight line with slope $1/m_e$ and intercept $1/k_2 m_e^2$ if the system obeys the pseudo second-order equation.

The kinetic data obtained for the TiNT, Cd_3Fe^{III} and the Cd_3Fe^{III}/ TiNT composite at 77 K and an initial pressure of 135 bar (see Figure 6.1) is plotted in Figures 6.3(a) and 6.3(b) in the form of the linearized equations (6-2) and (6-5) (i.e., the pseudo first-order and pseudo second-order laws), respectively. For all three samples, the fit to the pseudo first-order equation is clearly poor, whereas the fit to the pseudo second-order equation appears to be good. In order to confirm the fit to the pseudo second-order equation, the data for the Cd_3Fe^{III}/ TiNT composite at different temperatures and pressures (see Figure 6.2) was plotted in the form (6-5) and the result is shown in Figures 6.4(a) and 6.4(b). Again the fit appears to be good, at all temperatures and pressures. The pseudo-second-order rate constants were determined from Figure 6.4(b) by fitting straight lines to the data (least squares) and the values are presented in Table 6.1, together with the corresponding correlation coefficients. The rate constants are plotted against the initial pressure in Figure 6.5, clearly demonstrating that the relationship is not linear. It can be concluded, therefore, that film diffusion does not play a rate-controlling role in the adsorption process in the composite [9].

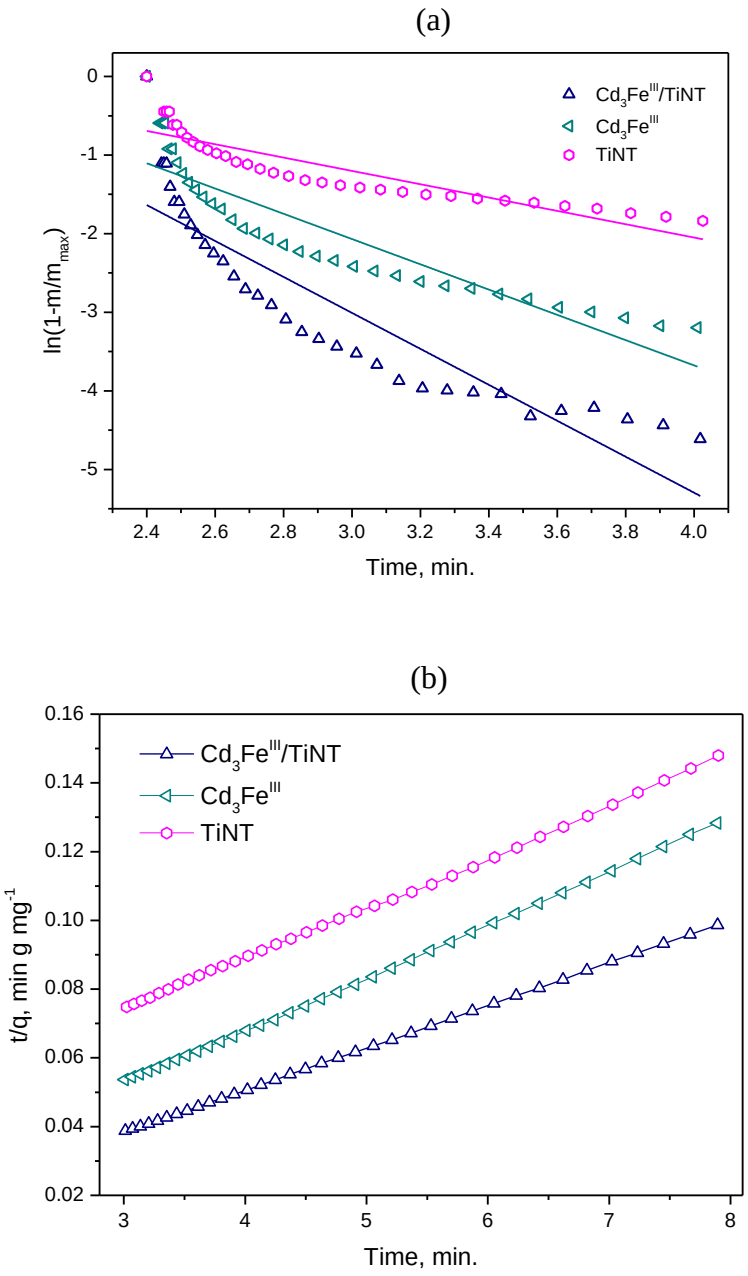

Figure 6.3: (a) A fit of the kinetic data for H_2 adsorption on TiNT, Cd_3Fe^{III} and Cd_3Fe^{III}/TiNT at 77 K and initial pressure of 135 bar to a pseudo first-order kinetic model. (b) A fit of the kinetic data for H_2 adsorption on TiNT, Cd_3Fe^{III} and Cd_3Fe^{III}/TiNT at 77 K and initial pressure of 135 bar to a pseudo second-order kinetic model.

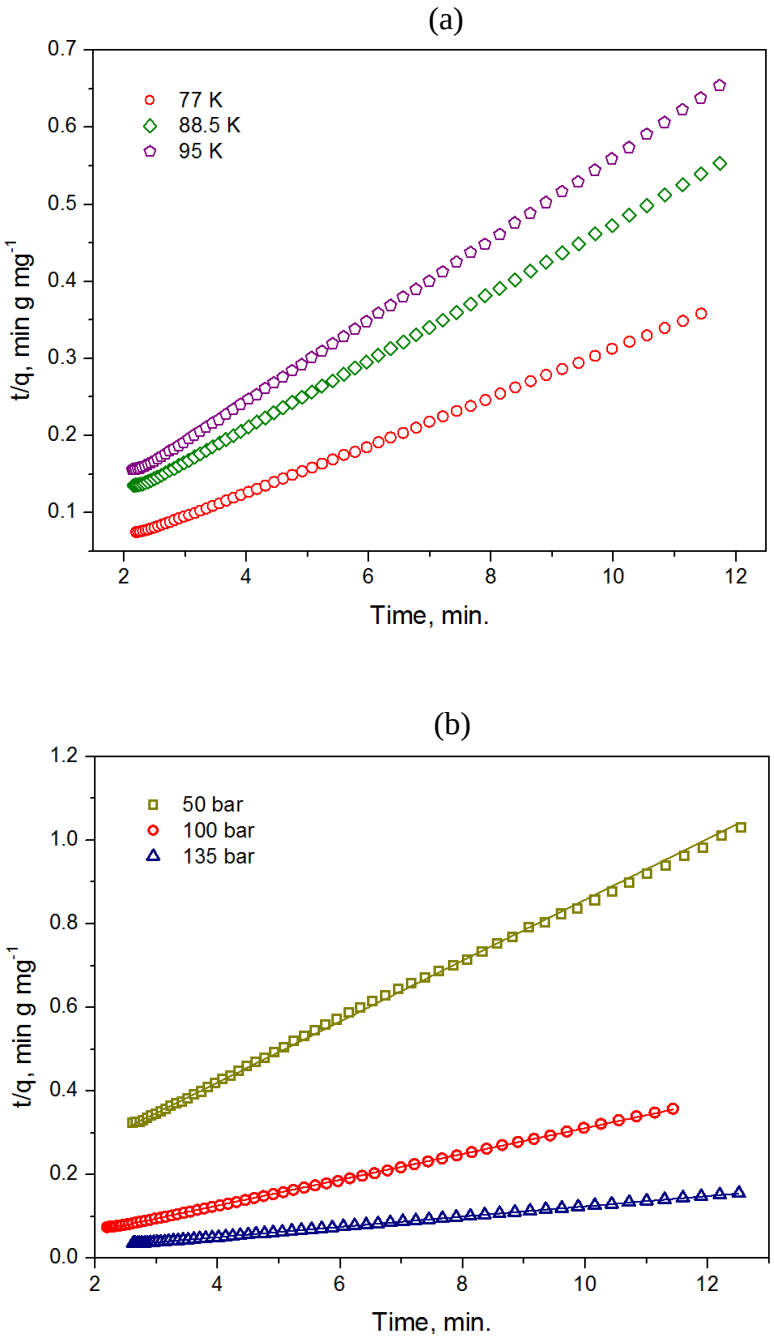

Figure 6.4: (a) A fit of the kinetic data for H_2 adsorption on the Cd_3Fe^{III}/TiNT composite at different temperatures and an initial pressure of 100 to a pseudo-second order kinetic model. (b) A fit of the kinetic data for H_2 adsorption on the Cd_3Fe^{III}/TiNT composite at 77 K and different initial pressures to a pseudo-second order kinetic model

Table 6.1: Second-order rate constants obtained for H_2 adsorption on the Cd_3Fe^{III}/TiNT composite at 77 K and initial pressures of 50,100 and 135 bar. The correlation coefficients (R^2) corresponding to the least-squares fit are also shown.

P **(bar)**	**Slope**	**Intercept**	$\mathbf{R^2}$	m_e **(mg g^{-1})**	k_2 **(g mg^{-1} min^{-1})**
50	0.07287	0.12926	0.99957	13.72	0.0411
100	0.03078	0.0038	0.99955	32.48	0.2493
135	0.01229	0.00184	0.99997	81.36	0.0821

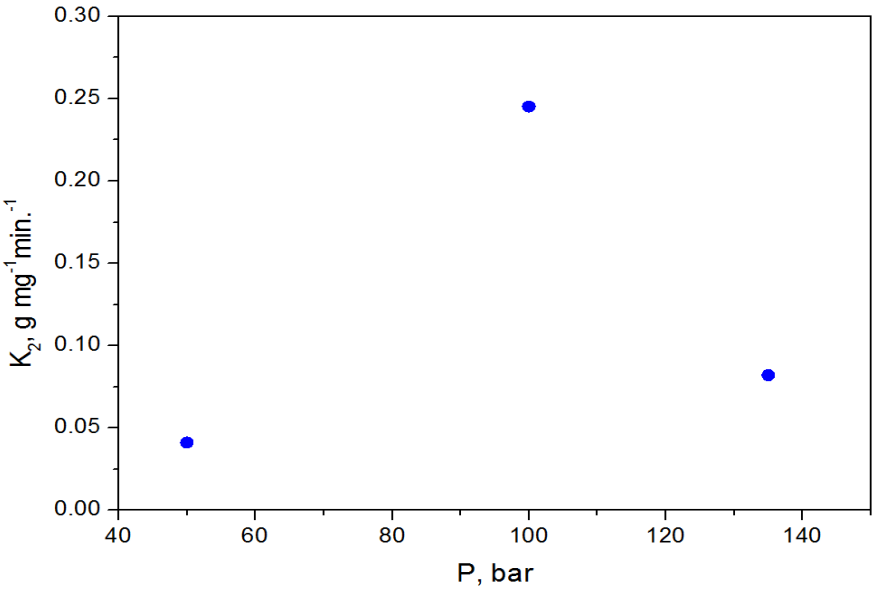

Figure 6.5: A plot of the second-order constant rate, k_2, vs. pressure for the adsorption of H_2 on the Cd_3Fe^{III}/TiNT composite at 77 K.

6.2.3 Intraparticle diffusion model

Consider the TiNTs as uni-axial cylinders with length *l*. Denote the diffusion coefficient of H_2 along the r (radial) axis as D_r and the diffusion coefficient in a direction z perpendicular to the r axis as D_z, both of which are assumed to be constant. Hence, the diffusion equation in standard cylindrical coordinates (r, θ, z) can be written as follows [10]:

$$\frac{dm_{ads}}{dt} = D_r \left[\frac{1}{r} \frac{\partial}{\partial r} \left(\frac{\partial m_{ads}}{\partial r} \right) + \frac{1}{r} \frac{\partial^2 m_{ads}}{\partial \theta^2} \right] + D_z \frac{\partial^2 m_{ads}}{\partial z^2} \tag{6-6}$$

Diffusion of hydrogen in solid materials has been studied extensively [11-13] and can be described as a hopping mechanism [14], in which a hydrogen molecule hops from one cage to an adjacent cage. For carbon and TiNTs, it is usually assumed that transport occurs mainly along the length (z axis) and that diffusion of the gas, in this case hydrogen, in the radial direction can be neglected. This assumption is supported by two facts. First, it was found [15] that the rate of hydrogen adsorption in carbon nanotubes could be increased by shortening the lengths of the tubes. Moreover, the crystal structure of single layers in a multilayered nanotube wall consists of densely packed TiO_6 octahedrons, which are less likely to be penetrated by hydrogen molecules than the slit channels along the tube [16]. With the assumption of dominating longitudinal diffusion (in the z direction) of the molecular hydrogen in cylindrical particles, equation (6-6) reduces to:

$$\frac{dm_{ads}}{dt} = D_z \frac{\partial^2 m_{ads}}{\partial z^2} \tag{6-7}$$

Following similar analyses for adsorption at a spherical particle [1-3, 17], the boundary and initial conditions are specified by considering a *step change* in the pressure (concentration) of hydrogen. The initial adsorbed concentration can be taken as zero, without any loss of generality. For $t > 0$, the adsorbed mass at the ends of the cylinder can be fixed at the equilibrium (maximum) value, m_e:

$$\begin{aligned} m_{ads}(0, z) &= 0 \\ m_{ads}(t, 0) &= m_e \\ m_{ads}(t, l) &= m_e \end{aligned} \tag{6-8}$$

Under the assumption of a constant diffusion coefficient, the solution of equation (6-7) at a given pressure is given by equation (4.16) in ref. [18], considering the terms containing odd values of n only (those containing even values are zero) :

$$\frac{m_{ads}}{m_e} = 1 - \sum_{n=0}^{\infty} \frac{4}{(2n+1)\pi} \exp\left(\frac{-\pi^2 (2n+1)^2 D_z}{l^2} t\right) \sin\left(\frac{(2n+1)\pi z}{l}\right) \tag{6-9}$$

The ratio m_{ads}/m_e is termed the fractional adsorption uptake. Equation (6-9) can be integrated to find the average value of m_{ads} over the length of the tube, defined as:

$$\bar{m}_{ads} = \frac{1}{l} \int_0^l m_{ads}\, dz \tag{6-10}$$

The integration yields:

$$\frac{\bar{m}_{ads}}{m_e} = 1 - \sum_{n=0}^{\infty} \frac{8}{\pi^2 (2n+1)^2} \exp\left(\frac{-\pi^2 (2n+1)^2 D_z}{l^2} t\right) \tag{6-11}$$

For fractional uptake values greater than 0.7, the following approximation of equation (6-11), obtained by neglecting the terms corresponding to $n \geq 1$, is valid:

$$1 - \frac{\bar{m}_{ads}}{m_e} \approx \frac{8}{\pi^2} \exp\left(\frac{-\pi^2 D_z t}{l^2}\right) \tag{6-12}$$

Equation (6-12) can be written as follows:

$$\ln\left(1 - \frac{\bar{m}_{ads}}{m_e}\right) \approx \ln\left(\frac{8}{\pi^2}\right) - \frac{\pi^2 D_z}{l^2} t \tag{6-13}$$

which is a more convenient form for comparison with the data and for extracting useful property values. A plot of $\ln\left(1 - m_{ads}/m_e\right)$ vs. t (m_{ads} is from the experimental data and is taken as the value for $\bar{m}_{ads}$) at different pressures yields a value for the hydrogen diffusion coefficient, D_z, from the slope $\pi^2 D_z / l^2$ of a least-squares fit. Only data

points with $0.7 < m_{ads}/m_e \leq 0.99$ were used in the fit [1-3]. The length of titanate nanotubes produced during alkali hydrothermal treatment usually exceeds several microns. For calculating the diffusion coefficient after obtaining the slope, a value of $l = 4\ \mu$m [16], estimated for TiNT prepared using the same hydrothermal synthesis route used in the present work, was used.

The adsorption kinetic data at different pressures (shown in Figure 6.2(b)) was plotted in the form of equation (6-13) and the cases corresponding to the highest and lowest pressure are shown in Figure 6.6. The range of time (shown in seconds for clarity) in Figure 6.6 is determined by the condition $0.7 < m_{ads}/m_e \leq 0.99$ since the model is not applicable outside this range. Similarly, the adsorption kinetic data at different temperatures (shown in Figure 6.2(a)) was plotted in the form (6-13) and the cases corresponding to the highest and lowest temperature are shown in Figure 6.7. It can be seen that the data approximates a straight line in all cases in Figures 6.6 and 6.7, suggesting that the diffusion model is a good approximation.

Estimation of the diffusion coefficients is summarised in Tables 6.2 (at different pressure) and 6.3 (at different temperature), which show the values of the slope, the diffusion coefficient and the correlation coefficient corresponding to a linear least-square fit. The high values of the correlation coefficient confirm that in all cases the data is well approximated by an equation of the form (6-13). Also shown in Tables 6.2 and 6.3 are the diffusion time constants, τ, defined below, for each of the (P,T) pairs:

$$\tau = \frac{l^2}{D_z} \tag{6-14}$$

The diffusion time constant is a measure of the time required for the diffusive flow to advance a distance equal to the characteristic length. It can be seen from Tables 6.2 and 6.3 that the diffusion time constant decreases with an increase in the pressure (at 77 K), and it decreases with an increase in the temperature at (100 bar). The decrease in the diffusion time constant with pressure at a given temperature is due to the reduction in the mean free path, $\lambda = 1/(\sqrt{2}(N/V)\pi d^2)$, where N/V is the number density of molecules and d is the diameter of the molecules. The decrease in the diffusion time

constant with temperature at a given pressure can be explained by the higher mean kinetic energy of the molecules.

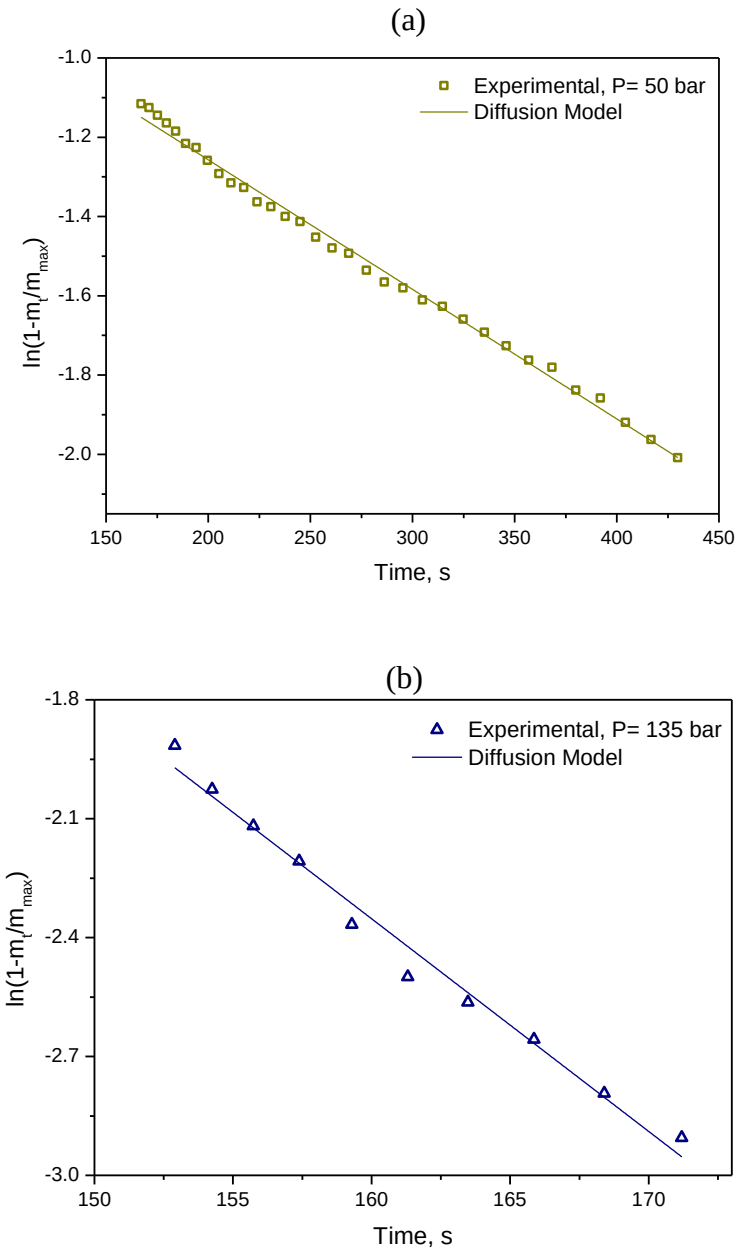

Figure 6.6: A fit of the kinetic data for H_2 adsorption on the Cd_3Fe^{III}/TiNT composite at 77 K and different initial pressure to the diffusion model solution given by equation (6-13).

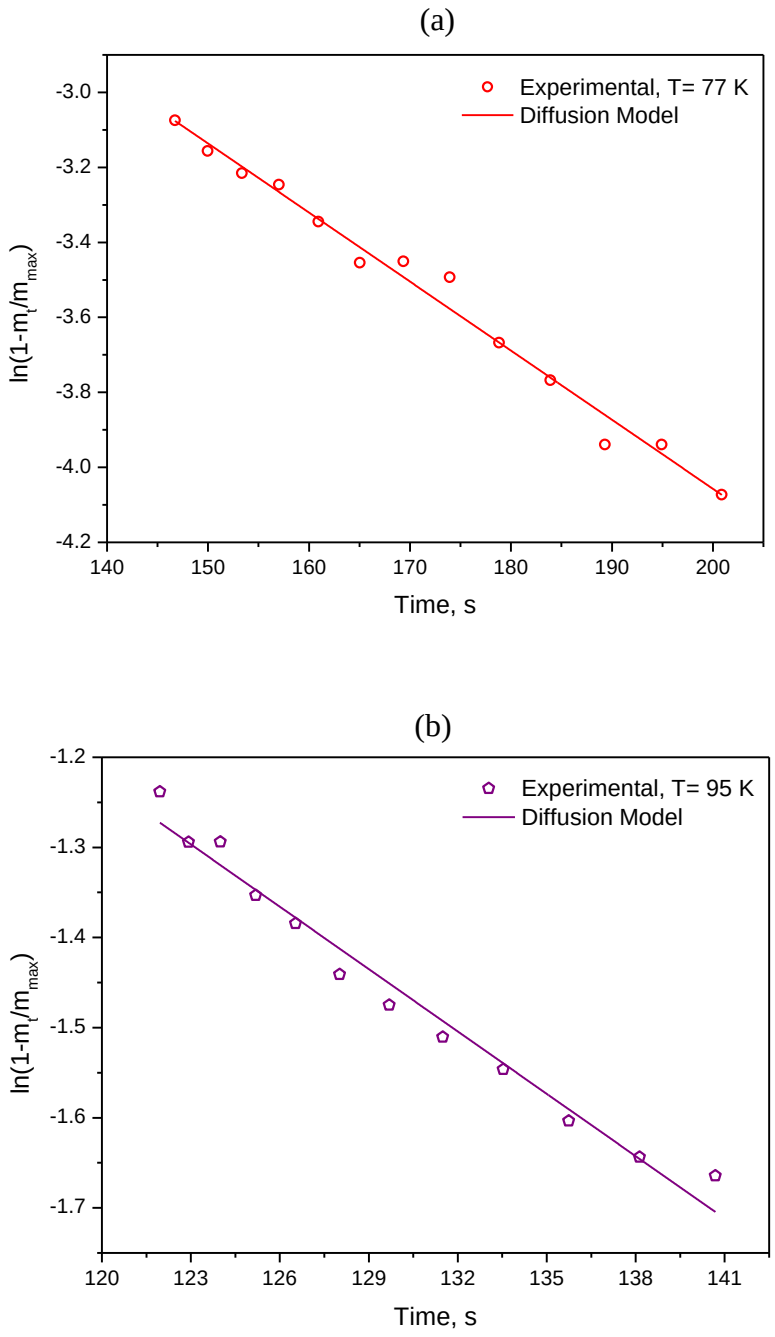

Figure 6.7: A fit of the kinetic data for H_2 adsorption on the Cd_3Fe^{III}/TiNT composite at different temperatures and initial pressure of 100 bar to the diffusion model solution given by equation (6-13).

Table 6.2: Diffusion coefficients and diffusion time constants for hydrogen adsorption on the Cd_3Fe^{III}/TiNT composite at a temperature of 77 K and different pressures, obtained using a least-squares fit with the correlation coefficients (R^2) shown.

P **(bar)**	**Slope,** $\pi^2 D_z / l^2$ **(s^{-1})**	$D_z \times 10^{10}$ **($cm^2\ s^{-1}$)**	$\tau = l^2 / D_z$ **(s)**	$\mathbf{R^2}$
50	–0.0033	0.53	3030	0.99444
100	–0.018	2.92	549	0.98410
135	–0.054	8.70	184	0.98296

Table 6.3: Diffusion coefficients and diffusion time constants for hydrogen adsorption on the Cd_3Fe^{III}/TiNT composite at a pressure of 100 bar and different temperatures, obtained using a least-squares fit with the correlation coefficients (R^2) shown.

T **(K)**	**Slope,** $\pi^2 D_z / l^2$ **(s^{-1})**	$D_z \times 10^{10}$ **($cm^2\ s^{-1}$)**	$\tau = l^2 / D_z$ **(s)**	$\mathbf{R^2}$
77.0	–0.018	2.92	549	0.98410
81.5	–0.019	3.15	507	0.98241
88.5	–0.021	3.40	469	0.98030
95.0	–0.023	3.73	429	0.97351

For H_2 at 50 bar and 95 K, the mean free path is around 1 nm (the largest across all conditions considered in this study), which is much shorter than the length scale l. It is, on the other hand, comparable to the distance between the layers of the multi-walled TiNTs (0.75 nm), although much shorter than the typical inner diameter (5-20 nm) [19]. Diffusion in the nanotubes is, therefore, a combination of molecular and Knudsen diffusion (taking into account tortuosity effects due to the presence of Cd_3Fe^{III} on the inner and outer surfaces of the TiNT), i.e., it is within the transition regime. The diffusion coefficients estimated from the data are effective values:

$$\frac{1}{D_z} \approx \frac{1}{D_m} + \frac{1}{D_K} \tag{6-15}$$

where D_m is the molecular coefficient and D_K is the Knudsen diffusion coefficient for the hydrogen gas. The Knudsen diffusion for a slit like pore (an approximation of the geometry of the space between layers in the nanotubes) can be estimated from [20]:

$$D_K = \frac{2h}{3}\sqrt{\frac{8RT}{\pi M}} \tag{6-16}$$

Here, h is the length of the slit-like pore or channel, M is the molecular mass of hydrogen and R is universal gas constant.

The diffusion coefficients increase with increasing pressure and increasing temperature, at fixed temperature and pressure, respectively. These trends are consistent with the trends in the diffusion time constant and can be explained as above. The Knudsen diffusion coefficient for hydrogen through the TiNT layers can be approximated from equation (6-16) as approximately 4.5×10^{-3} $cm^2\ s^{-1}$. This value, together with equation (6-15), suggest that Knudsen diffusion, although it is a contributor, is not the dominant mode of diffusive transport.

The equivalent analysis for the bulk Cd_3Fe^{III}, which can be approximated as spherical particles with an 'equivalent radius' R_p leads to the following expression for the average value of m_{ads}:

$$\frac{\bar{m}_{ads}}{m_e} = 1 - \sum_{n=1}^{\infty}\frac{6}{\pi^2 n^2}\exp\left(\frac{-\pi^2 n^2 D_r}{R_p^2}t\right) \tag{6-17}$$

Here, the average is defined as:

$$\bar{m}_{ad} = \frac{3}{R_p^3}\int_0^R r^2 m_{ads}\,dr \tag{6-18}$$

The boundary conditions used in this case correspond again to a step change in the hydrogen concentration at $t = 0$ and to symmetry at $r = 0$:

$$\begin{aligned} &m_{ads}(0, r) = 0 \\ &m_{ads}(t, R_p) = m_e \\ &\frac{\partial m_{ads}}{\partial r}(t, 0) = 0 \end{aligned} \tag{6-19}$$

The relevant approximation for fractional uptake values greater than 0.7 is:

$$1-\frac{\bar{m}_{ads}}{m_e} \approx \frac{6}{\pi^2}\exp\left(\frac{-\pi^2 D_r t}{R_p^2}\right) \tag{6-20}$$

in which D_r is the hydrogen diffusion coefficient in the radial direction r. The average equivalent radius was estimated from SEM images (see Figure 6.8) to be 700 nm. A least squares fit of the data for bulk Cd_3Fe^{III} (at 77 K and 135 bar) to the form (6-20) then yields a diffusion coefficient value of $D_r = 1.93\times10^{-11}$ cm^2 s^{-1} and a time constant value of $\tau = 254$ s. The time constant, which in this case is defined by $\tau = R^2/D_r$ is roughly 40 % higher than the value for the TiNT/Cd_3Fe^{III} composite, while the diffusion coefficient is approximately a factor of 40 lower. These results show that the mass transport resistance is significantly lower in the composite material, confirming that the deposition of the Cd_3Fe^{III} on the TiNT support leads to better mass transport characteristics.

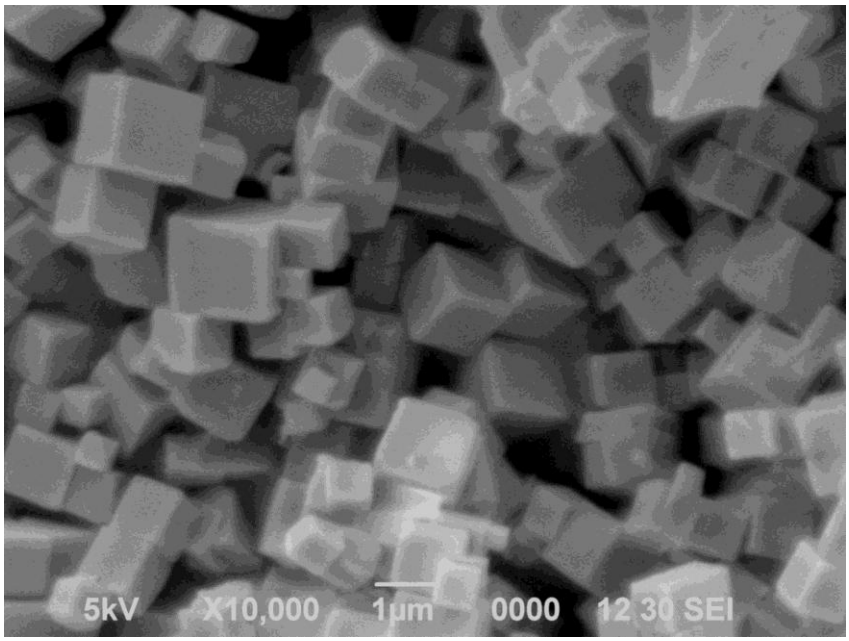

Figure 6.8: SEM image of bulk Cd_3Fe^{III}.

The temperature dependence of the diffusion can be approximated by using an Arrhenius equation form for the diffusion coefficient:

$$D_z = D_{z0}\exp\left(\frac{-E_a}{RT}\right) \tag{6-21}$$

in which D_{z0} is the pre-exponential factor and E_a is the activation energy for diffusion. A plot of $\ln(D_z)$ against T^{-1} yields a value for the activation energy. From the slope of the straight line fit in Figure 6.9, corresponding to data in Table 6.3, the activation energy for the composite was determined to be 0.817 kJ mol^{-1}.

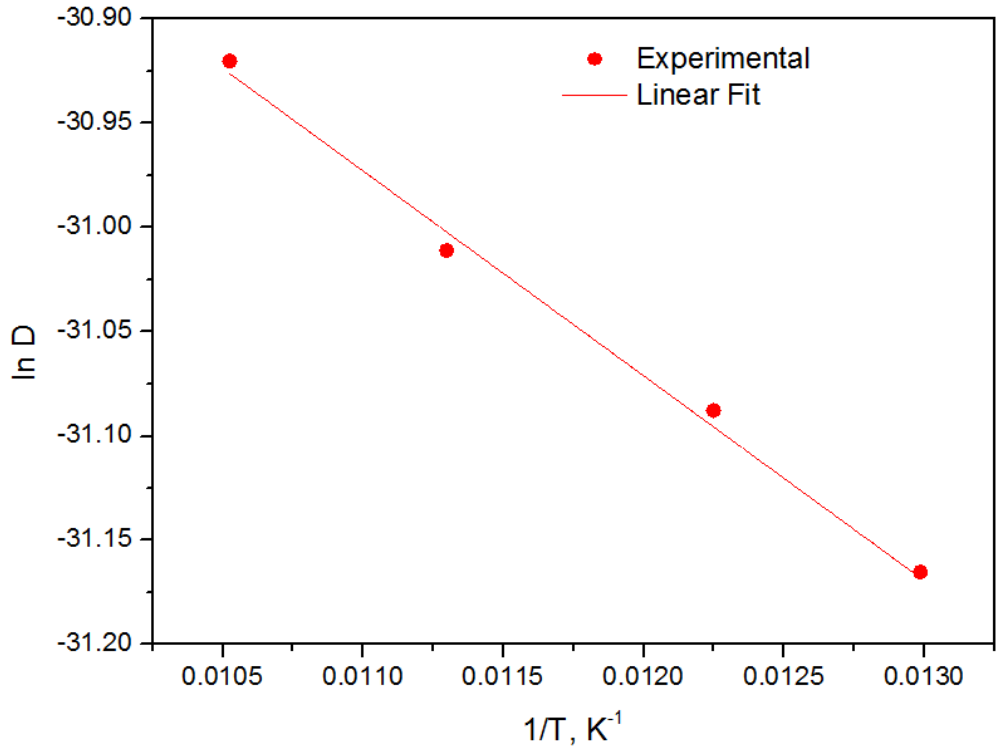

Figure 6.9: Arrhenius plot of the diffusion constants for hydrogen adsorption on the Cd_3Fe^{III}/TiNT composite.

6.2.4 Adsorption thermodynamics

Thermodynamic parameters, including the Gibbs free energy change, the enthalpy change and the entropy change, provide insights to the adsorption mechanisms are important for evaluating uptake of the adsorbents. The apparent isosteric enthalpy of adsorption into the pores of the adsorbent ΔH_{ads} can be calculated conveniently from the Clausius–Clapeyron equation with the assumption of a model isotherm. In this section, the isosteric enthalpy of adsorption of the hydrogen–Cd_3Fe^{III}/TiNT composite systems will be estimated using Dubinin–Astakhov (DA) model for adsorption. The DA isotherm equation (given below) was developed originally using the theory of volume filling of micropores and the Polanyi concept of desorption potential [21, 22]:

$$\theta = \frac{m_{ads}}{m_e} = \exp\left(-\left(\frac{RT}{E}\ln\left(\frac{P_s}{P}\right)\right)^{n_{DA}}\right) \tag{6-22}$$

In equation (6-22), θ is the surface coverage of hydrogen, P_s is a pseudo saturation vapour pressure, E is the characteristic energy and n_{DA} is a heterogeneity parameter. The pseudo saturation vapour pressure of hydrogen (under supercritical conditions) was estimated using the Dubinin approach [23]:

$$P_s = \left(\frac{T}{T_c}\right)^2 P_c \tag{6-23}$$

where P_c and T_c are the critical pressure and critical temperature of hydrogen, respectively. The equilibrium experimental data was fitted to equation (6-22) using nonlinear least-squares and the result is displayed in Figure 6.10. Also displayed in this

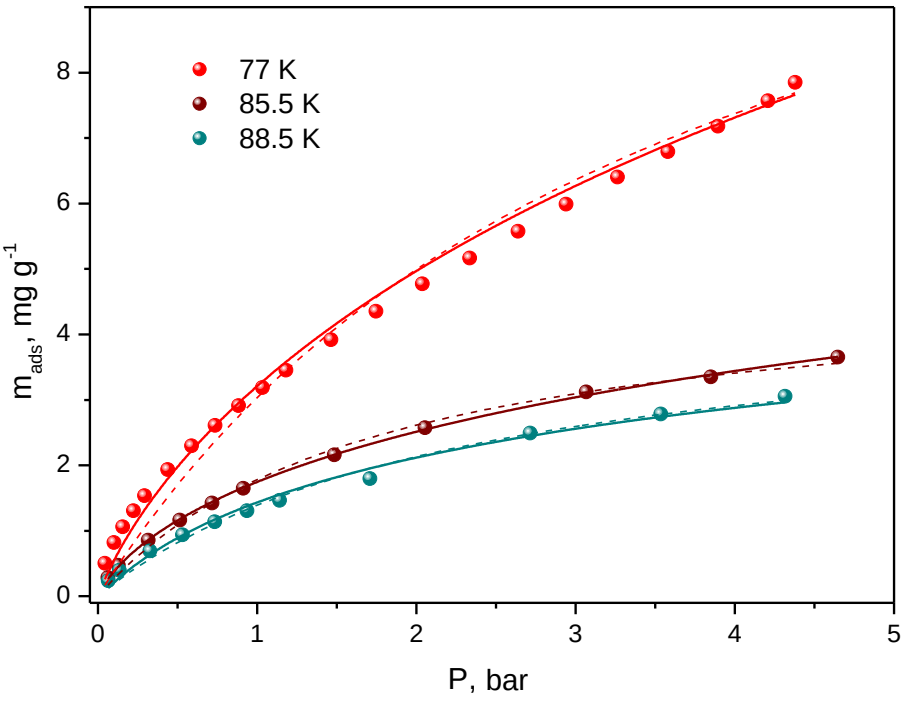

Figure 6.10: Experimental isotherms (shaded circles), Langmuir isotherm fits (dashed lines) and Dubinin–Astakhov isotherm fits (solid lines) for H_2 adsorption on the Cd_3Fe^{III}/TiNT composite at different temperatures.

figure is the fit to a Langmuir isotherm. This clearly shows that the DA model provides a better fit to the data. The fit was also superior to those using the Toth and Freundlich-Langmuir models, especially in the low surface coverage region. Table 6.4 shows the estimated parameter values obtained using the DA model.

Table 6.4: Adsorption parameters obtained by a nonlinear least squares fit of the Dubinin–Astakhov isotherm model to data for H_2 adsorption on the Cd_3Fe^{III}/TiNT composite at different temperatures. The corresponding correlation coefficients (R^2) are shown.

Parameter	77 K	81.5 K	85.5 K	95 K
m_e (mg g^{-1})	12.08	9.45	7.99	7.01
E (J mol^{-1})	2437	2445	2453	2500
n_{DA}	2.33	2.01	1.75	1.69
R^2	0.97935	0.98835	0.99455	0.99747

The differential Gibbs energy of adsorption, ΔG_{ads}, can be defined by:

$$\Delta G_{ads} = -RT \ln\left(\frac{P_s}{P}\right) \tag{6-24}$$

Combining equations (6-22) and (6-24) yields the following expression:

$$\Delta G_{ads} = -E\left(\ln\left(\frac{m_{ads}}{m_e}\right)\right)^{1/n_{DA}} \tag{6-25}$$

which can be used for estimating ΔG_{ads}. Plots of $\Delta G_{ads} = -E\left(\ln(\theta)\right)^{1/n_{DA}}$ vs. $\theta = m_{ads}/m_e$ from the experimental data at different temperatures are shown in Figure 6.11 for the composite material. The Gibb's free energy is negative, indicating that adsorption is a spontaneous process, as is well known. Figure 6.11 shows that $-\Delta G_{ads}$ decreases with increasing surface coverage. In other words, as a monolayer coverage is approached, the process becomes less spontaneous as a result of the decreasing number of free sites available for adsorption.

The data was then used to estimate values of ΔH_{ads} and the entropy change associated with adsorption of hydrogen on the composite material, ΔS_{ads}. Selecting a value of $m_{ads} = 0.3$ mg g^{-1}, the corresponding value of ΔG_{ads} was fitted to a straight line with temperature as the independent variable (shown in Figure 6.12). By virtue of the relationship $\Delta G_{ads} = \Delta H_{ads} - T\Delta S_{ads}$, the following values were obtained: $\Delta H_{ads} = -6.23$ kJ mol^{-1} and $\Delta S_{ads} = -45.15$ J mol^{-1} K^{-1}.

The relatively low value of ΔH_{ads} is characteristic of a physisorption process and is higher than that for bulk cadmium hexacyanoferrate (III) (2.1 kJ mol^{-1} at 0.3 wt. % hydrogen uptake) [24], and comparable to the values obtained for most metal organic frameworks (2–7 kJ mol^{-1}) [12,25]. Comparing the value of ΔH_{ads} with the previously estimated value of the activation energy for diffusion in the composite (0.817 kJ mol^{-1}), it can be seen that $\Delta H_{ads} \gg E_a$. Therefore, the diffusion process is spontaneous in comparison to the adsorption/desorption process, which implies that the rate-limiting step of the overall process of hydrogen adsorption onto the composite material is surface adsorption.

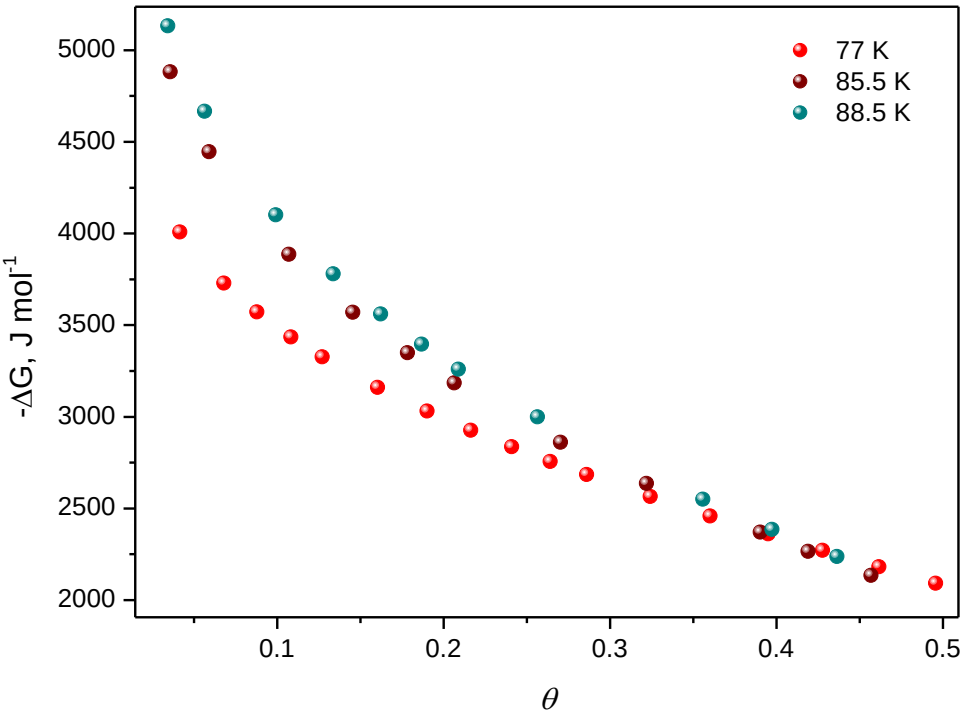

Figure 6.11: The effect of the adsorption uptake ratio on the Gibb's free energy of hydrogen adsorption, ΔG_{ads}, on the Cd_3Fe^{III}/TiNT composite.

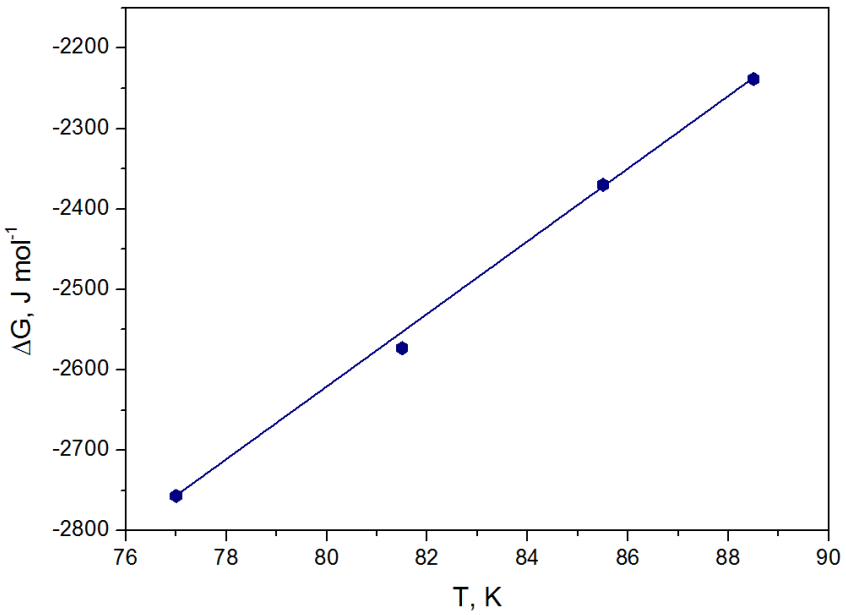

Figure 6.12: A plot of the Gibb's free energy change, ΔG_{ads}, versus temperature *T* for hydrogen adsorption on the Cd_3Fe^{III}/TiNT composite ($m_{ads} = 0.3$ mg g^{-1}).

References

[1] Saha D., Deng S., Int. J. Hydrogen Energy 34 (2009) 2670-2678.

[2] Saha D., Wei Z., Deng S., Int. J. Hydrogen Energy 33 (2008) 7479-7488.

[3] Saha D., Wei Z., Deng S., Separation and Purification Technology 64 (2009) 280-287.

[4] Al-Hajjaj A.A., Zamora B., Bavykin D.V., Shah A.A., Walsh F.C., Reguera E., Int. J. Hydrogen Energy 37 (2012) 318-326.

[5] Lagergren S., Kungliga Svenska Vetenskapsakademiens. Handlingar 24 (1898) 1-39.

[6] Fletcher A.J., Cussen E.J., Prior T.J., Rosseinsky M.J., Kepert C.J., Thomas K.M., J. Am. Chem. Soc. 123 (2001) 10001–10011.

[7] Ho Y.S., Mckay G., Process Biochem. 34 (1999) 451-465.

[8] Delavar M., Ghoreyshi A.A., Jahanshahi M., Khalili S., Nabian N., RSC Adv. 2 (2012) 4490-4497.

[9] Atun G., Sismanoglu T., J. Environ. Sci. Health A31 (1996) 2055-2069.

[10] Carslaw H.S., Jaeger J.C., *Conduction of Heat in Solids*. Second ed 1959, London: Oxford University Press.

[11] Krap C.P., Balmaseda J., Castillo L.F.d., Zamora B., Reguera E., Energy & Fuels 24 (2010) 581−589.

[12] Thomas K.M., Dalton Trans. (2009) 1487−1505.

[13] Düren T., Millange F., Férey G., J. Phys. Chem. C 111 (2007) 15350–15356.

[14] Kaye S.S., Long J.R., J. Am. Chem. Soc. 127 (2005) 6506−6507.

[15] Liu F., Zhang X., Cheng J., Tu J., Kong F., Huang W., Chen C., Carbon 41 (2003) 2527-2532.

[16] Bavykin D.V., Lapkin A.A., Plucinski P.K., Friedrich J.M., Walsh F.C., J. Phys. Chem. B 109 (2005) 19422-19427.

[17] Ruthven D.M., *Principles of Adsorption and Adsorption Processes* 1984, New York: John Wiley.

[18] Crank J., *The Mathematics of Diffusion*. Second ed 1975, London: Oxford University Press.

[19] Bavykin D.V., Walsh F.C., *Titanate and Titania Nanotubes: Synthesis, Properties and Applications*. First ed 2009, Cambridge, UK: Royal Society of Chemistry.

[20] Clark M.M., *Transport Modeling for Environmental Engineers and Scientists*. Second ed 2009, New Jersey: John Wiley.

[21] Bering B.P., Dubinin M.M., Serpinskii V.V., J. Coll. Int. Sci. 38 (1972) 185-194.

[22] Dubinin M.M., *Progress in membrane and surface science*, 1975, Academic Press: New York.

[23] Dubinin M.M., Chem. Rev. 60 (1960) 235-241.

[24] Reguera E., Int. J. Hydrogen Energy 34 (2009) 9163-9167.

[25] Murray L.J., Dinca M., Long J.R., Chem. Soc. Rev. 38 (2009) 1294-1314.

Chapter 7: Effect of the synthesis pH on hydrogen adsorption in TiNTs decorated with nanostructured Cd_3Fe^{III}

7.1 Introduction

Based on the favourable morphological and ion-exchange properties of titanate nanotubes [1,2], in Chapter 5 (see also [3]) a Cd_3Fe^{III}/TiNT composite was synthesized and evaluated as a hydrogen storage material, showing great promise. It was concluded that systematic studies were required in order to elucidate the nature of the interaction between hydrogen molecules and the surfaces of the Cd_3Fe^{III}/TiNT composite. In this chapter, changes were made to the pH during the second step (5-2) of the synthesis route and the morphologies and surface properties of the resulting composites were studied. A detailed analysis of the composites was performed using TEM, high resolution TEM, atomic force microscopy, energy-dispersive X-ray spectroscopy, elemental analysis, Fourier-transform infrared spectroscopy, X-ray diffraction analysis and X-ray photospectroscopy and thermogravimetric analysis. Nitrogen and hydrogen adsorption experiments were performed to further characterize the surface properties and to assess the H_2 uptake properties of the composites.

7.2 Sample Characterization

7.2.1 High resolution TEM

The second step (reaction of Cd^{2+} ions with the $[Fe(CN)_6]^{3-}$ complex) of the two-step deposition of cadmium ferricyanide (Cd_3Fe^{III}) on the surfaces of titanate nanotubes (TiNTs) described in Chapter 5 was modified by changing the chemical environment of the reaction, specifically through adjusting the initial pH of the environment. The reaction is rewritten below for convenience:

$$Cd_xH_{2(1-x)}Ti_3O_7(s) + \frac{2x}{3}K_3[Fe(CN)_6](aq) \rightarrow \left(Cd_3[Fe(CN)_6]_2\right)_{x/3} K_{2x}H_{2(1-x)}Ti_3O_7(s) \quad (5\text{-}2)$$

The initial pH during this step was adjusted to (separately) take values of 2, 4, 8 and 10 by adding 0.1 M HCl or 0.1 M KOH, which resulted in four different samples of the Cd_3Fe^{III}/TiNT composite. These samples were characterized, evaluated and compared with TiNT, Cd_3Fe^{III} and the original Cd_3Fe^{III}/TiNT composite material examined in Chapter 5 (neutral pH).

Figure 7.1 shows TEM images of the composite Cd_3Fe^{III}/TiNT material prepared with different initial pH values between 2 and 10. From Figure 7.1a it is possible to confirm that the TiNTs retained their tubular shape, with an average diameter of ca. 10 nm, in

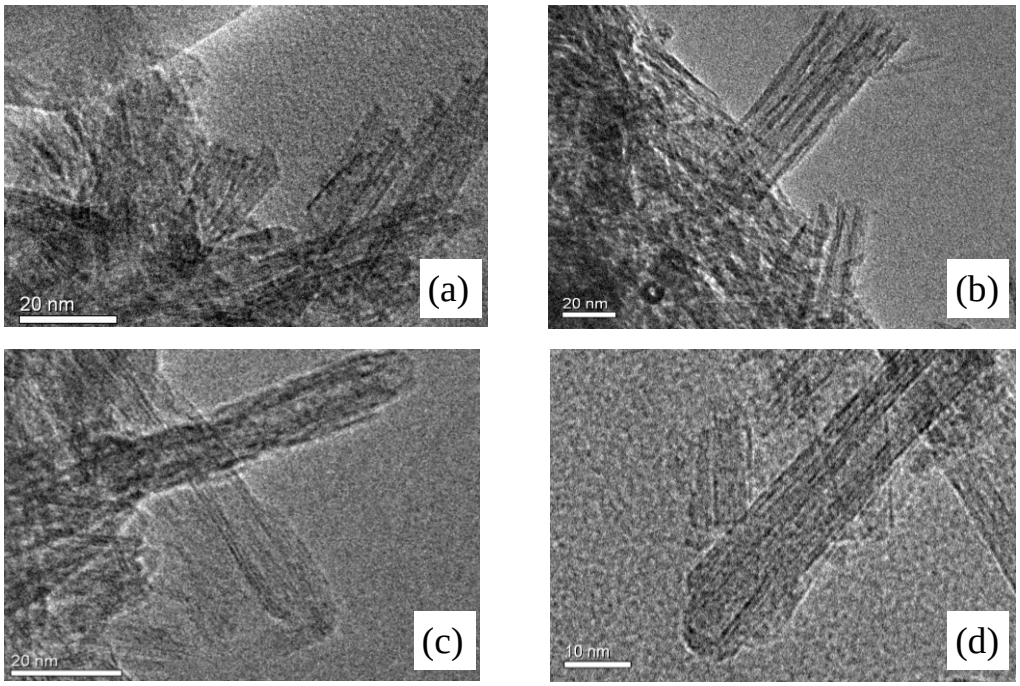

Figure 7.1: TEM images of the Cd_3Fe^{III}/TiNT composites prepared at an initial pH of (a) 2; (b) 4; (c) 8; (d) 10.

good agreement with previous observations [4]. These images also show an accumulation on the TiNT support but do not provide a clear indication of the nature of the accumulation or deposit on the TiNTs. High resolution TEM (HR-TEM) images were obtained for the same set of samples and are displayed in Figure 7.2. Figure 7.2

indicates that for each sample, Cd_3Fe^{III} particles are deposited on the outer as well as the inner surfaces of the TiNTs (see the case for pH=2). In Fig 7.2a, there is also evidence of the Cd_3Fe^{III} on the TiNT surface. The characteristic cubic shape and the perpendicular lattice fringes of a single Cd_3Fe^{III} nanoparticle are clearly visible, as was also observed by Ivekovic *et al.* after depositing Fe_3Fe^{III} (Prussian blue) on TiNTs [5].

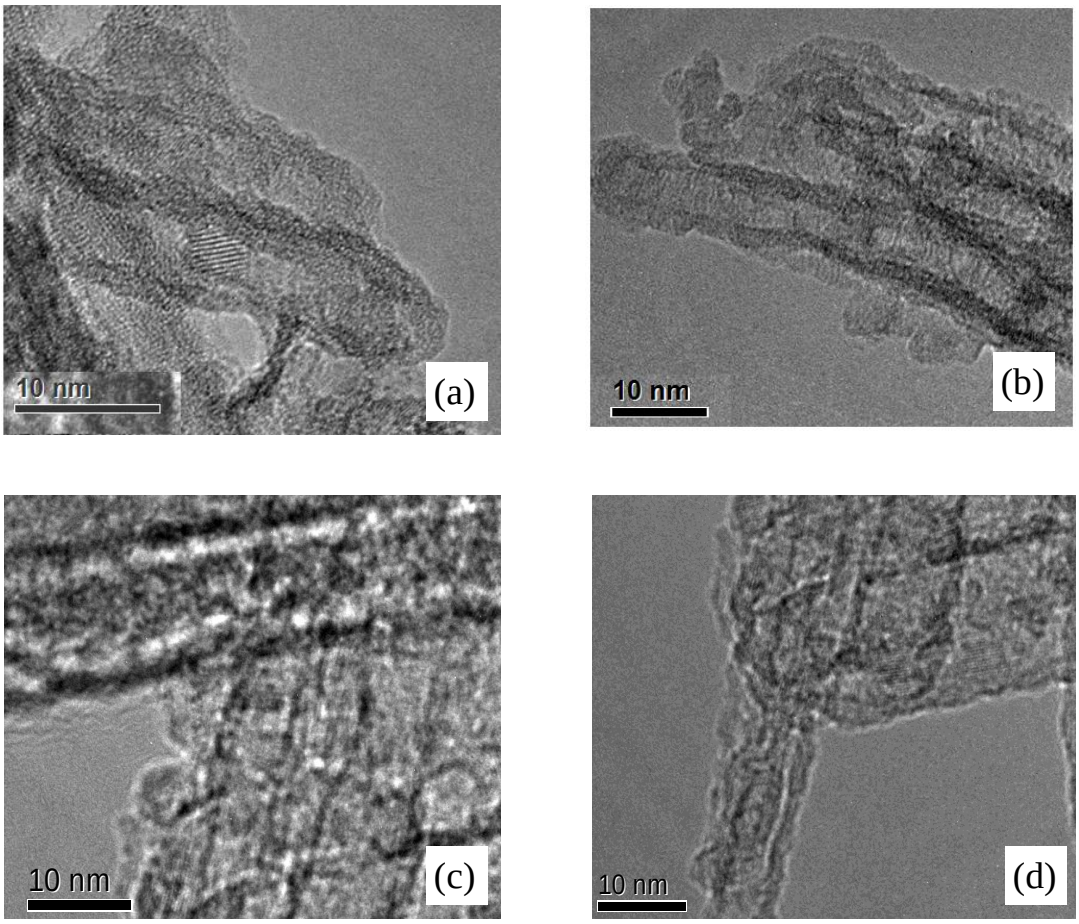

Figure 7.2: HR-TEM images of the Cd_3Fe^{III}/TiNT composites prepared at an initial pH of (a) 2; (b) 4; (c) 8; (d) 10.

7.2.2 Fourier transform infrared spectroscopy

The results of Fourier-transform infrared (FTIR) studies of the composites at different pH values and of bulk Cd_3Fe^{III} are depicted in Figure 7.3. The presence of bands within a range of wavenumbers that are characteristic to the vibrations of CN groups (2151 to 2154 cm^{-1}) validates the formation of cadmium ferricyanide in all composites; the

composite sample and bulk Cd_3Fe^{III} results are characterised by the presence of a band around 2154 cm^{-1}, which can be attributed to the stretching vibrations of the cyanide group Fe–C≡N–Cd chains [6]. A second band in the spectra for the composite samples appears at around 2062–2064 cm^{-1}, and this can be attributed to Fe^{2+} impurities, arising from the reduction of the inner metal (iron) Fe^{3+}. The wavenumbers associated with the stretching vibrations of the cyanide groups in the composite samples are slightly shifted to lower energies as the pH is increased. This is related to the 5σ orbitals of the CN groups, which have a certain anti-bonding character. The Cd_3Fe^{III} formation is always related to a reinforcement of the C≡N triple bond, which raises the ν(CN) frequency [7,8].

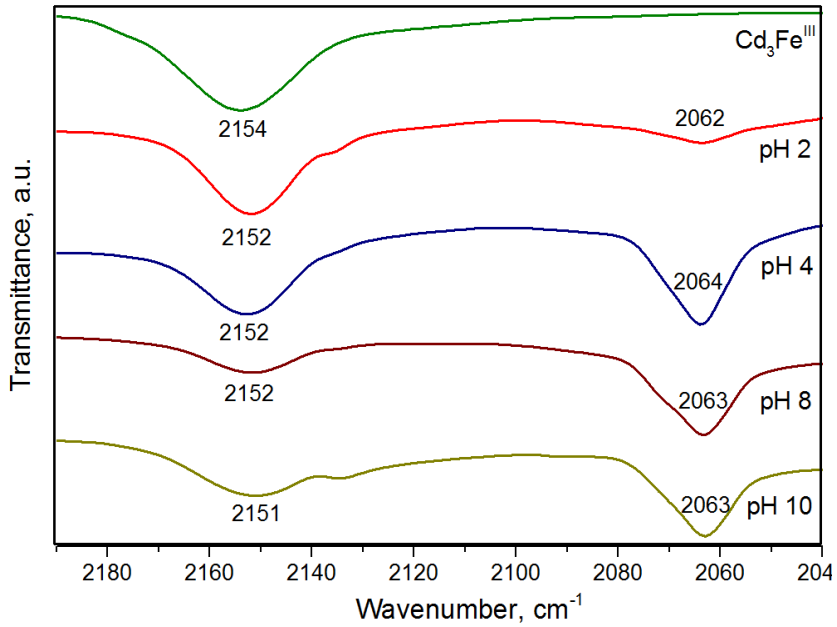

Figure 7.3: FT-IR spectra of Cd_3Fe^{III} and the Cd_3Fe^{III}/TiNT composites prepared at different initial pH.

7.2.3 X-ray photospectroscopy

XPS is used widely for studying the electronic states of materials, as well as for quantitative surface analysis. The XPS survey spectra of the Cd_3Fe^{III}/TiNT composites prepared at different pH are shown in Figure 7.4. The presence of an individual element in the composites is indicated by a label at the corresponding binding energy. The doublet at 458.5/464.2 eV corresponds to the Ti 2*p* orbital. The two binding energy values represent the states Ti $2p_{3/2}$ and Ti $2p_{1/2}$, respectively, which are formed as a

result of spin-orbit coupling; according to the angular momentum number for the *p* orbital ($l = 1$) and the possible spin states ($s = \pm 1/2$), leading to a total angular momentum of 1/2 (lower binding energy) and 3/2 (higher binding energy, which corresponds to the least favoured state). It can be confirmed that the Ti at the surface exists in the form Ti^{4+}. The binding energy of O 1*s* is 530.3 eV, related to an oxidation state of –2. The binding energy of C 1*s* is approximately 285 eV for all samples. The intensity of all elemental peaks (which is proportional to the quantity of the corresponding element) increases in the following order: pH2>pH10>pH4>pH8.

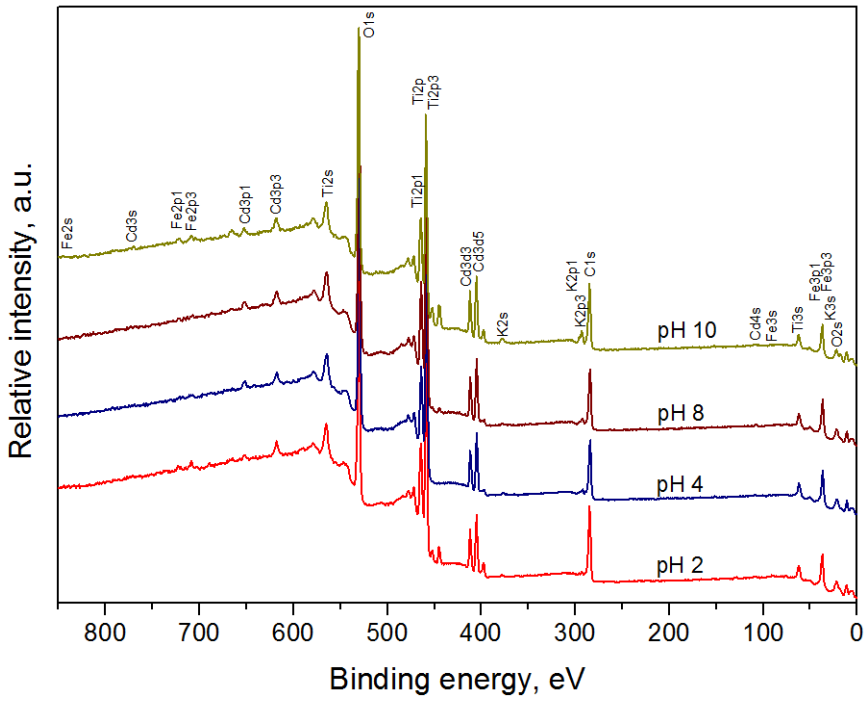

Figure 7.4: XPS survey spectra of the Cd_3Fe^{III}/TiNT composites prepared at different initial pH.

The K $2p_{3/2}$ and K $2p_{1/2}$ doublet is clearly visible in the interval 305–287 eV, corresponding to the K^+ cations required for charge balance after deposition of the Prussian blue analogue on the TiNT surfaces (discussed in Chapter 5). Figure 7.5 shows a region centered at the binding energy of Cd 3*d* (405.0 eV) for all samples. A doublet corresponding to Cd $3d_{3/2}$ (411.7 eV) and Cd $3d_{5/2}$ (404.5 eV) appears in the spectra for all samples (the spectra are given by the dotted lines). Also shown on these plots are the decompositions of the spectra using Gaussian basis functions. In each case, the spectrum is well approximated by the sum of contributions from CdO, $Cd(OH)_2$ and

CdO_2 , the latter of which corresponds to Cd^{4+}, whereas the first two correspond to Cd^{2+}. Calculations of the areas under the individual species curves show that more than 99 % of the Cd is in the form Cd^{2+}.

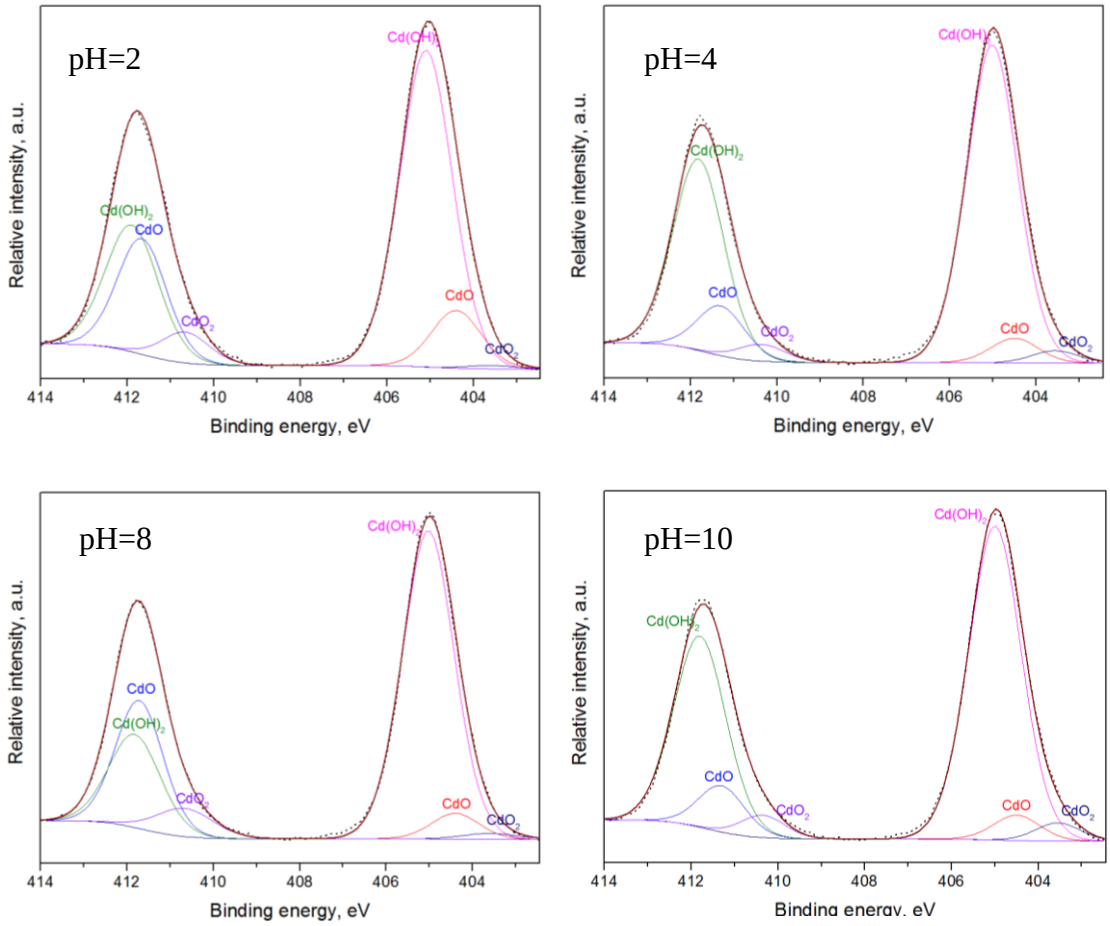

Figure 7.5: XPS spectra corresponding to the Cd-3*d* peaks of the Cd_3Fe^{III}/TiNT composite prepared at different initial pH (the dotted lines are the original spectra and the solid lines are the Gaussian-fitted spectra).

Figure 7.6 shows the XPS spectra in a range centred at the Fe 2*p* orbital binding energy. Doublet peaks at 723.91 eV ($2p_{1/2}$) and 709.55 eV ($2p_{3/2}$) are visible in all cases. A Gaussian basis function fitting is also shown on these plots, indicating the presence of six iron-containing species, Fe_2O_3, FeOOH, Fe_3O_4, FeO, Fe_3C and K_2FeO_4. This suggests that in addition to Fe^{3+}, the composite contains Fe^{2+}, probably as result of Fe^{3+} undergoing reduction to Fe^{2+}. The spectra for all samples are, on the other hand, weak and noisy, reflecting the low wt. % of Fe in the composites; the EDX analysis discussed later shows that only the sample at pH=2 contained an Fe wt. % of more than 1 %, some

of which will not be detected by XPS since it is contained in the inner surfaces of the TiNTs. It is difficult, therefore, to decompose the spectra into contributions from individual species, using any fitting procedure.

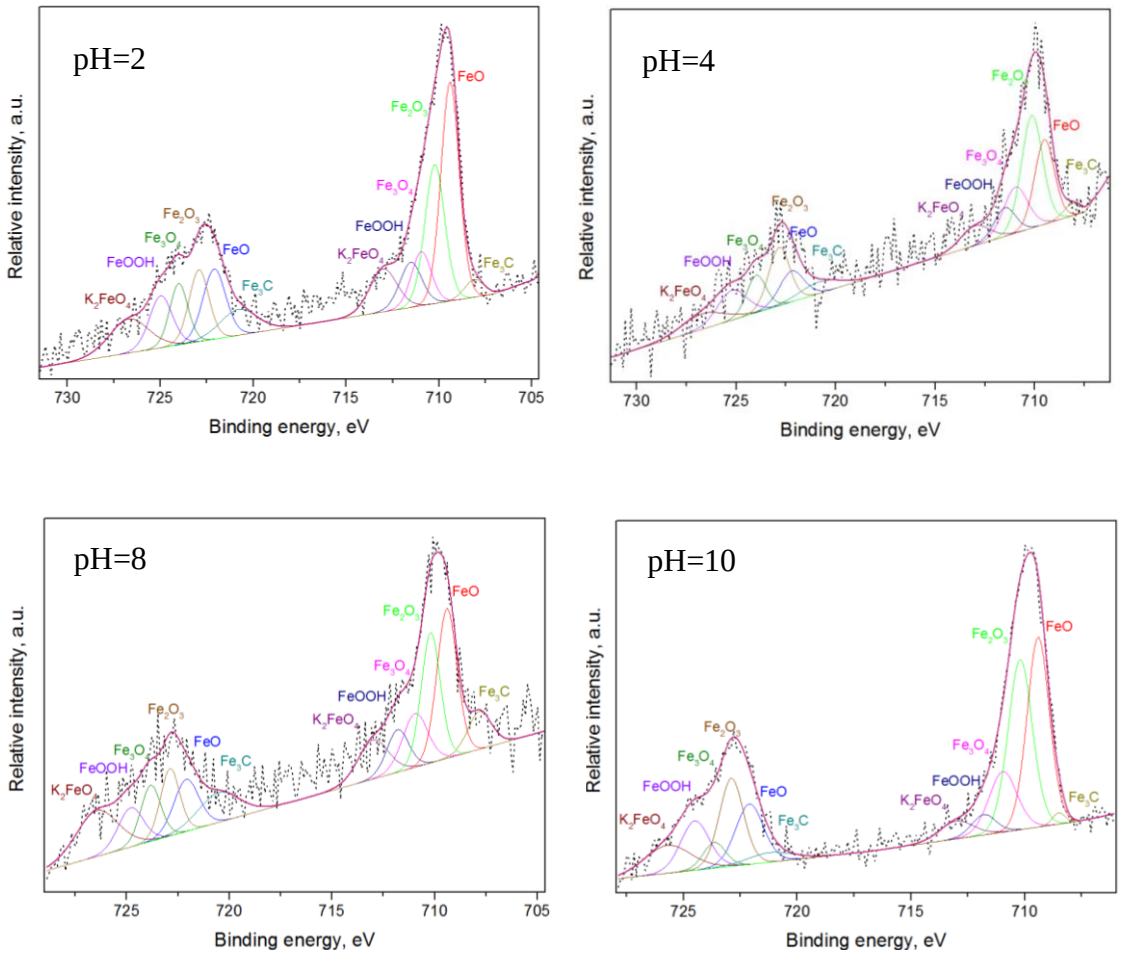

Figure 7.6: XPS spectra of Fe-2p peaks of the Cd_3Fe^{III}/TiNT composites prepared at different initial pH (the dotted lines are the original spectra and the solid lines are the Gaussian-fitted spectra).

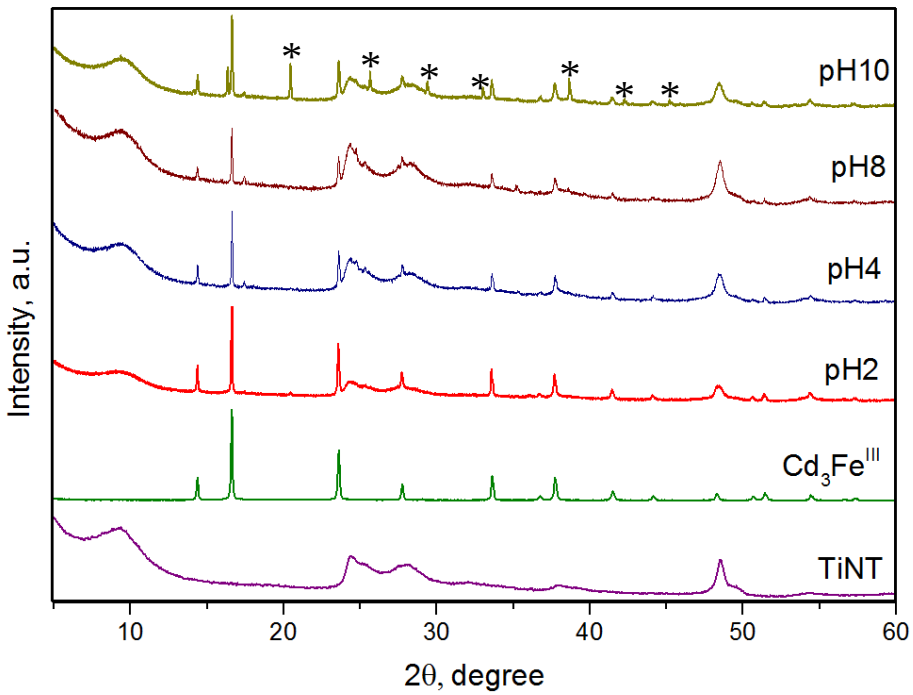

Figure 7.7: XRD patterns of as-prepared titanate nanotubes (TiNT), Cd_3Fe^{III} and Cd_3Fe^{III}/TiNT composite prepared at different initial pH. The asterisks mark characteristic reflections of different phases due to impurities.

7.2.4 X-ray diffraction

Figure 7.7 shows the XRD patterns for the composite samples at the different pH values, as well as bulk Cd_3Fe^{III} and bulk TiNT. The diffraction patterns at different pH contain characteristic reflections from both bulk Cd_3Fe^{III} and bulk TiNT, indicating that the process of Cd_3Fe^{III} particle deposition on the TiNT surfaces does not significantly alter the crystal structure of the TiNTs during reversible ion-exchange, as found in a previous study of the original (neutral pH) composite [3]. For the composite prepared at pH=2 the peaks associated with TiNT are of low intensity due to the poor stability of the TiNT in acidic environments (particularly noticeable from the peak at $2\theta \approx 48$ deg) [9]. The composite sample prepared at pH=10 exhibits characteristic reflections of at least seven different phases due to impurities (one at $2\theta \approx 21$ deg, and the rest at 2θ between 25-45 deg), which are marked on Figure 7.7 with asterisks. It is likely that this is due to a partial decomposition of Cd_3Fe^{III}, which leads to the formation of oxides and hydroxides of the outer (Cd) and inner (Fe) metals.

7.2.5 Energy-dispersive X-ray spectroscopy and elemental analysis

The EDX spectra in Figure 7.8 shows the presence of both metals (Fe and Cd) in all samples (at different pH values) which confirms that the Cd_3Fe^{III} complex is deposited onto the TiNT surfaces. The presence of potassium was explained in Chapter 5 (the ion exchange steps during preparation lead to a charge imbalance, which is compensated by

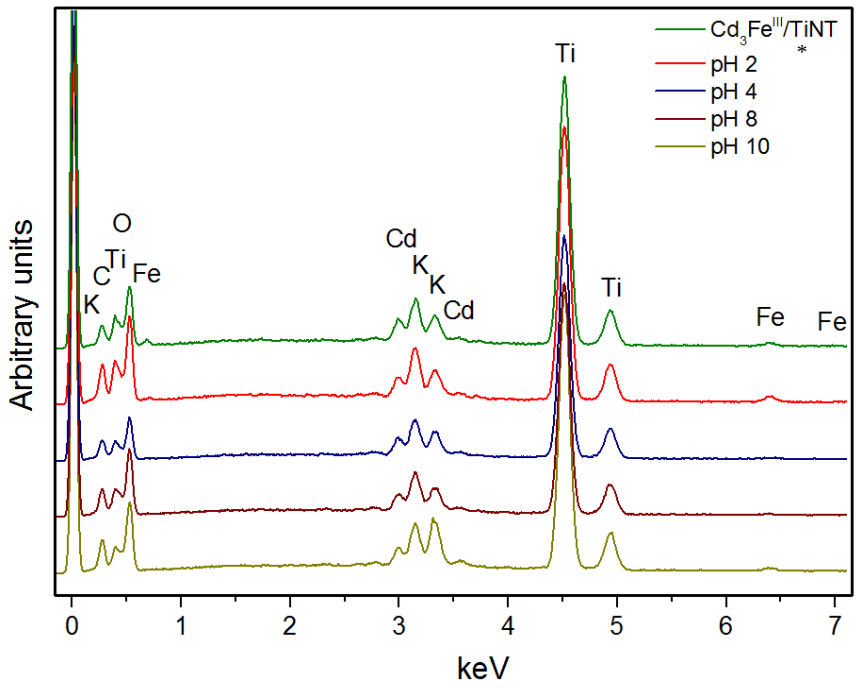

Figure 7.8: EDX spectra of the Cd_3Fe^{III}/TiNT composites prepared at different initial pH (*without pH adjustment).

K^+ cations on the TiNT surfaces of the composite). The results of elemental analyses (organic elemental analysis and energy dispersive spectroscopy) of all samples are shown in Table 7.1. There is a clear trend in the wt. % of Cd_3Fe^{III}, which decreases with increasing pH up to pH=8 (i.e. in an acidic or weakly basic environment). The wt. % in a strongly basic environment (pH=10), however, is considerably high than the value at pH=8. The wt. % follows the order pH2>pH10>pH4>pH8, consistent with the XPS analysis. The possible reasons for this behaviour are discussed after presenting the remaining characterization results.

Table 7.1: Elemental composition (wt. %) of the Cd^3Fe^{III}/TiNT composites prepared at different initial pH.

Element	pH=2	pH=4	pH=8	pH=10
H	1.434	1.271	1.205	1.089
C	2.325	0.710	0.635	1.417
N	2.712	0.829	0.741	1.654
O	35.712	38.103	38.290	36.844
K	0.568	1.200	0.950	2.851
Ti	45.892	48.856	49.096	47.242
Fe	1.803	0.551	0.493	1.099
Cd	9.475	8.480	8.589	7.803
Cd_3Fe^{III} wt. %	**12.257**	**3.731**	**3.348**	**7.425**

7.2.6 Atomic force microscopy

AFM is a powerful technique for probing the surface characteristics of materials, including their topographical and magnetic properties. AFM can be applied in different modes [10]. Phase imaging, which is an extension of the dynamic force or tapping mode, is able to detect differences in surface composition by mapping the phase of the cantilever oscillation. In this way, different components in composite materials can be distinguished. Figure 7.9 shows a three-dimensional high-resolution AFM image of a single TiNT obtained in phase imaging mode. The uniform single-phase surface of the single TiNT is well captured. Figure 7.10 shows a two-dimensional image of the TiNT sample (multiple TiNTs), again confirming that a single phase is present. These images will serve as references for the images of the composite materials shown below.

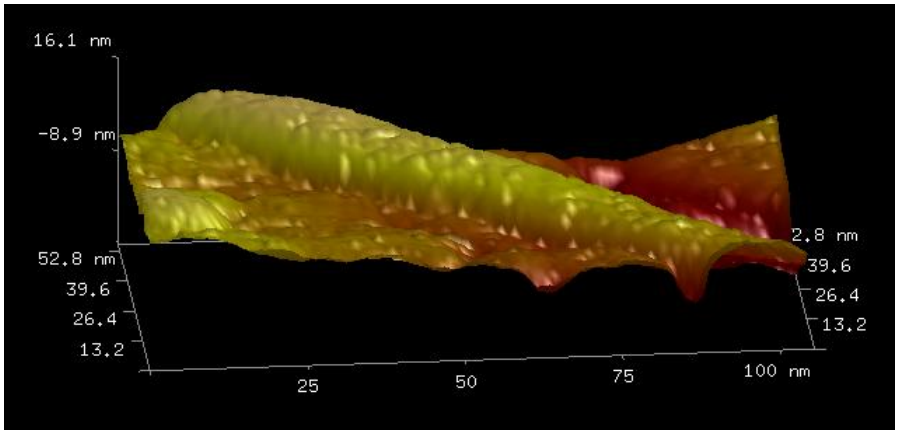

Figure 7.9: High re solution AFM 3D images of a 'single' titanate nanotube.

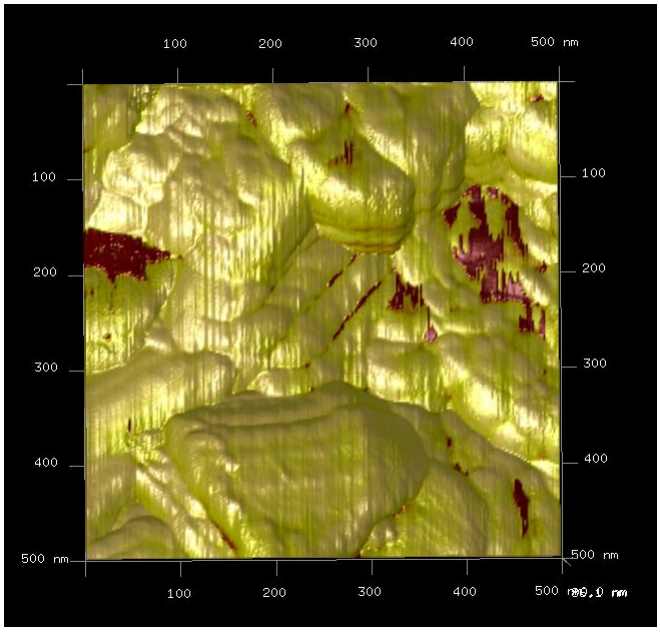

Figure 7.10: AFM images of TiNTs with phase imaging mode.

Figure 7.11 shows AFM images in phase imaging mode of the four Cd_3Fe^{III}/TiNT composite samples synthesized at different pH values. All of the images reveal the presence of two phases, the TiNTs and the Cd_3Fe^{III}. The distribution of the Cd_3Fe^{III} on the TiNTs is discontinuous, confirming the earlier TEM results in Chapter 5 and [3]. Perhaps more interestingly, the loading of the Cd_3Fe^{III} on the TiNTs is quite different depending on the pH value used during synthesis. For the samples prepared at pH=2 and pH=10, high loadings of Cd_3Fe^{III} on the TiNT surfaces are clearly visible. For pH=4 and pH=8, however, the level of Cd_3Fe^{III} is low, particularly at pH=8, confirming the results of the elemental (Table 7.1) and XPS analyses.

7.2.7 Discussion: effect of the pH on sample properties

The non-monotonic behaviour observed in the characterization results (AFM, XPS and elemental analysis) with respect to pH requires further investigation, which is beyond the scope of this thesis. Based on the available evidence, possible explanations are, nevertheless, proposed below.

Both a decrease and an increase of the pH of the solution increase the cation concentration; at low pH, the concentration of H^+ is elevated, whereas at higher pH the

concentration of K^+ is increased. Both of these cations increase the rate of Cd^{2+} leaching from the crystal structure of the TiNTs by shifting the following equilibriums to the right:

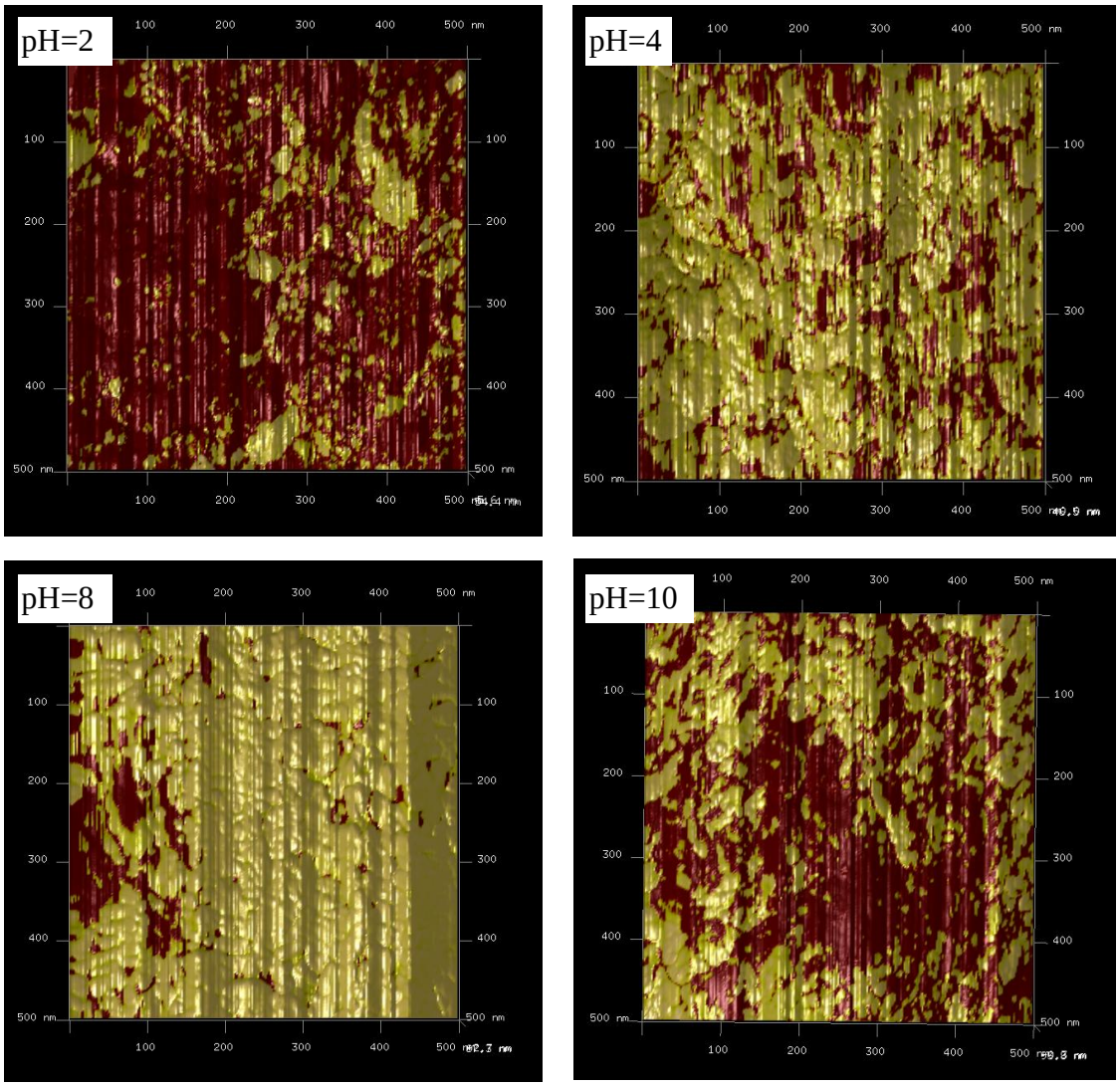

Figure 7.11: AFM images with phase imaging mode of (a) TiNT (b) the Cd_3Fe^{III}/TiNT composite prepared at different initial pH; scan size 500 nm.

$$Cd_xH_{2(1-x)}Ti_3O_7(s) + 2x\ H^+(aq) \rightarrow\ H_2Ti_3O_7(s) + x\ Cd^{2+}(aq) \qquad (7\text{-}1)$$

$$Cd_xH_{2(1-x)}Ti_3O_7(s) + 2x\ K^+(aq) \rightarrow\ K_{2x}H_{2(1-x)}Ti_3O_7(s) + x\ Cd^{2+}(aq) \qquad (7\text{-}2)$$

The released free Cd^{2+} ions can react rapidly with $[Fe(CN)_6]^{3-}$ anions forming Cd_3Fe^{III} precipitates on the TiNT surfaces. It is possible that when the rate of Cd^{2+} release from the TiNTs is slow, the Cd_3Fe^{III} phase formed is not strongly adhered to the surfaces of nanotubes and can be removed during subsequent washing. As a result, the loading of Cd_3Fe^{III} on the TiNTs is high at both acidic and basic pH, and low at moderate pH values.

7.3. Gas adsorption measurements

7.3.1 Sample evacuation

Adsorption experiments were conducted in order to assess the performance of the composites prepared under different initial pH values (in step (7-1)). Prior to the measurements, the samples were degassed under vacuum conditions shown in Table 3.2 to remove any moisture or other adsorbed gases from the surfaces of the solid. For complete removal of moisture or other contaminants, while avoiding dissolution and/or damage to the pore structure of the samples, temperatures and degassing times were determined according to the results of a thermogravimetric analysis (TGA).

Figure 7.12 demonstrates the weight loss % of the different samples in a heating range of 20–800 ˚C. For temperatures below 200 ˚C, the weight loss in all samples is related to the loss of water (zeolitic and coordinated) adsorbed on the surfaces of the solids. The loss of weight for the samples prepared at pH=4, pH=8 and pH=10 is almost 12 wt. %, and in the case of pH=2, the loss is around 13.5 wt. %. The wt. loss % ordering follows a similar pattern to that of the loading: pH2>pH10>pH4≈pH8. In the bulk cadmium ferricyanide, the binding between water and the solid surface is weak; dehydration of this material occurs at temperatures below 100 ºC [11]. Thus a higher loading of the cadmium ferricyanide should lead to a higher weight loss, as seen in the TGA results.

For temperatures above its dehydration temperature (which is lower than 100 ºC), decomposition of bulk Cd_3Fe^{III} would take place, forming C_2N_2 and ferrocyanide $[Fe(CN)_6]^{-4}$, which is stable up to 300–400 ˚C [11]. For the Cd_3Fe^{III} loaded on the TiNTs, however, decomposition takes place at temperatures above 200 ºC, which demonstrates that the Cd_3Fe^{III} is more stable when deposited on the TiNTs. In the case of TiNTs, phase transformation to anatase takes place only above temperatures of

approximately 400 ºC [12]. Based on these results, the activation temperatures and times were chosen according to Table 3.2.

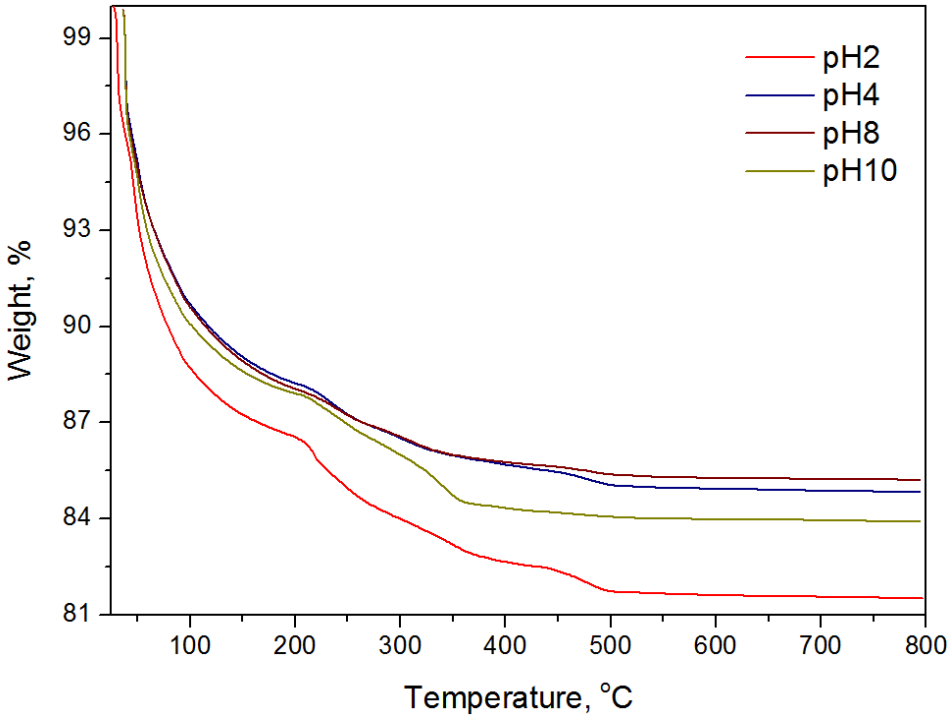

Figure 7.12: TGA plots for the Cd_3Fe^{III}/TiNT composites prepared at different initial pH.

7.3.2 Gas adsorption results

Figure 7.13 shows the adsorption and desorption equilibrium isotherms of N_2 at 77 K onto the Cd_3Fe^{III}/TiNT composites prepared at pH values of 2, 4, 8, and 10. In Chapter 5 it was demonstrated that decoration of the nanotubes with Cd_3Fe^{III} results in an increase in the BET surface area (from 210 $m^2\ g^{-1}$ to 244 $m^2\ g^{-1}$), and an increase in the total pore volume (from 0.64 $cm^3\ g^{-1}$ to 0.67 $cm^3\ g^{-1}$). The BET surface areas (shown in Table 7.2) follow the ordering: pH2>pH10>pH4>pH8, i.e., the same ordering as that of the loading of Cd_3Fe^{III} on the TiNTs (Table 7.1).

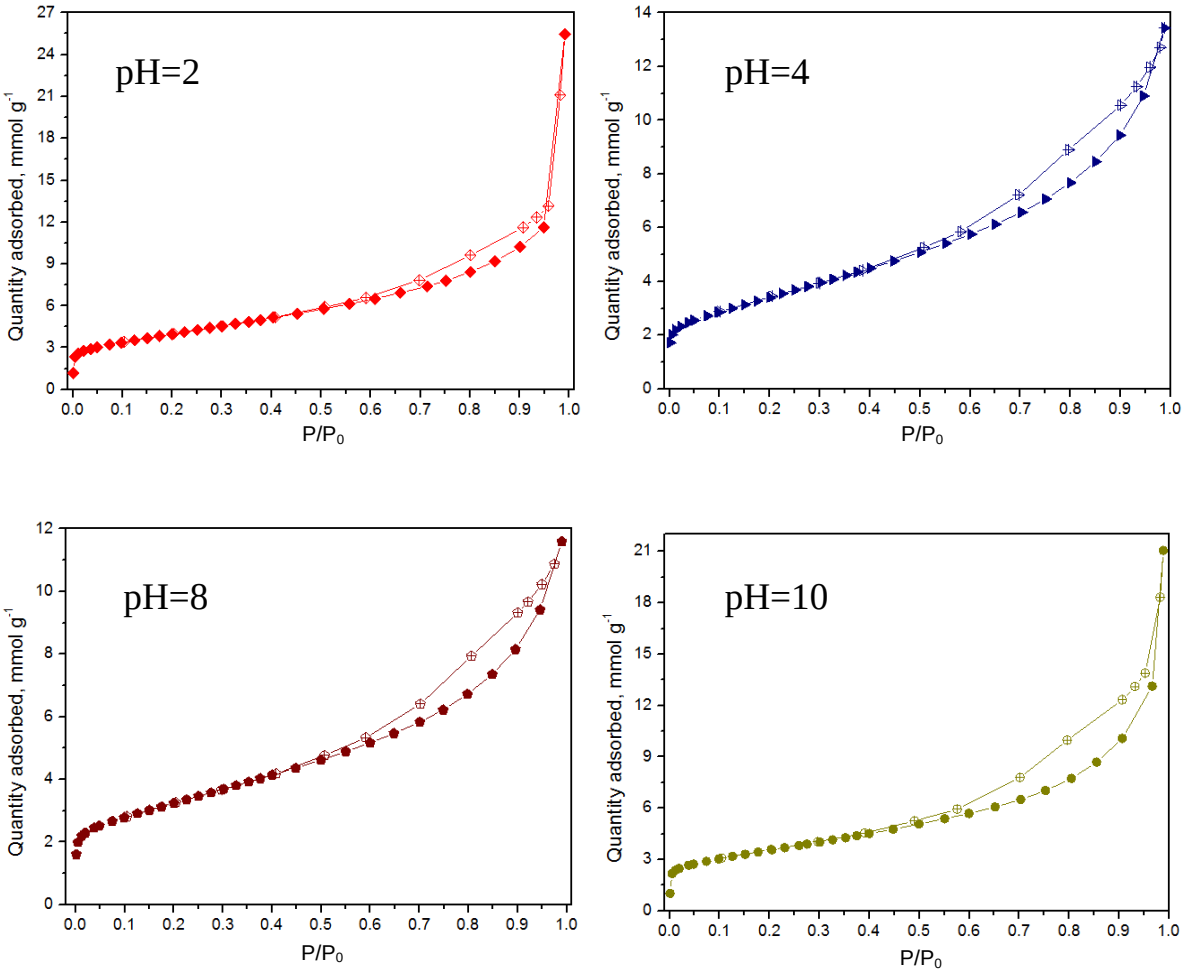

Figure 7.13: Adsorption (solid symbols) and desorption (empty symbols) isotherms of N_2 at 77 K onto the Cd_3Fe^{III}/TiNT composites prepared at pH values of 2, 4, 8, and 10.

The highest value, at pH=2, is 317.193 $m^2\ g^{-1}$, which is approximately 24 % higher than the lowest value obtained at pH=8. The loading of Cd_3Fe^{III}, however, is 266 % higher in the sample prepared at pH=2 compared to the sample prepared at pH=8. In other words, a naïve assumption of a similar increase in the surface area is not valid. The BJH pore size distributions for the composites are shown in Figure 7.14. The cumulative pore volumes (CPVs), shown in Table 7.2, also follow the ordering pH2>pH10>pH4>pH8.

The increase in CPV between pH=8 and pH=2 is approximately 130 %. Figure 7.14 reveals key differences in the pore size distributions between the samples. At high and low pH (2 and 10), the distribution is bi-modal, whereas the distributions at pH=4 and 8 are essentially uni-modal. In each of the samples prepared at pH=2 and 10, there is a peak in the range of pore diameters 50–60 nm, in addition to the peak at around 10 nm.

This is also evident from the average pore diameter (APD) calculations in Table 7.2, which are considerably larger for the samples prepared at pH=2 and 10. It is clear that much of the additional pore volume created by the higher loading of Cd_3Fe^{III} does not translate into active surface area for adsorption.

Table 7.2: Adsorption parameters for the Cd_3Fe^{III}/TiNT composite samples prepared at different initial pH.

Sample	Cd_3Fe^{III} wt. %	SSA_{BET}[3] ($m^2\ g^{-1}$)	CPV[4] ($cm^3\ g^{-1}$)	APD[5] (nm)	H_2 uptake at 1 bar,77K ($mg\ g^{-1}$)	ΔH_{ads} at 1.4 mg g^{-1} ($kJ\ mol^{-1}$)
pH=2	12.3	317	0.851	12.8	2.86	–6.31
pH=4	3.7	276	0.446	7.2	2.59	–5.43
pH=8	3.3	255	0.372	7.3	2.56	–5.65
pH=10	7.4	279	0.713	12.2	3.18	–6.18

It is known that small pores, particularly those with diameters < 1 nm, are ideal for H_2 adsorption due to the stronger interaction between the gas and sorbate surface [13,14]. Dash [14], e.g., found that in carbide derived carbons, an increase in the pore diameter above 2 nm led to a decrease in the H_2 uptake. Extrapolating to N_2, it is likely, therefore, that the large pores (with peaks around 60 nm) at pH=2 and 10 are not effective for

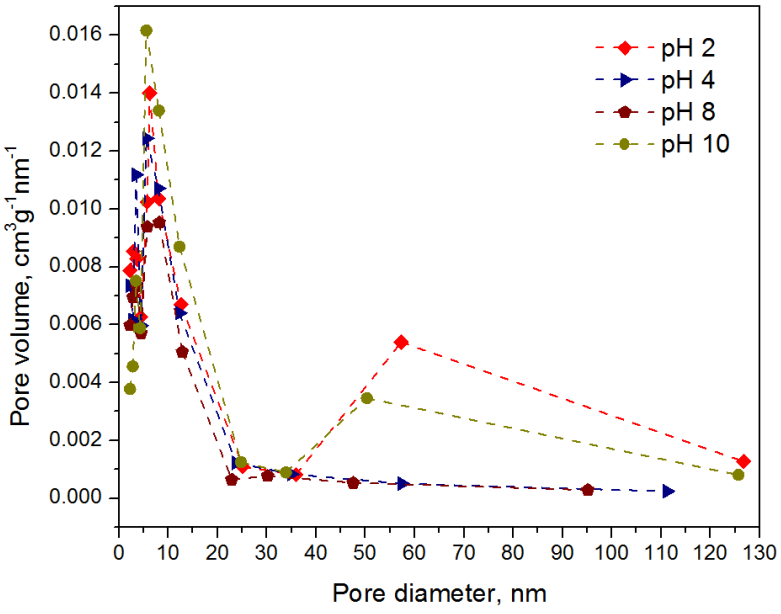

Figure 7.14: Pore size distributions of the Cd_3Fe^{III}/TiNT composite samples prepared at different initial pH.

[3] SSA = Specific Surface Area
[4] CPV = Cumulative Pore Volume
[5] APD = Average Pore Diameter

adsorption (the interaction strength is too weak). Thus, much higher loadings and CPVs translate into only relatively modest increases in the surface area for adsorption.

Figure 7.15 shows the hydrogen adsorption isotherms at 77 K for the TiNT and Cd_3Fe^{III}/TiNT composites prepared at different pH, including without pH adjustment. The H_2 uptake at 1 bar (see Table 7.2) follows the ordering pH10>pH2>pH4>pH8, which does not agree with the orderings for the loading of Cd_3Fe^{III} and BET surface area; pH=2 and pH=10 are interchanged. The reason for this interchange is apparent from the small pore region in Figure 7.14. The peak in the specific pore volume of small pores centred around 10 nm follows the ordering pH10>pH2>pH4>pH8, i.e., the same as the ordering of the H_2 uptake values at 1 bar. Taking any two samples, the ratios of the areas under the plots in Figure 7.14 (cumulative volumes) up to 25 nm diameter are approximately equal to the ratios between the uptake values. These results confirm that the large pores in the pH=2 and 10 samples play a minor role in the H_2 adsorption process.

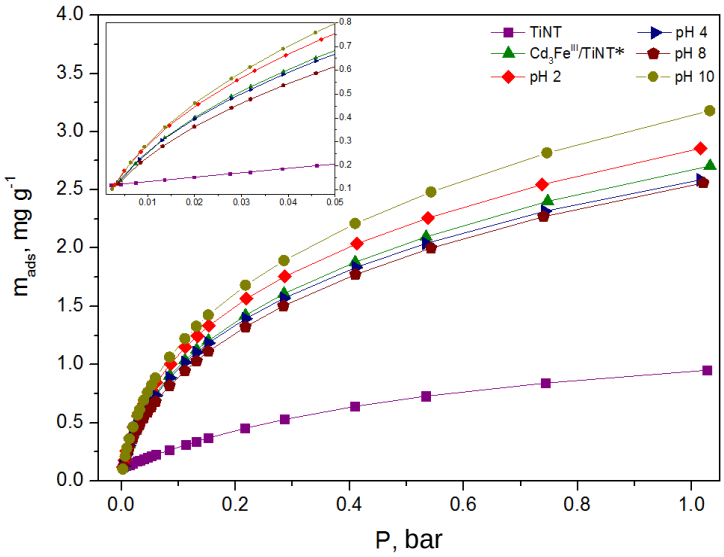

Figure 7.15: Comparative hydrogen adsorption isotherms at 77 K for the titanate nanotubes (TiNT) and the Cd_3Fe^{III}/TiNT composites prepared at different initial pH (*without pH adjustment).

The BET surface area measured with N_2 appears not to give an accurate indication of the surface area for H_2 adsorption (see Table 7.2). The much larger diameter of the N_2 molecule probably leads to a better interaction with the composite in the large pores, leading to a greater retention of N_2 compared to H_2. Thus, the BET surface area

overestimates the area for H_2 adsorption. Another factor that may play a role in the high uptake at pH=10 is the high wt. % of K^+ ions (see Table 7.1). The close proximity of K^+ ions within the TiNT lattice to the Cd_3Fe^{III} can create local charge centres capable of participating in hydrogen adsorption through electrostatic interactions [15].

7.3.3 Isosteric enthalpy of adsorption

The hydrogen adsorption isotherms at two temperatures, 77 and 87 K, were fitted to the Freundlich, Langmuir and Langmuir-Freundlich (L-F) models in order to select the best model for calculating the isosteric enthalpies of adsorption. For convenience, the models are presented below (see Chapter 4 for further details):

$$\text{Freundlich: } \theta = K_F P^{1/n_F} \tag{7-3}$$

$$\text{Langmuir: } \theta = \frac{K_L P}{1 + K_L P} \tag{7-4}$$

$$\text{Langmuir-Freundlich: } \theta = \frac{K_{LF} P^{1/n_{LF}}}{1 + K_{LF} P^{1/n_{LF}}} \tag{7-5}$$

in which θ is the surface coverage, K_F, K_L and K_{LF} are the Freundlich, Langmuir and L-F constants, respectively, and n_F and n_{LF} are the Freundlich and L-F heterogeneity factors, respectively. The results of the fit are shown in Figure 7.16. The best fit across the two temperatures (the highest correlation coefficient R^2) was obtained with the LF model.

A variant of the Clausius-Clapeyron equation was used to calculate the isosteric enthalpy of adsorption, ΔH_{ads} as follows:

$$\Delta H_{ads} = R\left(\frac{T_2 - T_1}{T_1 T_2}\right)\ln\left(\frac{P_1}{P_2}\right) \tag{7-6}$$

in which T_1 and T_2 refer to the two temperatures and P_1 and P_2 are the corresponding pressures on the equilibrium curve, at the same uptake value. The relationship between uptake (equivalently the surface coverage) and hydrogen pressure was assumed to take the form of the LF equation (7-5) together with the parameters that were determined in the fitting procedure described above. Thus:

$$\Delta H_{ads} = R\left(\frac{T_2 - T_1}{T_1 T_2}\right)\ln\left[\frac{\left(\frac{\theta_1}{K_{LF}(T_1)(1-\theta_1)}\right)^{n_{LF}(T_1)}}{\left(\frac{\theta_2}{K_{LF}(T_2)(1-\theta_2)}\right)^{n_{LF}(T_2)}}\right] \quad (7\text{-}7)$$

where R is the universal gas constant and the subscripts '1' and '2' refer to values at T_1 and T_2, respectively. The explicit dependence of the LF constant and LF heterogeneity factor on temperature is also indicated.

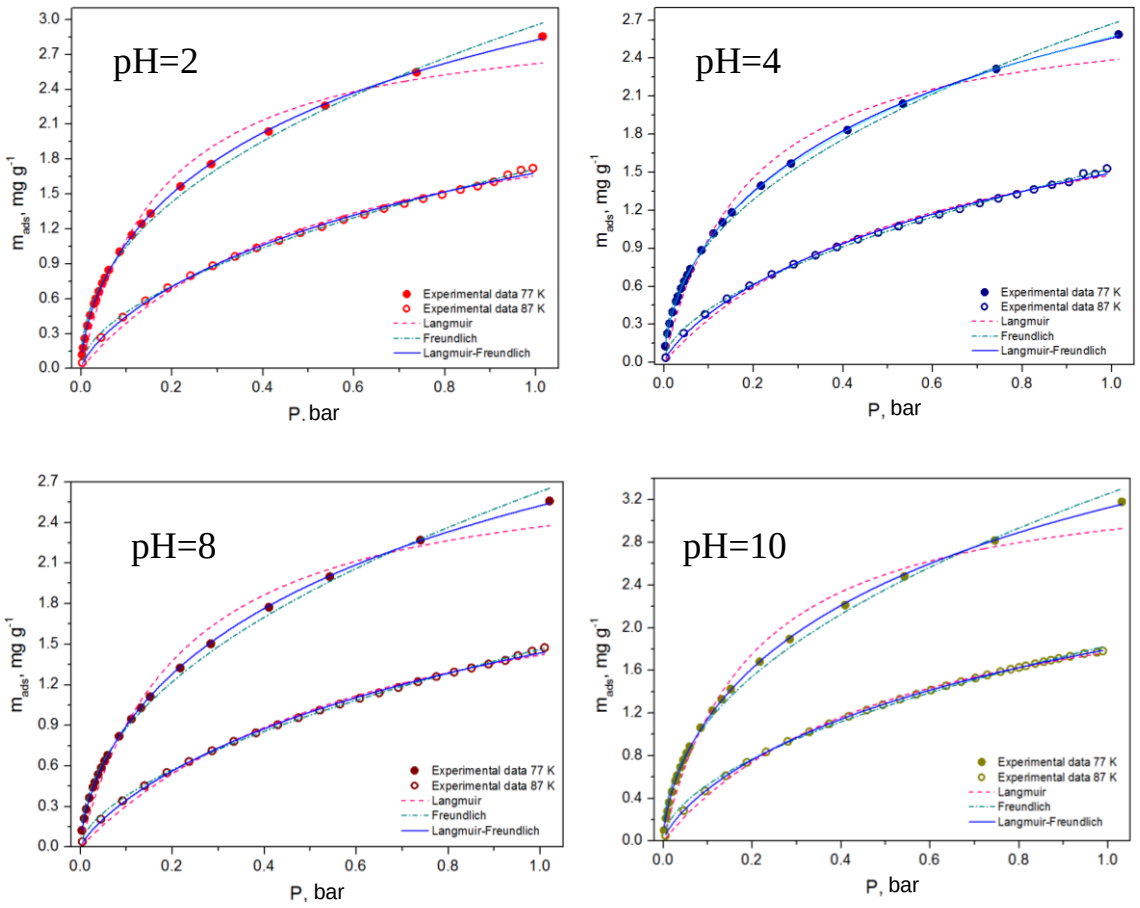

Figure 7.16: Experimental and simulated hydrogen adsorption isotherms on the Cd_3Fe^{III}/TiNT composite at 77 K (filled symbols) and 87 K (open symbols), for samples prepared at different initial pH.

Figure 7.17 plots the calculated isosteric enthalpies of adsorption as functions of the amount of H_2 adsorbed for the four samples of the Cd_3Fe^{III}/TiNT composite prepared at different initial pH. The values at an uptake value of 1.4 mg g^{-1} are shown in Table 7.2. As expected, the enthalpies of adsorption are highest at low coverages, when a large

number of surface sites are available. As the coverage increases, the enthalpies decay. The differences in the adsorption enthalpies at 1.4 mg g^{-1} are relatively minor (all fall within the range 5.5–6.5 kJ mol^{-1}), suggesting no significant change in the interaction strengths between the samples, at least up to 1.4 mg g^{-1}. Thus, the major differences seen in the H_2 adsorption results between the different samples are primarily a function of the differences in morphology.

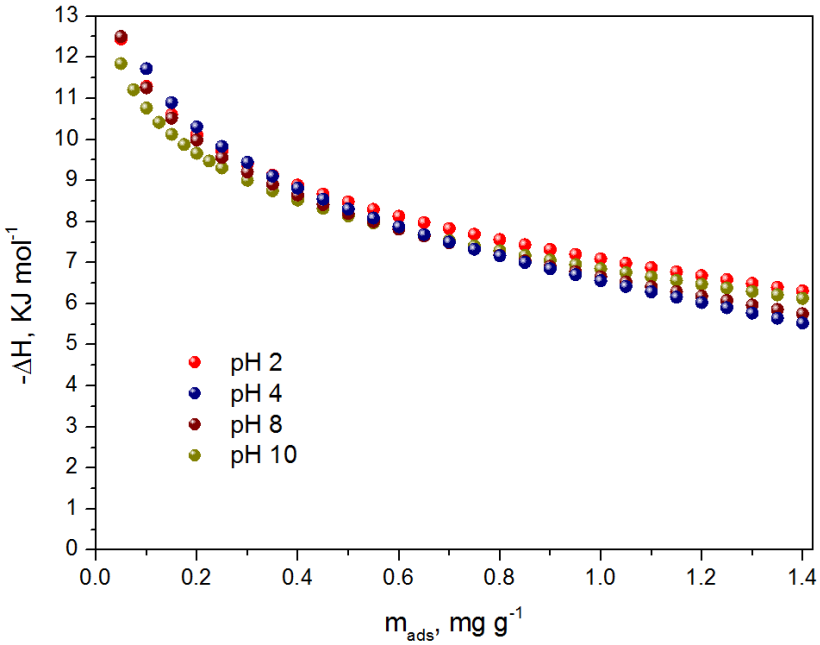

Figure 7.17: Variations of enthalpies of adsorption with the amount of H_2 adsorbed for samples of the Cd_3Fe^{III}/TiNT composites prepared at different initial pH.

References

[1] Bavykin D.V., Lapkin A.A., Plucinski P.K., Torrente-Murciano L., Friedrich J.M., Walsh F.C., Top Catal 39 (2006)151–160.

[2] Ma R., Sasaki T., Bando Y., Chem. Commun. 7 (2005) 948.

[3] Al-Hajjaj A.A., Zamora B., Bavykin D.V., Shah A.A., Walsh F.C., Reguera E., Int. J. Hydrogen Energy, 37 (2012), 318–326.

[4] Bavykin D.V., Cressey B. A., Light M. E., Walsh F. C., 19 (2008) 275604–275608

[5] Ivekovic D., Gajovic A., Ceh M., Pihlar B., Electroanalysis 22 (2010) 2202–2210.

[6] Nakamoto K., Infrared and Raman Spectra of Inorganic and Coordination Compounds, John-Wiley and Sons, New York, Chichester, Brisbane, Toronto, Singapore, 1986, p. 484.

[7] Fernandez J., Blanco J., Reguera E., Spectrochim. Acta A 46 (1990) 685–689.

[8] Fernandez J., Reguera E., Blanco J., Spectrochim. Acta A 46 (1990) 1679–1682.

[9] Bavykin D. V., Friedrich J. M., Lapkin A. A., Walsh F. C.,Chem. Mater. 18 (2006) 1124–1129.

[10] Stark R. W., Drobek T., Heckl W. M., Appl. Phys. Lett., Vol. 74, No. 22, (1999) 3296–3298.

[11] Iveković D., Japec M., Solar M., Živković N., Int. J. Electrochem. Sci., 7 (2012**)** 3252–3264.

[12] Lei Qian, Zu-Ling Du, Sheng-Yi Yang, Zhen-Sheng Jin, Journal of Molecular Structure 749 (2005) 103–107.

[13] Yushin G., Dash R., Jagiello J., Fischer J., Gogotsi Y., Advanced Functional Materials, Vol. 16, Issue 17 (2006) 2288–2293.

[14] Dash R.K., Nanoporous Carbons Derived from Binary Carbides and their Optimization for Hydrogen Storage, PhD Thesis, Drexel University, 2006.

[15] Krap C.P., Balmaseda J., del Castillo L.F., Zamora B., Reguera E., Energy & Fuels, 24 (2010) 581–589.

Chapter 8: Conclusions and future work

8.1 Conclusions

Efficient, low cost hydrogen storage is key to the realization of hydrogen-based energy economy. Hydrogen can be stored in various ways depending on the application. Compressed or liquefied hydrogen are currently used for fuel-cells in automobiles, given that the technology for this type of storage is well-understood, proven and commercially available. The energetic cost of compression and liquefaction processes and the problems associated with safety and maintenance have led many to conclude that it is not a practical long term solution. The storage of hydrogen in solid state (through either chemisorption or physisorption) is a safer and simpler method, although the cost is higher and the technology is still in a state of development.

In this thesis, a general mathematical framework for simulating hydrogen adsorption in microporous materials and estimating key properties, including the surface area, isotherm parameters and adsorption volume, was developed. An attractive and practical feature of the approach is that it requires only a single, standard regression analysis to determine all of the unknown parameters. Additionally, the modelling framework provides explicit expressions for the condensed, excess and absolute masses.

The simulation of adsorption equilibrium isotherms for four microporous materials revealed that the Langmuir isotherm model provides a poor fit to the experimental data, while the remaining isotherms models were able to fit the data well for all materials. There were, nevertheless, significant differences between the parameter values predicted by each of these isotherms, although the ordering of the values was consistent for Dubinin-Astakhov, Toth and UNILAN. This underlines the importance of using independent data to verify the estimates of accessible parameters (e.g. surface area/maximum capacity) and ab-initio modelling, such as Monte Carlo simulations, to

estimate inaccessible parameters (e.g., heterogeneity) before judging the accuracy of a model isotherm for a particular system.

Another important consideration in the application of regression analysis to hydrogen sorption (highlighted in Table 4.5) is the range of pressure used. Reliable estimates of the maximum adsorption volume can only be obtained using data that extends well beyond the saturation point. Although the differences in the other parameters (the surface area and the affinity and heterogeneity constants) are relatively small, they are, nonetheless, significant. The example in Table 4.5 shows a difference in the predicted surface area of 10 % between excess data up to saturation (≈3 atm) and the full range of data (up to 9.86 atm) using the same isotherm model.

In Chapter 5, a novel composite for hydrogen storage was developed. The decoration of titanate nanotubes with nanostructured $Cd_3[Fe(CN)_6]_2$ using ion exchange with Cd^{2+} ions and reaction with $[Fe(CN)_6]^{3-}$ counter ions yields a composite that is characterised by unusually high values of hydrogen uptake at 77 K. The hydrogen storage capacity in the composite at 77 K and 150 bar is approximately 3.5 times higher (15 wt. % *vs*. 4.3 wt. %) than the value based on a weighted average of the capacities for the two base components, suggesting that a strong interaction takes place between the nanotubes and the PB analogue materials. This strong interaction affects the nature of the hydrogen adsorption centers in the composite, increasing the value of the apparent enthalpy of the adsorption. Further systematic studies are required to reveal the nature of these interactions and to optimize the composition of the composite material in order to achieve higher hydrogen sorption capacities.

The kinetic and thermodynamic hydrogen adsorption characteristics of the Cd_3Fe^{III}/TiNT were investigated in Chapter 6. The previously obtained high uptake values were confirmed. It was demonstrated using pseudo first and second-order kinetic models that film diffusion does not play a limiting role in the mass transport of hydrogen inside the composite material. An intra-particle model for diffusion of hydrogen in the cylinder-like composite particles was employed to calculate the diffusion coefficient and time constant for hydrogen at different temperatures and pressures. Based on the results, and on approximate values for the Knudsen diffusion coefficient, molecular diffusion appears to dominate mass transport inside the composite material. This is possibly due to a preponderance of transport through the

inner layers of the nanotubes as opposed to between layers, in which Knudsen diffusion is expected to make a major contribution based on the analysis.

The apparent isosteric enthalpy of adsorption ΔH_{ad}, was calculated by fitting the Gibb's free energy to the Clausius–Clapeyron equation. The Gibb's free energy was determined by fitting the data to the Dubinin–Astakhov isotherm model. The calculated value of ΔH_{ad} is characteristic of a physisorption process and is higher than the value for bulk Cd_3Fe^{III} and comparable to the values obtained for most metal organic frameworks. It was found that value of ΔH_{ad} is considerably higher than the activation energy for intraparticle diffusion, E_a, calculated in the aforementioned analysis. This suggests that the rate-limiting step of hydrogen adsorption onto the composite material is surface adsorption.

In Chapter 7, the effects of variations in the synthesis environment, namely the pH at the start of reaction (5-2), were investigated. The samples were thoroughly characterised to reveal their surface characteristics and gas adsorption properties. It is clear from the results that the loading of Cd_3Fe^{III} and on the TiNTs and the morphology of the resulting composite material can, to some extent, be engineered in order to increase the H_2 uptake capacity. It was shown that a large increase in the loading of Cd_3Fe^{III} does not necessarily lead to a proportionate increase in the hydrogen uptake capacity. The key to this result was the pore size distribution; large pores, which are formed at high and low pH (in step (5-2)), were found not to be effective for adsorption. An increased loading of $Cd_3[Fe(CN)_6]_2$ should ideally be accompanied by an increase in the density of small pores, avoiding the creation of pores with diameter greater than 10 nm. This would lead to the optimal increase in the *effective* surface area and volume for adsorption.

8.2 Future work

The modelling framework developed in Chapter 4 is applicable to any porous material, provided a relevant isotherm model is available. Non-equilibrium adsorption, in which there exists a driving force for mass transfer between the adsorbed and compressed phases, would represent an important extension to the present work. The results of such a study would generalise equations (4-14) and (4-15), which were derived under the assumption of equilibrium. For the materials considered in Chapter 4, the isotherms are all of type I. Type VI isotherms, which are common to many families of microporous

materials, such as metal-organic frameworks, could equally be simulated using appropriate isotherm models.

The mechanism of hydrogen adsorption and the exact nature of the interaction between hydrogen and the Cd_3Fe^{III}/TiNT composite surface should be investigated futher via:

a) Detailed thermogravimetric analysis (including thermal stability, differential thermal analysis and differential scanning calorimetry);
b) In-situ X-ray diffraction;
c) Synchrotron X-ray analysis,
d) Mössbauer spectroscopy;
e) Temperature programmed adsorption
f) Structural and crystallography analysis.

The results of Chapters 5–7 suggest a detailed study of hydrogen adsorption in composites of TiNT and the general class of metal-cyanide frameworks $M_x[T(CN)_6]_y$, i.e., varying the inner and outer metals. For example, T=Co, which, from initial findings not reported in this thesis, yields highly promising results. Other families of materials such as nitroprussides, $M_3[Fe(CN)_5NO]$ have also been deposited on TiNTs in work that is not reported in this thesis. This represents another promising avenue for exploration.

Finally, initial investigations of the photocatalytic, electro-catalytic and gas separation properties of the Cd_3Fe^{III}/TiNT composite were conducted, yielding highly promising results. These applications are worthy of much more detailed investigations.